Lehrstuhl für Elektrische Energiespeichertechnik
Fakultät für Elektrotechnik und Informationstechnik
Technische Universität München

Phase Change Material in Battery Thermal Management Applications

An assessment of efficiency and safety

Dipl.-Ing. Univ. Christian Huber

Vollständiger Abdruck der von der Fakultät für Elektrotechnik und Informationstechnik der Technischen Universität München zur Erlangung des akademischen Grades eines

Doktor-Ingenieurs (Dr.-Ing.)

genehmigten Dissertation.

Vorsitzender:		Prof. Dr. Sc. (ETH) Samarjit Chakraborty
Prüfer der Dissertation:	1.	Prof. Dr.-Ing. Andreas Jossen
	2.	Prof. Dr.-Ing. Markus Lienkamp

Die Dissertation wurde am 19.04.2017 bei der Technischen Universität München eingereicht und durch die Fakultät für Elektrotechnik und Informationstechnik am 06.07.2017 angenommen.

Abstract

Driven by the rise of electric vehicles and stationary storage applications, large battery systems emerge from a niche to a standard product with serious production volume. However, some technological challenges in handling those batteries still remain. Especially in those new complex and high-performance applications, there is a significant need for battery thermal management, heating and cooling. Hence, depending on ambient conditions, a considerable amount of the effective battery energy has to be deployed for tempering the system. Up to now mainly active components have been used for this task, that not only reduce the overall efficiency, but also increase system weight, volume and maintenance effort.

Within the presented work an alternative passive Battery Thermal Management System (BTMS) concept, based on latent heat storage components is showcased and reviewed for its appropriateness in battery applications. For this purpose all relevant temperature sensitivities of modern Lithium Ion Batteries (LIBs) are presented and experimentally confirmed at first, before an overview on the range of Phase Change Materials (PCMs) is given. In this context relevant material properties are summarized and materials' dynamic behavior is replicated. Details of composite material production and characterization are introduced. The results are transferred into a numerical model of phase change processes, which is then utilized for the consecutive transient simulations and case studies, forming the core part of the work.

With the help of laboratory experiments on single battery cells and real life case studies on larger battery systems, the impact of different PCM samples on the most common BTMS tasks is assessed and quantified. Peak shaving, passive cooling and prevention of Thermal Runaway (TR) propagation are investigated for automotive and stationary applications. The results obtained, suggest that PCM, if chosen properly, can significantly contribute to an increase in system efficiency and safety. However, detailed quantified data also highlights that the quality of the results is highly dependent on the chosen material and its dimensioning. Especially thermal inertia and melting temperature have been identified as main design levers. The corresponding impact of those two factors is quantified for each specific application and a design guideline for PCM based BTMS is derived.

Acknowledgements, standards and conventions

The acquisition of results presented in this thesis has only been possible thanks to the support of numerous individuals and institutions. First of all, the Institute for Electrical Energy Storage Technology at Technical University Munich and its chair Professor Andreas Jossen, who has supervised and supported the research over many years, are to mention. Field tests and measurements on the large scale stationary storage modules (case studies II/III) have only been enabled by kind support of the EEBatt project, funded by the Bavarian State Government and thanks to the close collaboration with the TÜV Süd Battery Testing GmbH. Another large fraction of experimental work and especially the automotive case study (I) were conducted in the laboratories of TUM CREATE and kindly funded by the National Research Foundation of Singapore. Essential valuable input has been contributed by all academic and supportive colleagues, both from Munich and Singapore.

In the following some general definitions are made that are valid throughout the thesis and are considered constant. Regarding the cell terminals, anode is referred to as negative, cathode as positive. Current flows are referred to as negative when discharging the cell and positive in charging direction. The term "C rate" is defined as quotient of current and nominal capacity. The term "stack" is used for a compound of multiple cells, which is not operational on its own, while independent multi-cell systems, which include a Battery Management System (BMS) are referred to as modules. Complete systems comprising one or several modules as well as cooling components, electronics and mechanical structure are titled "battery packs".

Solely LIBs are considered. Research focuses on Nickel Manganese Cobalt Oxide (NMC), Nickel Cobalt Aluminum Oxide (NCA) and Lithium Iron Phosphate (LFP) cell chemistry and common form factors. Where not stated else wise, one of the three cells described in section 3.5 is used for experiments, measurements and simulations. State Of Charge (SOC) of tested cells is individually stated for all experiments and consequently referred to the new cells' nominal capacity.

Presented material data is given for a reference temperature of 25 °C if not stated otherwise explicitly.

Contents

Glossary III

Abbreviations V

Formula Symbols VII

1 Introduction and Motivation 1
- 1.1 Battery market development and trends 2
- 1.2 Importance of Battery Thermal Management 3
- 1.3 Scope and approach 5

2 Sensitivity of Lithium Ion Batteries towards temperature 7
- 2.1 Capacity and capacity fade 11
- 2.2 Power and power fade 13
- 2.3 Reversible self-discharge 14
- 2.4 Low temperature behavior and lithium plating 14
- 2.5 Thermal runaway 16
- 2.6 Summary of cell thermal sensitivity 17

3 Battery thermal characteristics 19
- 3.1 Specific heat 19
- 3.2 Thermal conductivity 22
- 3.3 Heat generation rate 27
- 3.4 Onset temperature 31
- 3.5 Overview on experimental values for selected cells 31

4 Battery thermal management: state of the art 33
- 4.1 Air based systems 34
- 4.2 Liquid based systems 38
- 4.3 Refrigerant based systems 41
- 4.4 Comparison of common concepts 43
- 4.5 Thermal energy storage 44

5 Phase change material (PCM) 47
- 5.1 Classification and properties 47
- 5.2 Characterization 52
- 5.3 Composite functional materials 53
- 5.4 Graphite Paraffin composite 56

6 Modeling PCM 61
- 6.1 The Stefan problem 61

6.2 Analytical solution . . . 62
6.3 Numerical models . . . 64
6.4 Model validation . . . 67

7 PCM in LIB applications 69
7.1 Overview on existing research and implementation . . . 69
7.2 Experimental single cell studies . . . 70
7.3 Passive control of temperature rise (constant moderate load) . . . 71
7.4 Mitigation of peak loads . . . 73
7.5 Increasing temperature uniformity . . . 75
7.6 Preventing thermal runaway . . . 77
7.7 Summary of single cell experiments . . . 79

8 Design methodology - case studies 81
8.1 Case study: Mitigation of peak loads during fast charging . . . 82
8.2 Case study: Passive cooling . . . 94
8.3 Case study: Prevention of thermal runaway propagation . . . 105

9 Review and Outlook 113
9.1 Review of results using Primary Component Analysis (PCA) and response surfaces . . . 113
9.2 Critical review and limitations . . . 118
9.3 Concluding remarks and further perspective . . . 119

References 121

List of Figures 133

List of Tables 137

Glossary

Accelerated Rate Calorimetry (ARC)

A calorimetry method designed to track thermal (and pressure) properties of exothermal reactions, such as battery heat release or battery abuse tests.

Battery Electric Vehicle (BEV)

An electric vehicle, which solely relies on an onboard battery as energy source for propulsion.

Battery Management System (BMS)

The technical unit referred to as Battery Management System includes hard- and software which manages, supervises and actively controls a rechargeable battery. It collects and evaluates data on voltage levels and temperatures and protects the system from leaving its safe operating area. The data obtained from the BMS can be used for reporting or be combined with external components as the vehicle bus system.

Battery Thermal Management System (BTMS)

The umbrella term "Battery Thermal Management System" integrates all technical components that are used in order to keep a battery element within its intended operational temperature range. Depending on the application this comprises cooling and/or heating assemblies.

Differential Scanning Calorimetry (DSC)

A calorimetry technique which relies on the comparison of the specimen's behavior with a known probe, in order to determine the probe's specific heat capacity or its latent heat storage capability

Heating Ventialtion Airconditioning (HVAC)

In the automotive context, HVAC describes the subassembly used for conditioning and/or heating of air directed to the cabin or in case of air cooled batteries, the battery department.

Phase Change Material (PCM)

A substance featuring a significant heat of fusion, which can technically be used for storing thermal energy. During the phase change large amounts of heat are absorbed, respectively released, at an almost constant tempeature

Plugin Hybrid Electric Vehicle (PHEV)

An electric vehicle, which features both, an internal combustion engine and a rechargable battery, which can be charged by external sources, e.g. charging stations

Primary Component Analysis (PCA)

Primary Component Analysis is a statistical method, based on orthogonal transformation. With the help of the PCA large sets of (experimental) observations can be screened for correlated values. Based on the result a set of linearly uncorrelated variables can be identified and further evaluated.

Solid Electrolyte Interface (SEI)

The Solid Electrolyte Interface is an electrically insulating but ion-conducting solid layer formed on the electrodes of Lithium Ion Batteries.

State of Charge (SOC)

The State of Charge is an indication for the remaining usable energy content of batteries, in relation to their nominal or actual full capacity

State of Health (SOH)

The term State of Health describes the actual status of a battery (system) compared to ideal condition. Several parameters add to its calculation. Remaining capacity, internal resistance and OCV are usually considered.

Stationary Energy Storage (SES)

Batteries or other electrical storage systems, used to store energy for stationary applications, e.g. grid stabilization or storage of renewable energy. SES devices can be connected to the grid or be operated within isolated networks

Thermal Runaway (TR)

Describes the self-accelerating process, which occurs when excess heat origining from exothermic reactions can not be dissipated and itself leads to an temperature increase triggering further reactions

Abbreviations

ANSYS	Analysis System
APDL	ANSYS Parametric Design Language
ARC	Accelerated Rate Calorimetry
BEV	Battery Electric Vehicle
BMS	Battery Management System
BTMS	Battery Thermal Management System
CCCV	Constant Current Constant Voltage
CFRP	Carbon Fibre Reinforced Plastic
COP	Coefficient of Performance
DSC	Differential Scanning Calorimetry
HVAC	Heating Ventilation Airconditioning
ICE	Internal Combustion Engine
LFP	Lithium Iron Phosphate
LIB	Lithium Ion Battery
NCA	Nickel Cobalt Aluminum Oxide
NMC	Nickel Manganese Cobalt Oxide
OC	Overcharge
PCA	Primary Component Analysis
PCM	Phase Change Material
PHEV	Plugin Hybrid Electric Vehicle
PV	Photovoltaics
PVC	Polyvinyl Chloride
RTD	Resistance Temperature Device

SC	Short Circuit
SEI	Solid Electrolyte Interface
SEM	Scanning Electron Microscope
SES	Stationary Energy Storage
SOC	State Of Charge
SOH	State Of Health
TCS	Thermochemical Storage
TPS	Transient Plane Source
TR	Thermal Runaway

Formula Symbols

A	Area in m^2
E_A	Activation energy in $\frac{J}{mol}$
d	Depth in m
ρ	Density in $\frac{kg}{m^3}$
ϵ	Emissivity
H	Enthalpy in J
η_{sys}	System efficiency
h	Heat transfer coefficient in $\frac{W}{m^2K}$
ν	Kinematic viscosity in $\frac{kg}{m \cdot s}$
l	Length in m
λ	Thermal conductivity in $\frac{W}{mK}$
$\lambda_\perp$	Thermal conductivity cross-plane in $\frac{W}{mK}$
$\lambda_\parallel$	Thermal conductivity in-plane in $\frac{W}{mK}$
L	Latent heat in $\frac{kJ}{kg}$
m	Mass in kg
Nu	Nusselt number
P_{el}	Power, electrical in W
P	Power (electrical/thermal) in W
Pr	Prandtl number
$\dot{Q}$	Heat flux in $\frac{J}{s}$
Re	Reynolds number
k	Reaction rate in $\frac{mol}{Ls}$
α	Resistance temperature coefficient in $\frac{1}{K}$
c_p	Specific heat capacity in $\frac{J}{kgK}$
T	Temperature in K
w	Width in m
w_{air}	Air speed in $\frac{m}{s}$
W_{el}	Work, electrical in J

1 Introduction and Motivation

Driven by global trends as portable electronic devices, temporary storage of renewable energy and the electrification of vehicle drive-trains, Lithium Ion Batteries (LIBs) have evolved from a niche technology to one of the key components in numerous applications. However, those batteries are complex systems, which on the one hand come in countless sizes, form formats and chemistry, but on the other hand all face similar challenges. Their properties, behavior, performance and safety are very sensitive towards ambient conditions, especially temperature [53]. Hence, detailed understanding of those correlations and the development of proper supporting battery system technology is of utmost importance for the broad and sustainable success of battery systems.

Against the background of a rapdily increasing number of systems in the field and the integration of batteries into security relevant applications as aerospace and medical engineering, development of efficient, economic and safe Battery Thermal Management Systems (BTMSs) is a highly prevailling field of interest. It directly affects the value those systems add and has seen huge improvements over the last years. Nevertheless, unfortunate incidents as the Boeing Dreamliner case [155] or a series of EVs catching fire [146] in a dramatic way show, that there is still need for enhancement in terms of thermal safety and reliability.

As media coverage focuses on such fatal events, proper thermal management is not only a technical requirement, but also highly decisive for public acceptance of new technologies e.g. Battery Electric Vehicles (BEVs). The gain in importance on issues related to BTMS is reflected by the steep increase in research activities that results in a highly increased number of publications linked to the topic. Figure 1.1 depicts the count of scientific journal articles featuring thermal keywords, published within the Journal of Power Sources.

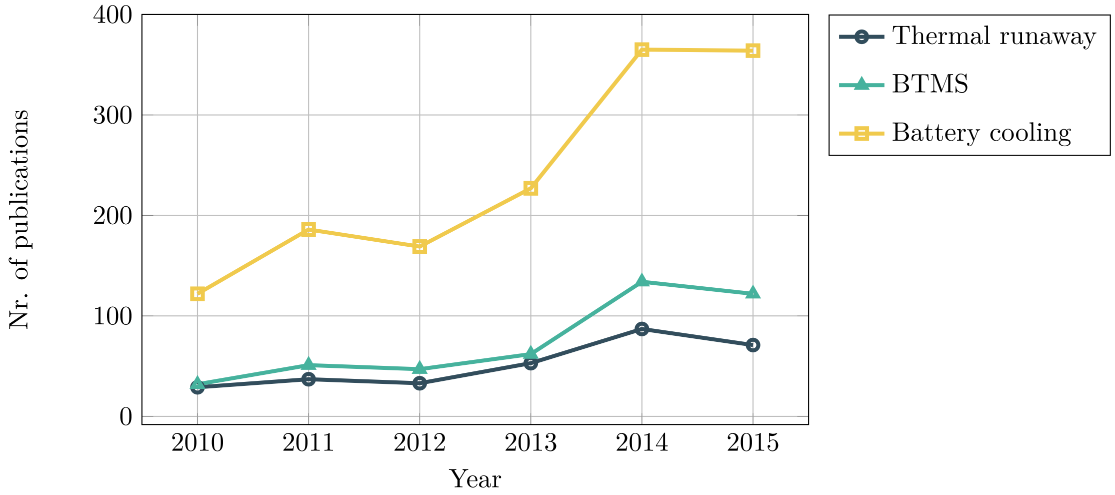

Figure 1.1: Development of publication numbers based on thermal keywords [72]

1.1 Battery market development and trends

Since their commercial launch in the 1990s LIBs have seen a significant increase in sales and are considered to remain the dominant energy storage technology for most automotive and stationary applications over the next ten to fifteen years [34]. As shown in figure 1.2, market size in terms of production volume, energy content and economic value has significantly increased between 2005 and 2015. The compound anual growth rate currently lies at approximately 15% and is supposed to develop further. Alone during the year 2015 approximately six billion LIB cells, with a total usable capacity of more than 60 GWh have been produced and integrated into electric vehicles, stationary storage systems and portable electronic devices [135]. Most recent studies see a global production volume for 2025 in the range of 170 to 180 GWh [95] [115].

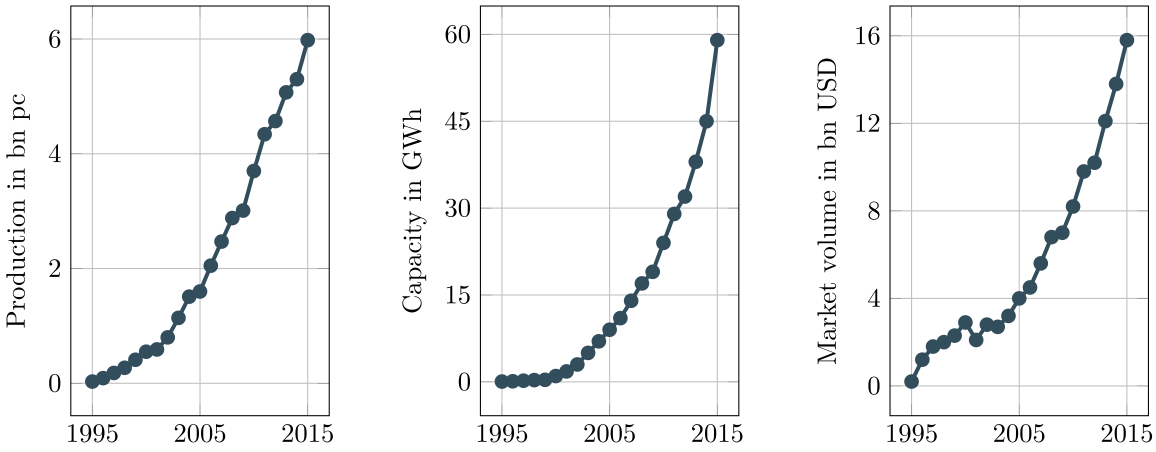

Figure 1.2: Global LIB market trends by year on cell level [135]

Besides the absolute production volume, also the average energy content and the size of battery packs has continuously increased over the past years. The customer driven trend towards high-range BEVs and Plugin Hybrid Electric Vehicles (PHEVs) comes along with larger and more complex battery packs, which can consist of several thousand cells and a network of an according number of cells connected in serial and parallel [15]. Another key trend that is clearly visible and of major influence in order to overcome range anxiety are shorter charging times. As for most applications voltage levels are limited (e.g. the 400V semi-standard in most automotive systems), fast charging is mainly achieved by higher currents [108]. Average charging power of BEVs has steadily increased [70] and premium vehicles as the Tesla Model S, already today allow to charge the battery pack with DC currents of up to 300 A, utilizing a proprietary system. Nevertheless, as part of the efforts towards standardization, the recently approved "Level 3 fast charging" defined in the SAE J1772 standard also allows currents of up to 400 A [120].

As chapters 2 to 4 will show, the combination of more complex battery systems and significantly increased charging currents leads to high thermal losses, reduced efficiency and hence more challenging tasks for BTMS, especially in terms of peak temperature, temperature spread and uniformity.

1.2 Importance of Battery Thermal Management

Application aspects

Due to the electrochemical nature of all common battery types, thermal operation conditions, especially temperature level and temperature distribution have significant impact on battery performance, lifetime and safety. Therefore huge efforts have been put into designing highly sophisticated BTMS, which are presented in more detail in chapter 4. As most of those systems are actively driven and accordingly consume electric energy, their operation leads to a decrease in overall system efficiency. This is of particular interest for automotive applications where the electric consumption of BTMS components reduces the achievable driving range. However, the negative impact is also omnipresent for stationary energy storage systems, as their sustainability and profitability is affected by the power required to thermally manage the core battery, too.

The magnitude of this impact can be derived from figure 1.3. Simulation data is obtained for a mid-sized all-electric vehicle performing the identical driving cycle under varying ambient conditions. In order to consider only the negative impact of battery thermal management and ensure comparable results, cabin thermal management is completely switched off and all auxiliary loads are set to exactly identical settings. Even under these conditions, the power demand for BTMS reduces the vehicle's driving range as much as more than 25 % from 307 km to 230 km. As in real life cabin climatization further adds to the energy consumption for the cold and hot temperature ranges, the negative effect is even further increased. A more detailed explanation of the vehicle energy model and the assumptions regarding thermal management is found in chapter 8.1

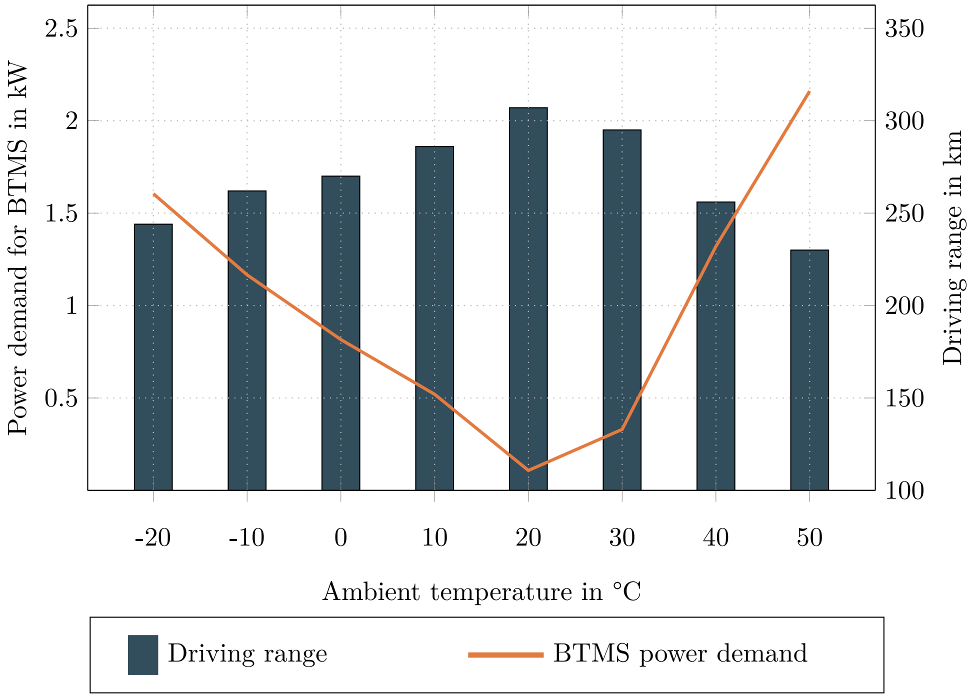

Figure 1.3: Impact of ambient temperature on BTMS energy demand and driving range

Economic and integration aspects

As a consequence of the trend towards high energy and high power battery cells as well as larger battery packs, the cost share of cell components and cell manufacturing for the whole pack is increasing as depicted in figure 1.4. Since at the same time, for customer acceptance the overall price of battery packs has to be further reduced, all system technology components, including BTMS are facing immense cost pressure. Hence, novel smart, but simple solutions are required and requested by industry.

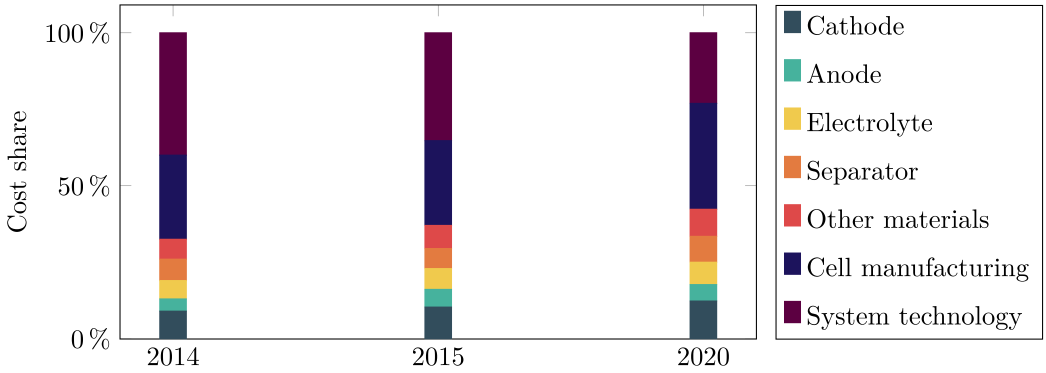

Figure 1.4: Cost composition of automotive Li-ion battery packs [135]

In automotive applications heavy and voluminous battery packs also challenge conventional packaging concepts within the vehicle and further reduce the space available for BTMS components. Besides weight and volume, system complexity is also a critical issue. Though BTMS only accounts for a small share of system volume and weight, it adds almost 30% on the overall part count. Shares of the individual functional components are exemplarily given for a water cooled 52 kWh BEV battery pack in figure 1.5. Further details on main components of state of the art systems can be found in sections 4 and 8.1.

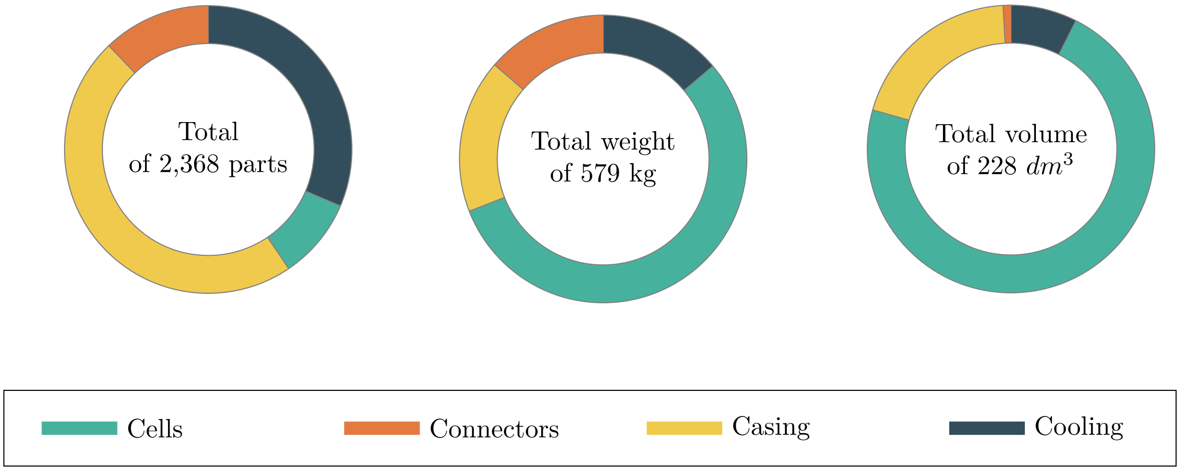

Figure 1.5: Volume and weight distribution of battery pack components as used in EVA electric vehicle (see section 8.1)

1.3 Scope and approach

For both, price pressure and weight or volume constraints, new concepts for battery thermal management are subject of extensive research. Due to the significant negative impact of active systems on the overall efficiency (e.g. usable capacity/driving range), but also noise exposure and error proneness, passive systems are considered as promising new concept. Among others in particular the integration of latent heat storage material into battery systems has gained researcher's and industry's attention. The basic principle is already common in other fields as building climatization, well understood and only has to be transferred to battery applications. In order to do so, further application oriented research is required. Within the presented work, the possible impact of adding phase change materials into battery packs and the resulting consequences are evaluated. After highlighting the most influential thermal parameters of LIBs typical state of the art BTMS solutions are presented and evaluated in terms of quality and efficiency. As an objective comparison between the conventional concepts and the PCM approach shall be ensured, a reference setup and a cooling efficiency factor are introduced. In the main part, an overview over the range of suitable PCMs is given before material candidates are selected with respect to the specific battery requirements. Experimental procedures and simulation models for PCM characterization are introduced, establishing a sound basis for the following quantitative studies. The impact of PCM is highlighted with the help of three real-life case studies following the approach according to figure 1.6. From the results gathered, a critical conclusion is drawn and guidelines for adapting and designing passive PCM based BTMS are derived.

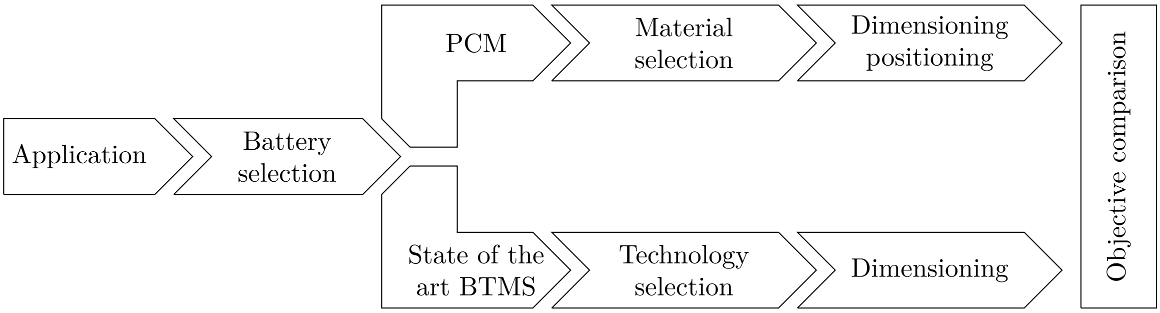

Figure 1.6: Systematic approach for case study evaluation

The main scope of this study is to contribute answers to the following questions:

- What are the applications most suitable for PCM integration?
- Which PCM is the best fit for each of the identified battery applications?
- How big is the impact of PCM integration on cooling efficiency and aging?
- Are there significant differences in terms of safety or reliability between conventional technologies and cooling via PCM?
- How can a proper operation strategy further enhance the benefits of passive cooling?
- Which PCM design parameters affect the individual applications the most?

2 Sensitivity of Lithium Ion Batteries towards temperature

The LIB core process of converting chemical energy into electrical energy and vice versa is highly temperature sensitive and hence limited to a narrow operation window, typically inbetween -20 °C and 50 °C. While falling below a certain temperature results in sluggish reaction rates and can also destroy the battery cell - e.g. by frozen electrolyte [127] - exceeding the allowed battery temperature is even more critical, as it puts the battery cell at risk of an unwanted self accelerating exothermal reaction, known as Thermal Runaway (TR) [131].

But even within the given temperature limits, besides State Of Charge (SOC) and State Of Health (SOH), temperature is the most influential state variable. As charging and discharging operation of batteries goes along with numerous endothermal and exothermal reactions, cell temperature is not only dependent on ambient conditions, but also on the battery's internal structure and the load profile. Thus temperature level and internal temperature distribution within the battery cell strongly vary over time and transiently affect virtually all of its characteristics [121].

The corresponding effects can be instantly visible for the available power and capacity, but are also highly present for slower processes as self discharge or aging mechanisms. After all, a change in temperature level caused by operating the cell has an impact on local resistance, reaction rate etc. and hence heat generation itself. As effects can occur locally, e.g. at welding spots, or points of high current density, temperature distribution in the cell normally can not be considered to be uniform, especially for high current load cycles [36].

All of these effects can superpose each other and cause changes in performance, lifetime and operational safety, with some of them even leading to total loss of the cell including potentially fatal consequences. The dominating effects can be traced back to the temperature dependancy of reaction rates, electrical and ionic conductivity and diffusion processes [6]. For efficient and safe BTMS design, all these effects must be well understood and depicted in analytical or numerical models. Those models can then be used as a starting point for designing and dimensioning the proper BTMS layout.

In the following section, all of the most decisive effects are explained in more detail and substantiated with actual data obtained from experiments conducted with a 60 Ah pouch cell of NMC chemistry. Further details on the investigated cells can be found in section 3.5.

Reaction rates and equilibrium

As the rate of electron transfer reaction can be estimated by the exponential Arrhenius equation (2.1), already small changes in temperature have significant consequences on its level [78]. With the reaction constant k_0 and the molar gas constant R being constants and the activation energy E_A only showing very limited temperature dependancy, the temperature T is clearly the dominating factor. Reactions typical in LIB batteries feature activation energies in the range of $50\frac{kJ}{mol}$, so that a temperature rise of approximately 10 K already results in a doubled reaction rate k [71].

$$k = k_0 exp\left(-\frac{E_A}{R \cdot T}\right) \tag{2.1}$$

As by nature the reverse reaction is present as well, but features slightly different temperature dependancy, also the equilibrium and hence the open circuit voltage is a function of temperature. For detailed information on the individual activation energies, models and methods to determine them, work by Okubo [110] and Birkl [11] are recommended readings.

Mechanical and electrical material properties

Not only the chemical reactions, but also the material properties of battery components are a function of temperature. This includes thermomechanical properties as density, E modulus and specific heat capacity, but also electrical properties as the ohmic resistance. As particularly the resistance has major impact on the battery performance, a linear approximate solution for the individual components based on a material specific temperature coefficient α is given in equation 2.2.

$$R_i\left(T\right) = R_{i,0}\left[1 + \alpha_i\left(T - T_0\right)\right] \tag{2.2}$$

While for metallic cell components α_i is positive and hence resistance increases with temperature, the electrolyte shows an opposite behavior. As for most cells, overall resistance is dominated by the electrolyte's share, also the cell resistance's temperature coefficient α_{cell} is negative for virtually all battery types. Total resistance hence decreases with elevated temperatures. Experimentally obtained values for the sample cell, using the real part of the 1 kHz AC impedance are presented in figure 2.1.

Diffusion processes

In addition to the electrical conduction, diffusion processes play an important role for battery cell's behavior. At this point especially diffusion within the electrolyte is considered most influential and can be approximated by the Stokes-Einstein equation for diffusion in liquids and solids [112]. Boltzmann constant k_B and particle radius r are virtually temperature independent, the dynamic viscosity η

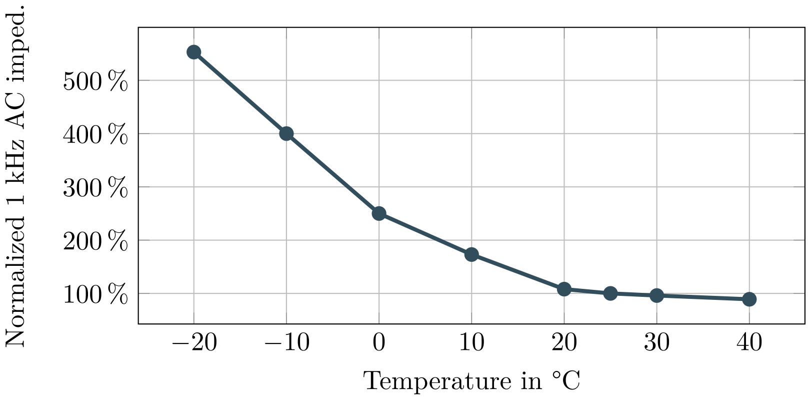

Figure 2.1: Internal 1 kHz AC impedance vs. temperature

typically decreases with elevated temperatures. Hence, again a positive direct correlation of diffusivity D and temperature T is given by equation 2.3.

$$D = \frac{k_B \cdot T}{6 \cdot \pi \cdot \eta \cdot r} \tag{2.3}$$

Temperature uniformity

Local inhomogenities inside the battery cell and the position of power connectors at two distinctive points result in a highly non-uniform temperature field. Two of the most obvious temperature inhomogeneity effects can be traced back to the current distribution. As in proximity to the cell terminals, current flow density is highest, also at this area, temperature level can be expected to be higher than at the most remote points of the cell. Furthermore, due to the fact that current collectors at anode and cathode side are made of different material - mostly copper on the anode side, and aluminum on the cathode - there is a difference in ohmic resistance and hence heat generation [13]. Both effects are always present but most obvious for elevated current levels, as can be seen in figure 2.2.

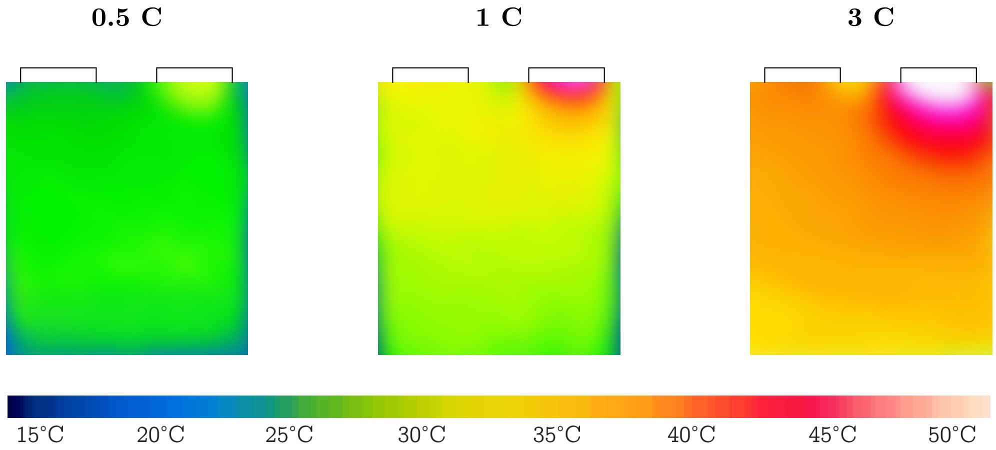

Figure 2.2: Extent of temperature spread within one cell dependent on C rate

Thermal images are obtained at the surface of a 60 Ah NMC pouch cell, at the end of the constant current phase of a Constant Current Constant Voltage (CCCV) charge sequence, performed at different C rates. For the measurements cells have been vertically mounted inside a climate chamber set to 25 °C and hence are subject to a moderate forced convection.

When dealing with multi-cell systems as battery modules or packs, not only the temperature spread within the individual cells is of interest, but also the temperature spread in between the single cells. The position of the cell within the battery pack, e.g. the proximity to cooling plates or ambient air has major impact on temperature. Figure 2.3 depicts an infrared thermography of the uneven distribution and the surface temperature curve along a linescan across the width (A=0 to B=1). Data is obtained at the end of a charging period conducted at a C-rate of 1. The battery pack has been operated inside a cooling chamber set to 25 °C and the pack is actively cooled by liquid plates with an inlet temperature of 15 °C. Results point at a distinct temperature peak of the cells loacted in the middle of the pack. As the performance of cells connected in series is limited by the weakest element, those persistent differences in temperature lead to deviating aging behavior and finally a decrease in system performance. In order to limit this effect, for practical use, a maximum temperature spread of 5 K is widely considered as desirable [114].

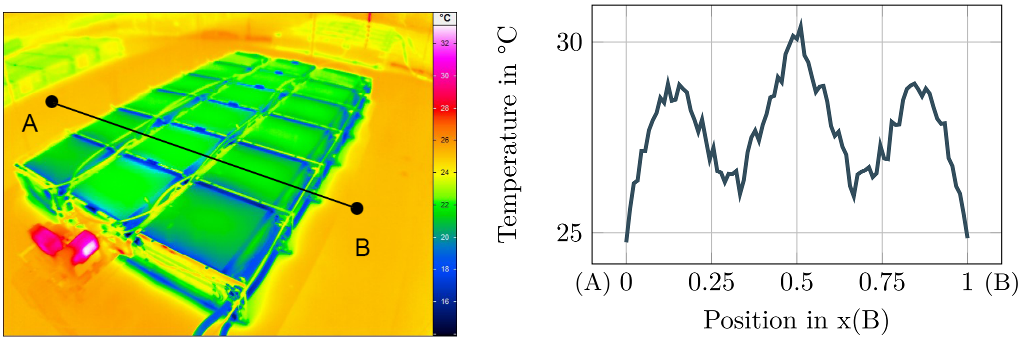

Figure 2.3: Extent of temperature spread within a battery pack after 1 C charge

2.1 Capacity and capacity fade

The precedent sections have shown that elevated temperatures come along with accelerated reaction rates, decreased resistance and improved diffusion. The combination of these effects leads to faster and more efficient charge/discharge processes, resulting in an increased usable capacity [90]. Hence, within certain ranges, usable capacity can be estimated as a linear function of battery temperature. An exemplary correlation of temperature, C rate and usable capacity for the investigated 60 Ah NMC pouch cell is given in figure 2.4 and equation 2.4. Before the actual capacity determination, all cells have been fully charged at a C-rate of 0.5 and an uniform temperature of 25 °C.

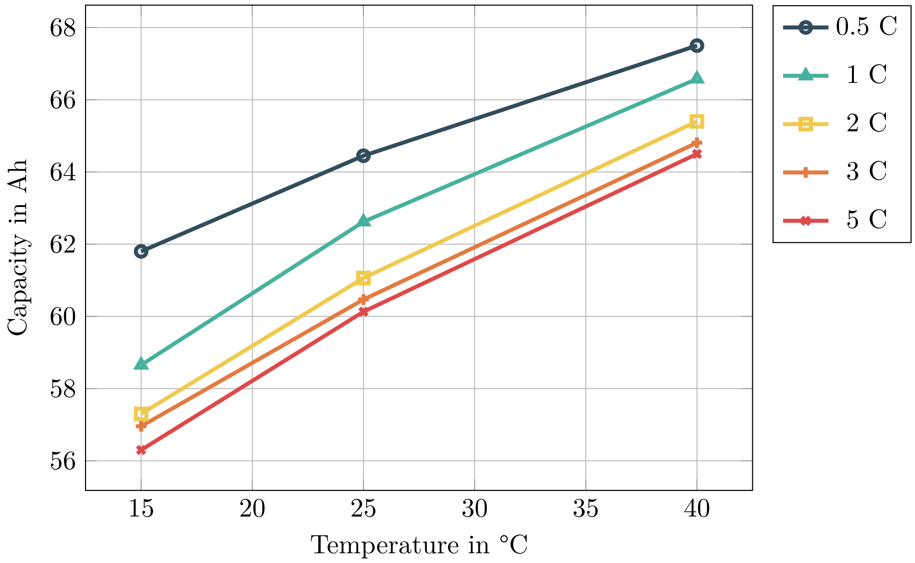

Figure 2.4: Usable capacity of a 60 Ah NMC pouch cell as function of C rate and ambient temperature

$$C = C_0 + \alpha\,(40 - T) \tag{2.4}$$

However, elevated temperatures also accelerate unwanted side reactions, leading to reversible and irreversible capacity loss. In this context, loss of cycleable lithium, dissolution of active material into the electrolyte, electrolyte oxidation and degradation of the negative electrode are considererd to be most influential [6], [132]. As side reactions also follow the Arrhenius scheme, within certain temperature ranges a linear dependancy of capacity loss and temperature can also be observed. Waldmann et al. have shown that there are two distinct areas of low and high temperature that are most influential [144]. Figure 2.5 depicts the capacity fade for continuous cycling with a CCCV charging and discharging rate of 1 C at different temperatures.

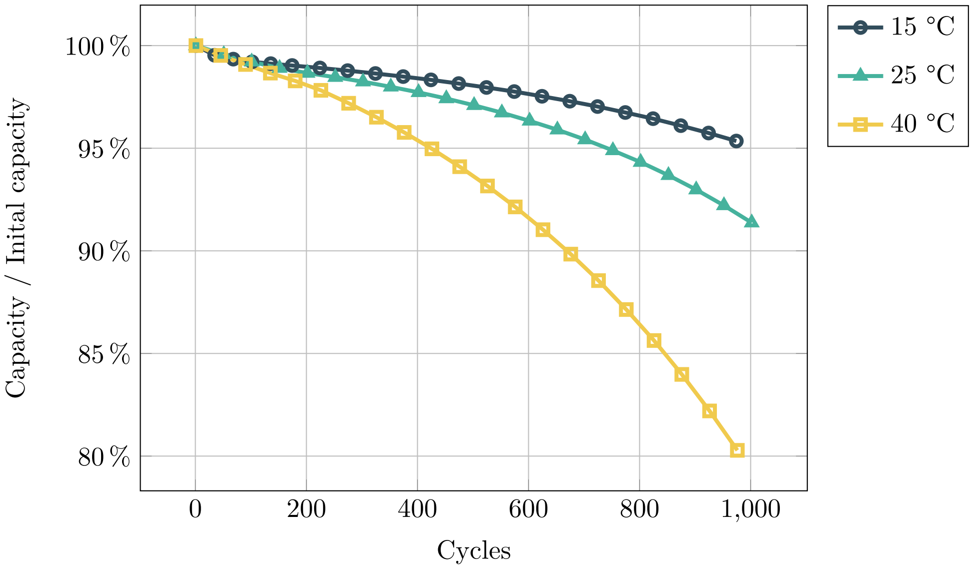

Figure 2.5: Cyclic irreversible capacity fade at 1C/1C as a function of ambient temperature

Irreversible capacity fade also occurs without the cells being cycled, referred to as calendaric aging. Also in this scenario, besides the SOC, storage temperature is the main parameter affecting the speed of the degradation the most. Irreversible consumption of cycleable lithium into the Solid Electrolyte Interface (SEI) layer formation accounts for the major part of the observed capacity loss. According to experimental studies with NMC cells, loss of positive active material and electrolyte decomposition also take place, but only have a minor impact [132]. Experimental values for the selected 60 Ah NMC pouch cell are presented in figure 2.6.

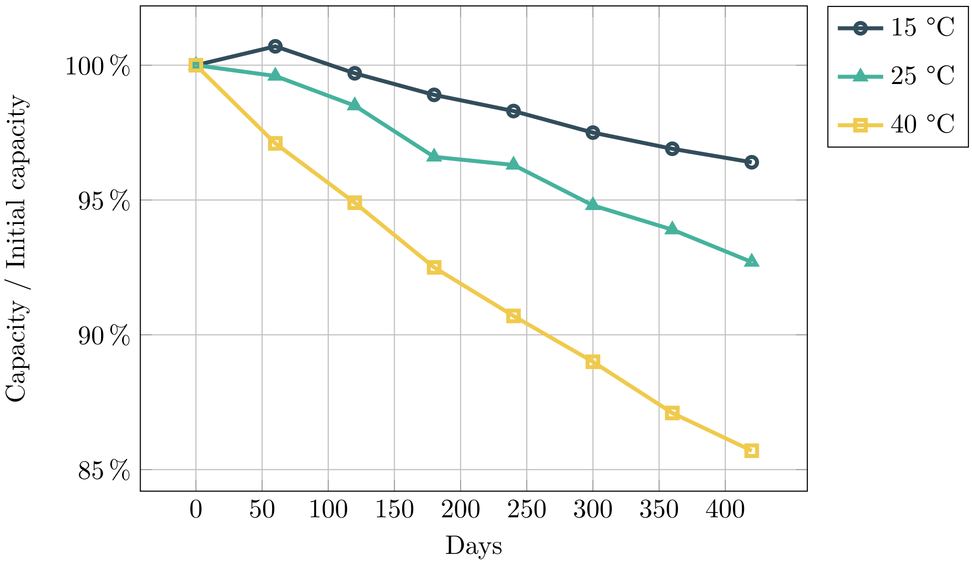

Figure 2.6: Irreversible capacity loss of a 60 Ah NMC pouch cell during soaking at 50 % SOC

2.2 Power and power fade

The amount of available power can be the decisive limit for many operations and is hence another key specification of a battery cell. In virtually all cells reduced power capability is directly linked to a growth in impedance, which is highly dependent on ambient temperature [132] [14].

High temperatures over longer time lead to an increase in ohmic resistance, caused amongst others by electrolyte decomposition. Passive film formation, adhesion and local corrosion affect the current collectors and further accelerate this effect [48] [13]. Investigations of Thomas et al. [136] have shown that power fade is highly temperature dependent and can be divided into two phases. Within the presented study internal resistance has been determined according to the VDA standards [126]. The according current step method is based on one constant current discharge pulse of 18 seconds and a following charge pulse of 10 seconds duration. Experimental data for increase in resistance over charge-throughput respectively soaking time are exemplary given in figure 2.7 and figure 2.8 for a 60 Ah NMC pouch cell.

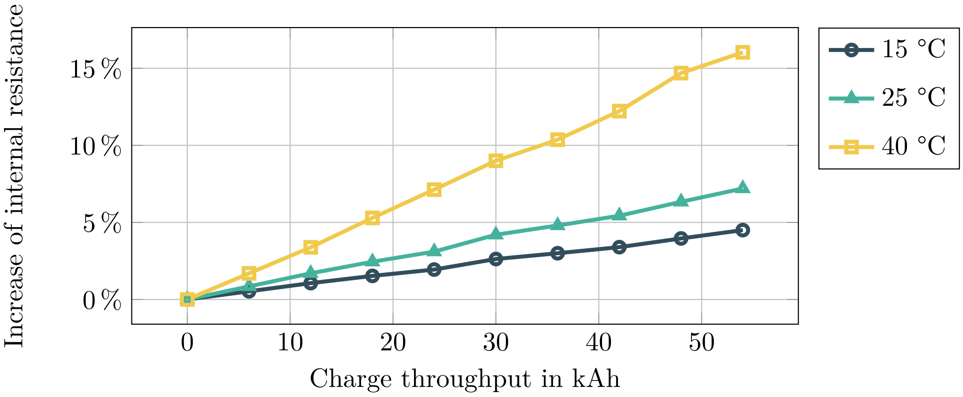

Figure 2.7: Increase of internal resistance (VDA current step) of a 60 Ah NMC pouch cell over charge throughput

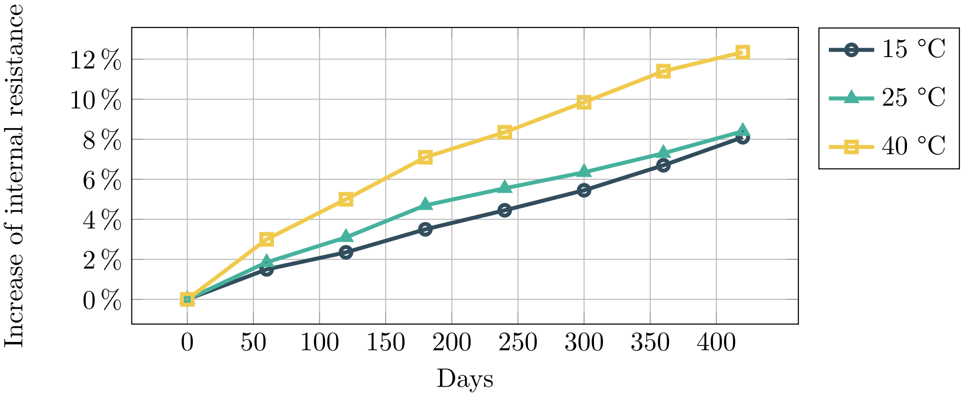

Figure 2.8: Increase of internal resistance (VDA current step) of a 60 Ah NMC pouch cell during soaking at 50 % SOC

2.3 Reversible self-discharge

When stored for a longer period of time, cells do not only undergo irreversible aging processes in form of passivation, but also reversibly loose a certain amount of the stored energy. Driving force for this phenomena is the fact that electrodes are not completely passivated by the SEI. As a result, electrons and ions can transcend and reduce usable net energy. The process is accelerated by higher temperatures, as diffusion is sped up and ions can be dissolved more easily [160]. At very high temperatures, also mechanical stress can lead to damages within the SEI and a further increased reaction. Measured temperature dependent self-discharge rates over a six months period are presented for two temperature levels in figure 2.9. The significant change in incline between the first and second months might be originating from the superposition of irreversible calendar aging mechanisms, that add to the measured loss of charge. As only one cell per time frame has been evaluated, variations in build quality between the cells might have compounded the effect.

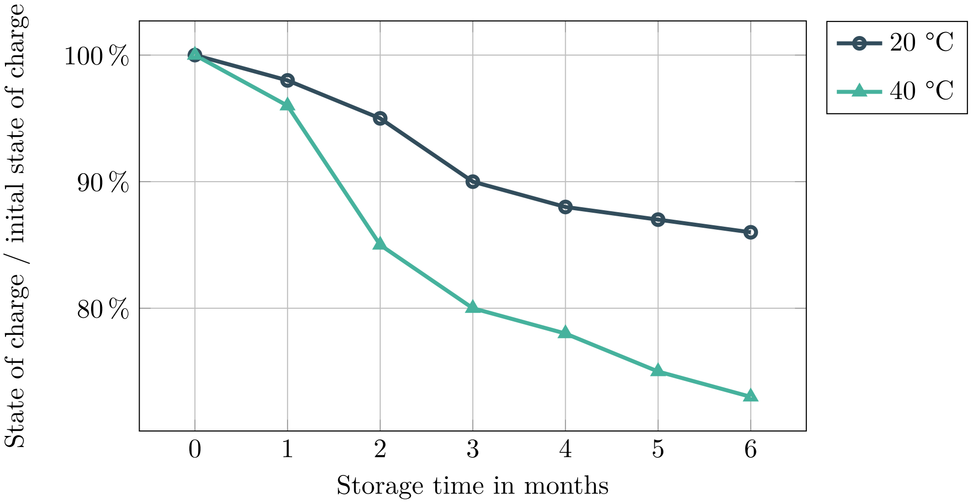

Figure 2.9: Self-discharge of a 60 Ah NMC pouch cell at different storage temperatures

2.4 Low temperature behavior and lithium plating

Not only temperatures above a certain limit, but also cold temperature are critical for battery system operation. Similar to overheating, also subcooling can not only limit performance and capacity but also completely prevent operation or cause irreversible damage. In particular charging at low temperature is still a huge challenge for most common battery types [164].

Especially for temperatures below 0 °C, reduced ionic conductivity and limited diffusivity of lithium ions lead to a significant loss of available energy and power [164], as can be exemplarily seen in figure 2.10. All sample cells have been charged at 25 °C with C-rates of 0.5 but show differing discharge behavior depending on discharging temperature. Impact can be reduced by adding special additives to the electrolyte, which then, however, also affect the behavior under moderate temperature. Hence, this approach is only suitable for very specific applications as e.g. for batteries used for satellites [145]. In most use cases as in electric vehicles proper insulation against ambient and an active heating system are first choice.

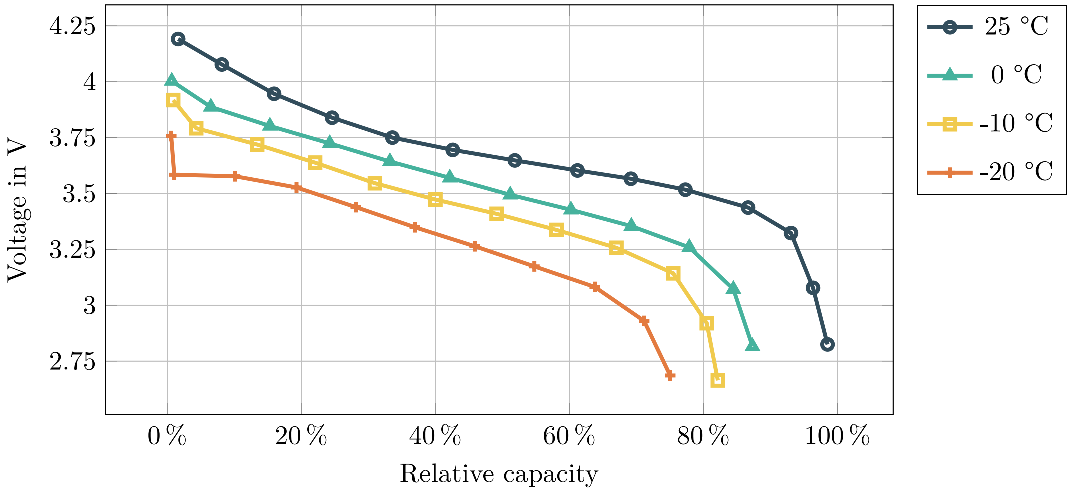

Figure 2.10: Low temperature performance of a 60 Ah NMC pouch cell at 0.5 C charge/discharge

Besides the already mentioned effects, there is another highly temperature dependent aging process, typical for cells with graphite based anodes. Caused by the deposition of metallic lithium at the graphite anode, lithium plating can lead to significant loss of capacity, and in severe cases even trigger internal short circuits [31]. Cells are especially prone to lithium plating when charged at high rate and low temperature. Depending on the load profile and the used cell type, plating can already occur at moderate temperatures above 20 °C [125]. Additives to the electrolyte can reduce the plating risk to a certain extent, but the general effect remains present and highly critical for lifetime. Experimental data presented in figure 2.11 demonstrates the rapid degradation of a battery deliberately forced into lithium plating by fast charging at low temperature. The corresponding 60 Ah NMC cells have been cycled between 3.0V and 4.1V solely with CC fast-charging at 3 C. Discharging loads resemble the driving profile presented in section 8.1. More detailed studies on the mechanisms of lithium plating can be found inter alia in [42], [129] and [165].

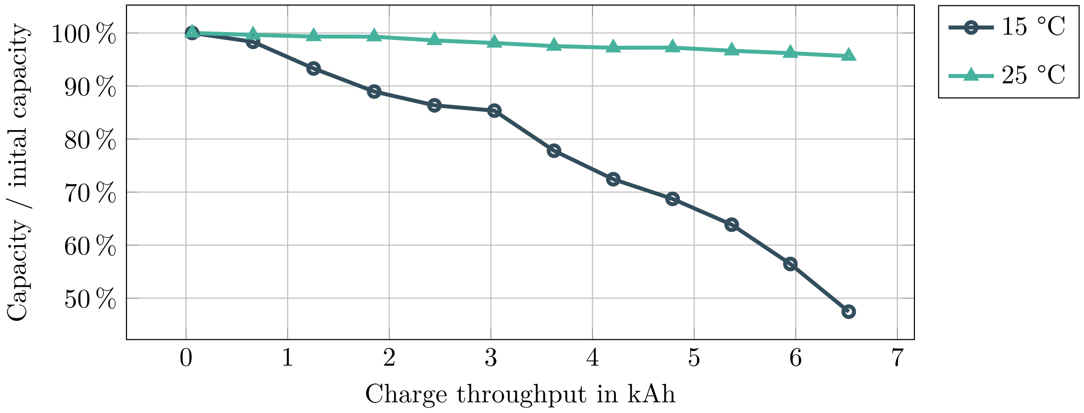

Figure 2.11: Impact of lithium plating during low temperature fast charge

2.5 Thermal runaway

At a certain onset temperature level exothermic reactions inside the battery cell release more heat than can be dissipated to the ambient, which can then lead to an irreversible self accelerating heating, referred to as Thermal Runaway (TR). Among the reactions triggering or accelerating TR are: thermal decomposition of the electrolyte, thermal decomposition of the anode or cathode, reduction of the electrolyte by the anode, oxidation of the electrolyte by the cathode and finally internal shorts caused by melting of the separator [146]. As possible consequences include gassing, fire and explosion, excess of the onset temperature has to be prevented under all circumstances and with a sufficient safety threshold.

In order to identify the onset temperature experimentally, cells can be placed inside a rigid oven or examined by Accelerated Rate Calorimetry (ARC). In both cases, the sample is heated up stepwise and held at constant temperature for a certain amount of time in order to identify any self-heating. If no exothermal reaction of the cell is present, temperature is elevated again to the next step. The result of an experiment conducted with this so called "heat-wait-search"-method, is given in figure 2.12.

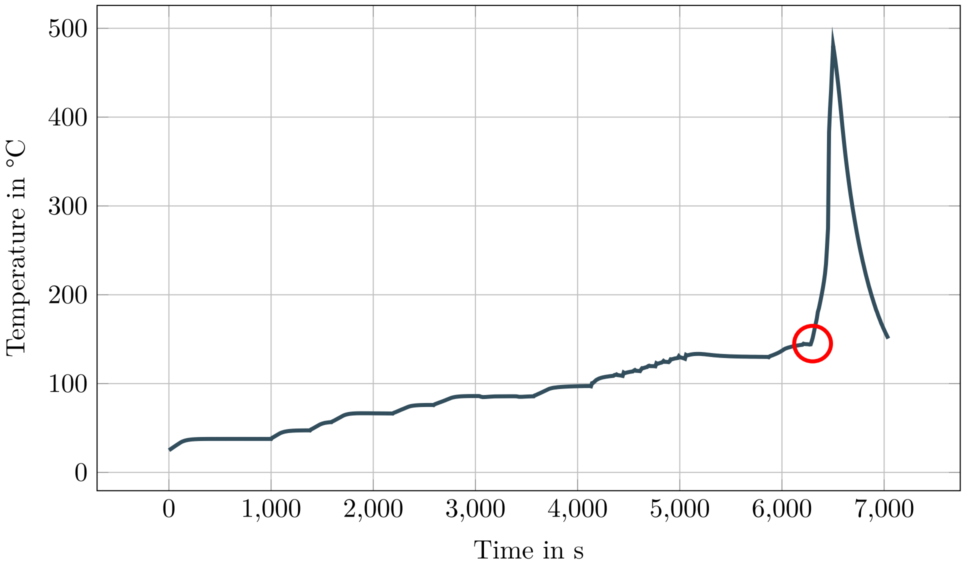

Figure 2.12: Triggered Thermal Runaway (heat-wait-search method)

Once the onset temperature is exceeded for a critical time, course of action is barely to be stopped as the triggered processes release further heat. However, there are measures of cell design, as the use of additives to the electrolyte, that can help to suppress thermal runaway [99], [27]. More detailed information and an insight on the correlation between onset temperature and cell chemistry is given in chapter 3.4 and in literature [44], [118], [51].

2.6 Summary of cell thermal sensitivity

The precedent sections have highlighted the sensitivity of LIB cells towards temperature and its impact on their performance, lifetime and safety. Table 2.1 summarizes the fundamental causal dependencies valid for most cell types and gives an overview on the resulting design goals.

Table 2.1: Overview on thermal dependencies

Criteria	**Effect of low temperature**	**Effect of elevated temperature**	**Design goal**
Usable capacity	↘	↗	↗
Usable power	↘	↗	↗
Internal resistance	↗	↘	↘
Capacity fade (aging)	↘	↗	↘
Power fade (aging)	↘	↗	↘
Self-discharge	↘	↗	↘
Risk of lithium plating	↗	↘	↘
Risk of thermal runaway	↘	↗	↘

Based on experimental observations and extended life-cycle analysis, as e.g. in [111], table 2.2 gives an overview on the typical recommended operating conditions for LIBs of different cell chemistry, as they can be found in literature.

Table 2.2: Operating conditions of common cell types as found in literature [142], [161], [71], [9]

Criteria	**NCA**	**NMC**	**LFP**
Min. storage temperature	-30 °C	-20 °C	-40 °C
Max. storage temperature	60 °C	50 °C	65 °C
Min. charging temperature	0 °C	0 °C	0 °C
Max. charging temperature	40 °C	45 °C	60 °C
Min. discharging temperature	-30 °C	-30 °C	-20 °C
Max. discharging temperature	60 °C	60 °C	60 °C

3 Battery thermal characteristics

For proper understanding of thermal battery pack behavior and the according layout of the BTMS, as well as for calorimetric heat generation measurements and for creation of simulation models, material parameters of the specific battery cell have to be at hand. Obtaining those values can be challenging, as Maleki et al. [96] have shown that physical properties are not only dependent on temperature, but also on SOC. In the following, an overview on the dominant parameters, selected exemplary values and the most common analytic and experimental methods to obtain them are given. Wherever experimental values have been recorded with one of the sample cells, they are listed in the respective section.

3.1 Specific heat

The specific heat of a material or a heterogenous compound of materials can be seen as capability to store thermal energy. It links the amount of heat stored to the according temperature rise and hence determines the dynamic thermal behavior of a sample. Whereas for pure materials values are widely available in literature [5], for compound structures as battery cells, values have to be obtained analytically or experimentally.

Analytic determination

If the internal structure of a battery cell is known, heat capacity can be analytically determined by the mass weighted sum of its components according to equation 3.1. Exemplary values for materials common in lithium ion cells are given in table 3.1 at a temperature of 25 °C, though noting that exact values can be difficult to obtain.

$$c_{p,Batt}\left(T\right) = \frac{\sum_{n=1}^{N} m_n \cdot c_{p,n}\left(T\right)}{\sum_{n=1}^{N} m_n} \tag{3.1}$$

Even with the components' material data being known, the fact that the internal layout and the mass fraction of the single components are not publicly available impede a reliable estimation. Hence, for a valid analytic study, cells have to be opened in order to examine their content. For the three batteries utilized within the presented work, such an examination was conducted within a glove box (Figure 3.1 showing the process). As volatility of the electrolyte complicates direct weighing, its mass is calculated from the weight difference between intact cell and remaining components. The calculated c_p values, representing a first estimation, are given in table 3.2.

Table 3.1: Specific heat capacity of selected materials common in LIBs

Material	**Component**	**Density** $\frac{g}{cm^3}$	**Spec. heat capacity** $\frac{J}{gK}$	**Source**
Graphite	Anode	2.1	0.71	[5], [16]
$LiNi_{1/3}Mn_{1/3}Co_{1/3}O_2$	Cathode	4.9	0.85	[46], [25]
$LiNi_{0.8}Co_{0.15}Al_{0.05}O_2$	Cathode	5.1	0.72	[158], [25], [93]
$LiFePO_4$	Cathode	3.6	0.74	[106], [24]
Organic electrolyte (EC)	Electrolyte	1.13	2.06	[21]
Microporous polymer	Separator	1.4	1.551	[74]
Aluminum	Current collector	2.70	0.90	[5]
Copper	Current collector	8.93	0.39	[5]

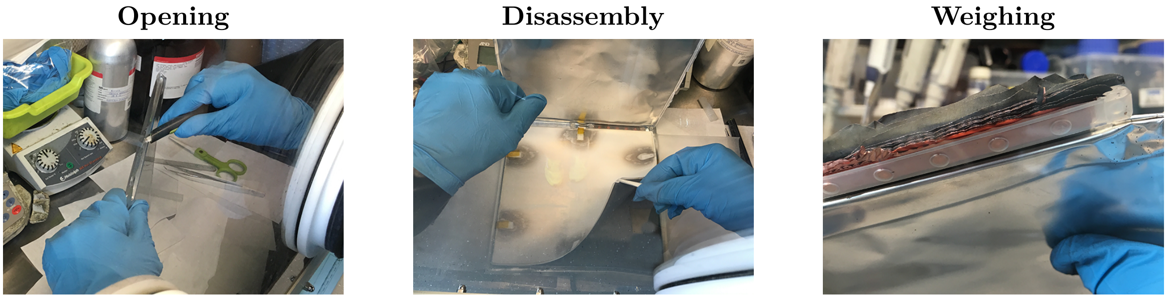
Opening **Disassembly** **Weighing**

Figure 3.1: Process of dissasembly and weighing of cell components

However, for nearly all commercial cells, internal structure and material properties, especially for the electrolyte, are not available. Hence, the compound specific heat capacity can not be analytically estimated exactly, but has to be obtained experimentally. Therefore, whole cells or even modules can be surveyed with the help of a calorimeter.

Adiabatic calorimetry

For adiabatic calorimetry a predefined constant heating power $\dot{Q}_{heater}$ is applied to the battery cell for a certain time $\Delta t = (t_{n+1} - t_n)$, resulting in a temperature rise $\Delta T = (T_{n+1} - T_n)$, as depicted in figure 3.2. With the calorimeter's heat capacity being known and the assumption of perfect insulation towards the ambiance, heat capacity as a function of temperature can be derived within only one single measurement according to equation 3.2. For the following experiments a THT EV-ARC has been utilized. As table 3.3 shows, analytically and experimentally determined values are aligned and show only slight deviation below 10 %. The observed discrepancies could have arisen form the fact,

Table 3.2: Specific heat capacity calculated from individual cell components

Property	**NCA**	**NMC**	**LFP**
Form format	cyl.	pouch	cyl.
Nominal capacity in Ah	42	60	3
Casing (Aluminum): mass in g	100	n.a.	16
Casing (Pouch foil): mass in g	n.a.	85	n.a.
Current collector (Aluminum): mass in g	50	85	4
Current collector (Copper): mass in g	60	119	10
Active material cathode: mass in g	280	465	24
Active material anode: mass in g	260	412	16
Separator: mass in g	22	41	2
Electrolyte: mass in g	28	299	19
Estimated spec. heat capacity c_p in $\frac{J}{gK}$	**0.72**	**0.91**	**0.89**

that binders and additives are not taken into account and electrolyte composition is not exactly known. Measuring inaccuracies of the calorimeter further add to the error. Values stated are the average of at least three individual measurements. For the following investigations and as material data for the simulation models the measured values are used.

$$c_{p,T} = \frac{\dot{Q}_{heater} \cdot \Delta t}{m \cdot (T_{n+1} - T_n)} \tag{3.2}$$

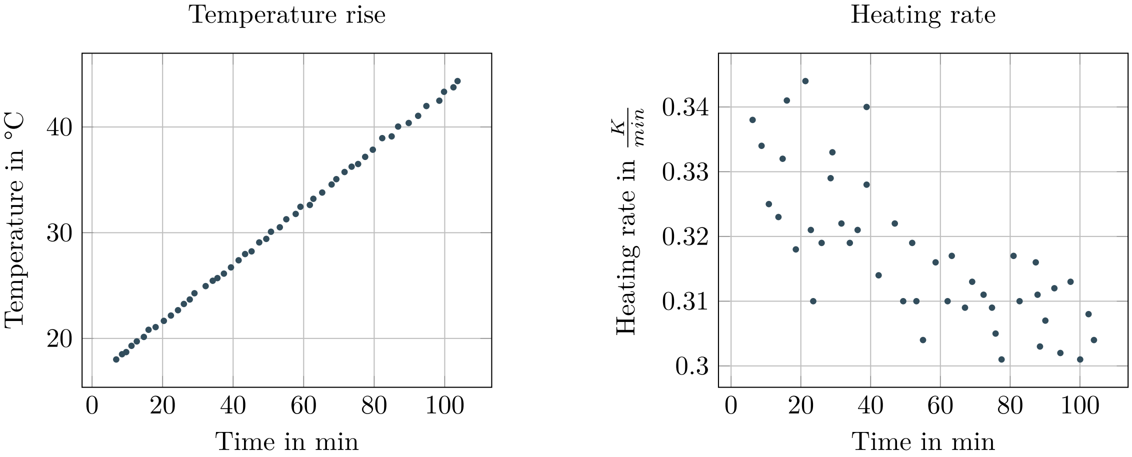

Figure 3.2: Result data of a calorimetric heat capacity determination

Table 3.3: Specific heat capacity calculated from individual cell components

	NCA	**NMC**	**LFP**
Measured spec. heat capacity c_p in $\frac{J}{gK}$	**0.79**	**0.83**	**0.88**
Relative deviation to calculated values	8.2 %	8.8%	1.1%

3.2 Thermal conductivity

Thermal conductivity defines the capability of a material to conduct heat from internal or external heat sources to heat sinks. In battery context this refers to the heat path from heat generation inside the cell to the ambient or the cooling system. Especially for larger battery cells and high power applications, the conductivity of this path can be the crucial factor, limiting the maximum allowable heat generation and therefore the maximum achievable power. For a given geometry (A/l) and temperature spread ΔT, heat flux within a homogeneous body only depends on its thermal conductivity λ according to equation 3.3.

$$\dot{Q} = \lambda \cdot \frac{A \cdot \Delta T}{l} \tag{3.3}$$

For heterogeneous materials or bodies being combined out of several components, another parameter is preferable: The value of thermal resistance, generally being defined as in equation 3.4. For homogeneous bodies of constant cross section, it can be easily derived from the thermal conductivity with the help of equation 3.5.

$$R_{th} = \frac{\Delta T}{\dot{Q}} \tag{3.4}$$

$$R_{th} = \frac{l}{\lambda \cdot A} \tag{3.5}$$

Using the equivalency to electrical networks, heat flux paths and their conductivity can be modeled as a network of parallel and serial thermal resistances. The system's total resistance can then be obtained according to figures and equations in table 3.4. As battery cells feature a layered design, thermal conductivities in perpendicular directions highly differ. Hence, values of in-plane $\left(\lambda_{\|}\right)$ and cross-plane conductivity $(\lambda_{\perp})$ vary by orders of magnitude. Values for individual cell components and material compounds have been determined amongst others by Maleki, Zhang and Drake [96]. An overview on selected values available in literature is presented in table 3.5.

Based on those values and experimental data on thickness and quantity of the individual layers, thermal conductivity can be estimated with the help of the analogies summarized in table 3.4. Results of such an estimation are given for the three investigated cells in table 3.7.

Table 3.4: Analogy between thermal and electrical network

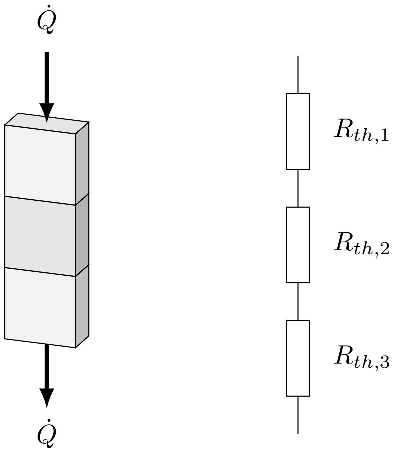	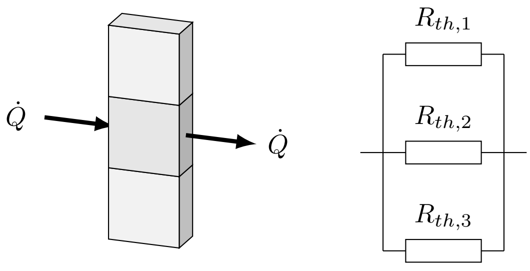

$$R_{th,tot} = R_{th,1} + R_{th,2} + R_{th,3} \qquad (3.6)$$

$$R_{th,tot} = \frac{1}{R_{th,1} + R_{th,2} + R_{th,3}} \qquad (3.7)$$

Table 3.5: Thermal conductivity of selected materials common in LIBs

Material	**Component**	**Thermal conductivity** $\frac{W}{mK}$	**Source**
Graphite	Anode	15.11 [1]	[96]
$LiNi_{1/3}Mn_{1/3}Co_{1/3}O_2$	Cathode	0.687 [1]	[46]
$LiNi_{0.8}Co_{0.15}Al_{0.05}O_2$	Cathode	0.72 [1]	[158]
$LiFePO_4$	Cathode	0.741 [1]	[106]
Organic electrolyte	Electrolyte	4.2	[3], [97]
Polymer	Separator	0.35 [1]	[74], [97]
Aluminum	Current collector	230	[22], [140]
Copper	Current collector	397	[22], [140]

---

[1] Values are given for wet electrodes and separator, soaked with electrolyte

Table 3.6: Properties of individual cell layers

Property	**NCA**	**NMC**	**LFP**
Anode active material thickness in mm	**0.085**	**0.06**	**0.16**
Anode current collector thickness in mm	**0.01**	**0.015**	**0.008**
Cathode active material thickness in mm	**0.09**	**0.08**	**0.16**
Cathode current collector thickness in mm	**0.02**	**0.02**	**0.015**
Separator thickness in mm	**0.05**	**0.05**	**0.025**
Number of layers/windings	**37**	**31**	**22**

Table 3.7: Thermal conductivity estimations

Property	**NCA**	**NMC**	**LFP**
Estimated cross-plane th. conductivity $\lambda_{\perp}$ in $\frac{W}{mK}$	**0.93**	**0.79**	**1.26**
Estimated in-plane th. conductivity $\lambda_{\parallel}$ in $\frac{W}{mK}$	**15.6**	**19.37**	**27.5**

For the analytic determination of the thermal conductivity, the same restrictions as for the specific heat regarding unknown geometry and composition apply. Accordingly, experimental determination is necessary for unknown material samples or in order to validate analytic estimations.

Steady State method

Especially for larger samples thermal conductivity can be obtained by a steady state experiment. The unknown sample is therefore placed between two identical reference materials, with one being heated, the other one being cooled. After a certain time, the system reaches equilibrium, with the temperature difference being stable. With the known heat flux $\dot{q}$ and the measured temperature difference dT, the sample's thermal conductivity can be estimated based on the Fourier law according to equation 3.8. As a heat source a resistance heating foil with a maximum power of 200 W has been attached to the cell, temperature rise is recorded at the center part of the cell's opposite area using a high precision thin film PT-1000 thermo probe, read by an Ahlborn data logger. Initial temperature is equal to the ambient temperature of 25 °C. The experiment setup and recorded data samples for a measurement conducted with a 60 Ah NMC pouch cell are depicted in figure 3.3 and figure 3.4 respectively.

$$\lambda = -\dot{q} \cdot \frac{dx}{dT} \qquad (3.8)$$

Due to parasitic heat losses, the long time to reach equilibrium and sensor uncertainties, the method is rather difficult to handle and, in particular, not suitable for small, non-uniform samples as cylindrical battery cells. Hence, in the following, another preferable experimental technique is used.

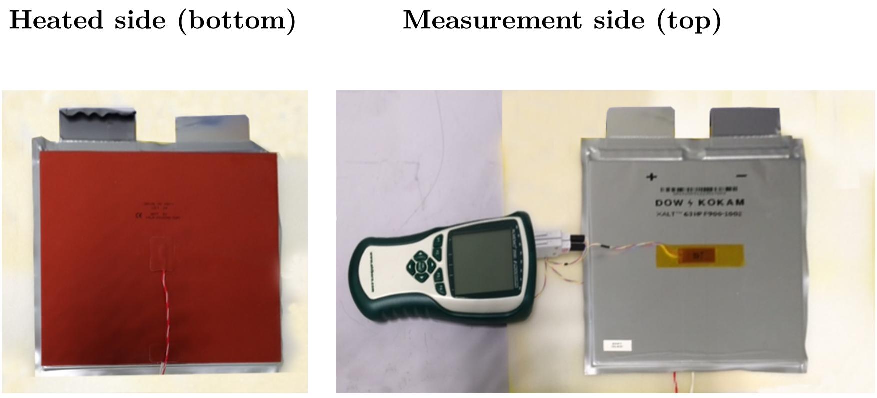

Heated side (bottom)

Measurement side (top)

Figure 3.3: Process of steady state $\lambda_\perp$ determination applied to a 60 Ah NMC pouch cell

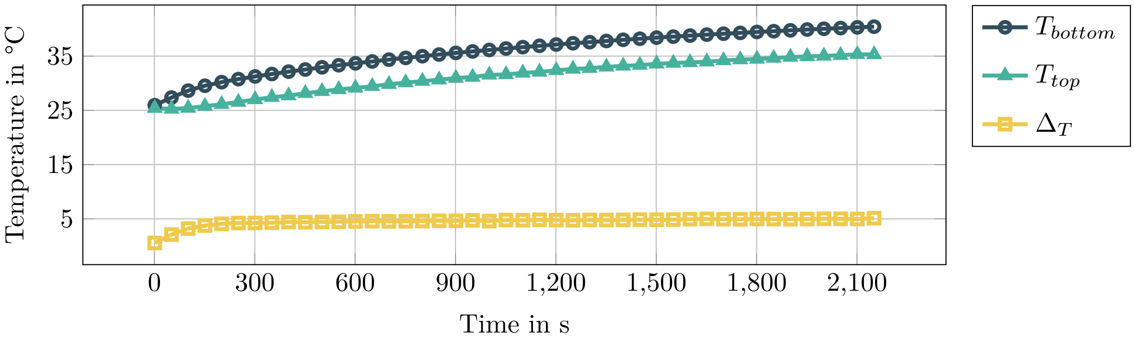

Figure 3.4: Measurement data of steady state methodology

Table 3.8: Result data - steady state measurements on 60 Ah NMC cell

Property	**Measured value**
Measurement time t in s	2182
Equilibrium temperature delta ΔT in °C	5.1
End temperature bottom T_{bottom} in °C	35.4
End temperature top T_{top} in °C	40.5
Calculated th. conductivity $\lambda_\perp$ in $\frac{W}{mK}$	0.39

Transient plane source method

The method chosen to measure anisotropic thermal conductivity within the following is referred to as Transient Plane Source (TPS) method or Hot Disk method. It is based on a very thin double nickel spiral, which is mounted in between two identical samples of the probed material. Alternatively the sensor can also be placed in between the sample and a well isolating layer, resulting in a one-sided measurement. In both cases, with constant power being applied to the spiral and parallel measurement of the spiral's resistance, the sensor acts as heater and temperature probe at the same time [52]. Before the actual measurement is started, temperature drift is recorded for 40 seconds, in order to ensure that there is no parasitic heat flux influencing the measurement. Results of such a drift measurement are presented in the left portion of figure 3.6. This way, the following temperature rise $\Delta T_s(\tau)$, quoted for a normalized time τ only depends on the applied heating power P_0, the sensor's radius r and the material's capability to conduct thermal energy as equation 3.9 shows. Hence, measuring the temperature increase at high resolution, leads to the volumetric heat capacity and the thermal conductivity [55]. If the material's thermal conductivity is identical in two directions, but highly differs in the third one, as e.g. for layered samples, also anisotropic measurements can be conducted with the TPS method using equation 3.10.

$$\Delta T_s(\tau) = \frac{P_0}{\pi^{\frac{3}{2}} \cdot r \cdot \lambda} \cdot D(\tau) \quad (3.9)$$

$$\Delta T_s(\tau_x) = \frac{P_0}{\pi^{\frac{3}{2}} \cdot r \cdot (\lambda_x \lambda_z)^{\frac{1}{2}}} \cdot D(\tau_x) \quad (3.10)$$

A typical experimental setup is shown in figure 3.5 and measured raw data is depicted in figure 3.6. The resulting thermal conductivity values for the three reference cells are summarized in table 3.9.

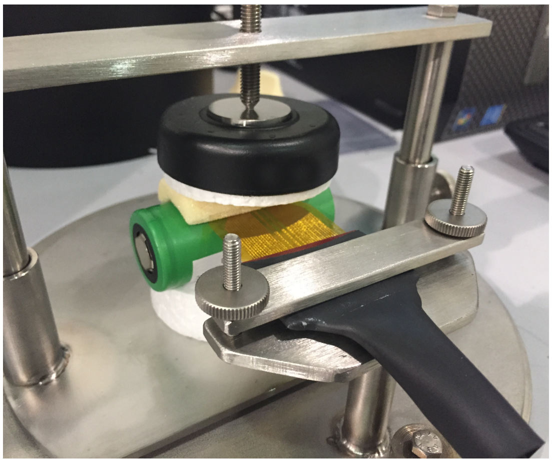

Figure 3.5: Experimental setup for a one-sided TPS measurement on a cylindrical LFP cell

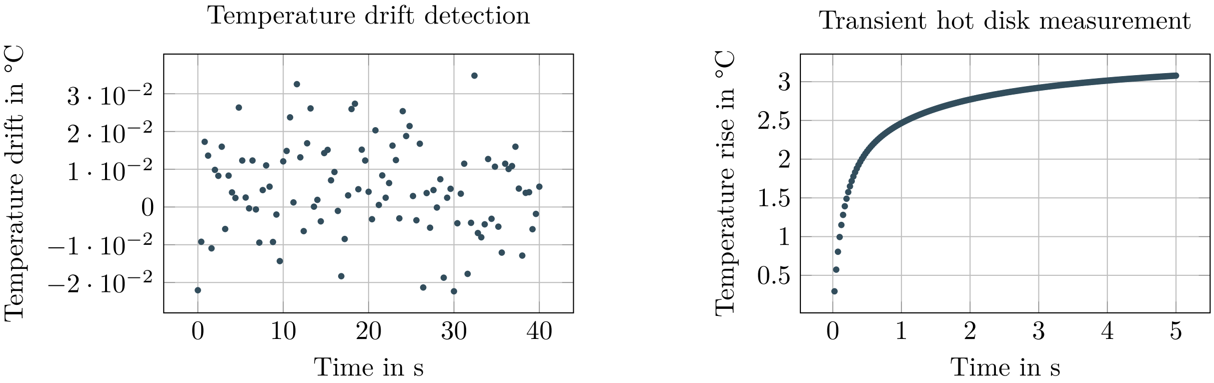

Figure 3.6: Result data of TPS thermal conductivity determination

Table 3.9: Thermal conductivity values obtained via TPS method

	NCA	**NMC**	**LFP**
Measured cross-plane th. conductivity in $\frac{W}{mK}$	**0.985**	**0.83**	**1.13**
Relative deviation to calculated values	5.6 %	4.8 %	11.5 %
Measured in-plane th. conductivity in $\frac{W}{mK}$	**17.2**	**19.71**	**23.94**
Relative deviation to calculated values	9.3 %	1.7 %	14.9 %

The considerable derivations between estimated and measured λ values of up to 15 % point at the difficulty in their reliable experimental determination.

3.3 Heat generation rate

Heat generated in LIBs originates from four sources: Activation, transport of species, reaction entropy and ohmic losses. According to Bernardi, the amount of heat generated is given as in equation 3.11 [10]. While the first term describes the electrical power, the second term originates from the producible reversible heat and the entropic heating. The third and fourth term describe the heat produced from mixing and phase change respectively. For virtually all applications, the heat generated due to the resistance of current passage $I\left(U-V\right)$ and entropic heating are dominant, and hence contribution of mixing and phase change can often be neglected [137]. In its resulting simplified form, according to equation 3.12, Bernardi's model is one of the most commonly used models for small cells [6]. However, the approach neglects the Joule heating within the current collectors, which can have significant impact, especially for larger BEV cells.

$$\begin{aligned} q = -IV - \sum_{l} I_l T^2 \frac{d\frac{U_{l,avg}}{T}}{dT} + \sum_{j} \frac{d}{dt}\left[\int_{v_j} \sum_{i} c_{i,j} RT^2 \frac{\delta}{\delta T} ln\left(\frac{\gamma_{i,j}}{\gamma_{i,j}^{avg}}\right) dv_j\right] + \\ \sum_{i,j\neq m}\sum_{i}\left[\left(\Delta H^0_{i,j\rightarrow m} - RT^2 \frac{d}{dT} ln \frac{\gamma_{i,m}^{avg}}{\gamma_i, j^{avg}}\right)\frac{dn_{i,j}}{dt}\right] \end{aligned} \tag{3.11}$$

$$q = I\left(U-V\right) - I\left(T\frac{\partial U}{\partial T}\right) \tag{3.12}$$

Effects highlighted in the precedent section lead to a temperature variation during operation which depends on the ambient conditions, the cell's material properties and mass as well as the heat generation q. It can be estimated as shown in equation 3.13.

$$\frac{\mathrm{d}T}{\mathrm{d}t} = \frac{q - hA_{surf}\left(T_{surf} - T_{amb}\right)}{mc_p}$$

Given the material properties as specific heat c_p, as well as the heat transfer coefficient h, the cell surface A_{surf}, the ambient temperature T_{amb} and tracking the temperature profile of the cell, heat generated q can be experimentally obtained.

Among the primary methods for determining these values is the ARC, which allows fast temperature tracking and recording of transient heat generation. Results of numerous adiabatic measurements on the 60 Ah pouch cell are given in figure 3.7 and figure 3.8. Temperatures are recorded at the center of the cell surface during constant current charge and discharge phases of different C rates.

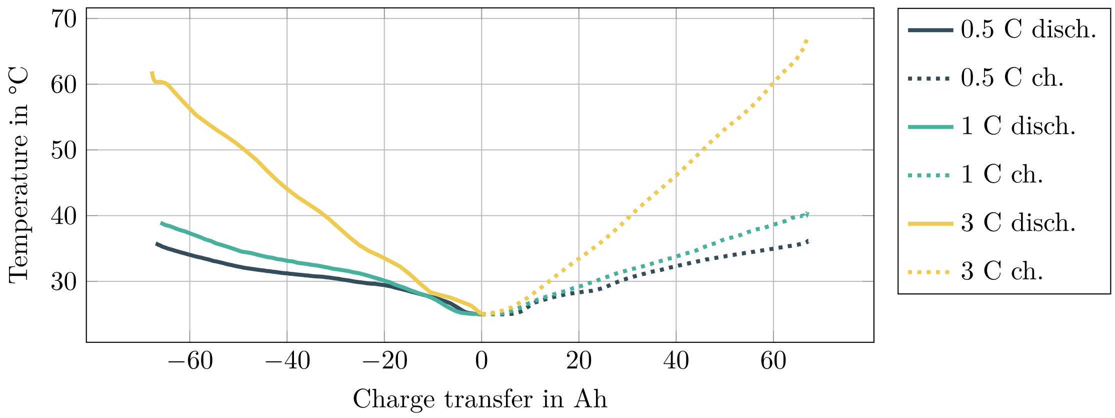

Figure 3.7: Temperature of a 60 Ah NMC cell cycled at different C rates under adiabatic conditions

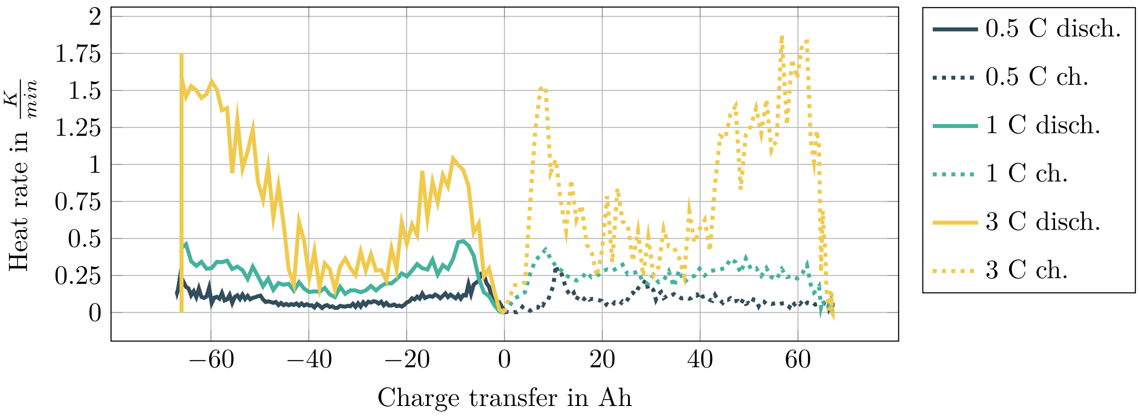

Figure 3.8: Heat rate of a 60 Ah NMC cell cycled at different C rates under adiabatic conditions

As can be seen in the measured data and literature, heat generation is highly dependent on SOC and the C rate [92]. For lower currents, a more distinct difference between charging and discharging can be observed, which can be traced back to entropy effects. When cycled with higher C-rates this effect fades as it is superposed by the other heat generation mechanisms. These correlations allow first estimations for cooling demand. Real life applications, however, virtually never show constant C rates. Especially during discharge they rather follow a certain current profile. In order to facilitate basic dimensioning of thermal management systems, a time-averaged heat release can be calculated and transformed into a thermal efficiency of the cell. Therefore, the heat energy Q_{th} is put into relation with the electric energy transfer to or from the cell W_{el} . Average thermal power released from the cell can then be calculated accordingly pursuant equation 3.14

$$\eta_{Batt,th} = 1 - \frac{Q_{th}}{W_{el}} \tag{3.14}$$

Table 3.10 highlights the significant differences between load profiles of stationary and automotive applications, the corresponding heat generation and hence thermal efficiency values.

Table 3.10: Typical cycle data for exemplary automotive and stationary load profiles

	Current profile	
	Stationary storage application	Automotive application (fast charge)
	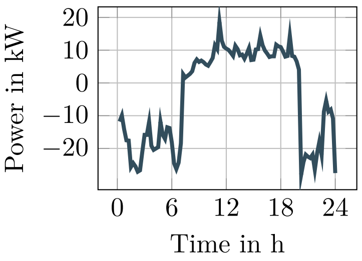	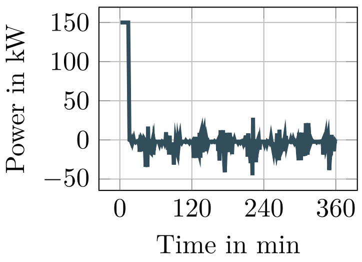
Nominal system capacity	250 kWh	52 kWh
Cycle time	24 h	6 h
Min. cont. current	-1 CA	-10 CA
Max. cont. current	1 CA	3 CA
Av. current charge	0.08 CA	2.5 CA
Av. current discharge	0.05 CA	0.135 CA
Charge transferred per cycle W_{el}	350 kWh	60 kWh
	Heat generation rate (based on ARC experiments)	
	Stationary storage application	Automotive application (fast charge)
	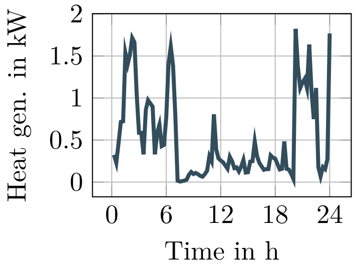	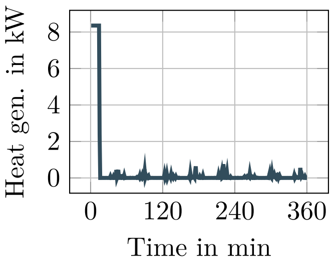
Max. heat-gen	1.82 kW	8.35 kW
Av. heat-gen	0.52 kW	0.78 kW
Total heat release Q_{th}	12.5 kWh	4.7 kWh
Overall $\eta_{Batt,th}$	96.4 %	92.2 %

3.4 Onset temperature

As described in section 2.5, nearly all cells feature a certain temperature that leads to self-accelerating exothermic reactions, resulting in an irreversible loss and severe consequences as fire or explosion. Hence, the so called onset temperature has to be very well known, when designing thermal management systems. As different cell types clearly differ in onset temperature level and vehemence of reaction, experiments or physicochemical simulations are used for characterization.

Heat-Wait-Search method

In order to identify the starting point of the exothermic reaction and quantify the energy of the TR, the so called heat-wait-search method is widely used [148], [128]. Onset temperature and beginning of TR are considered, once the exothermal self heating of the cell surpasses 0.2 K/min [53]. Figure 3.9 displays the overlain data of heat-wait-search experiments for cells of different chemistry and format. The corresponding temperature levels are presented in table 3.11.

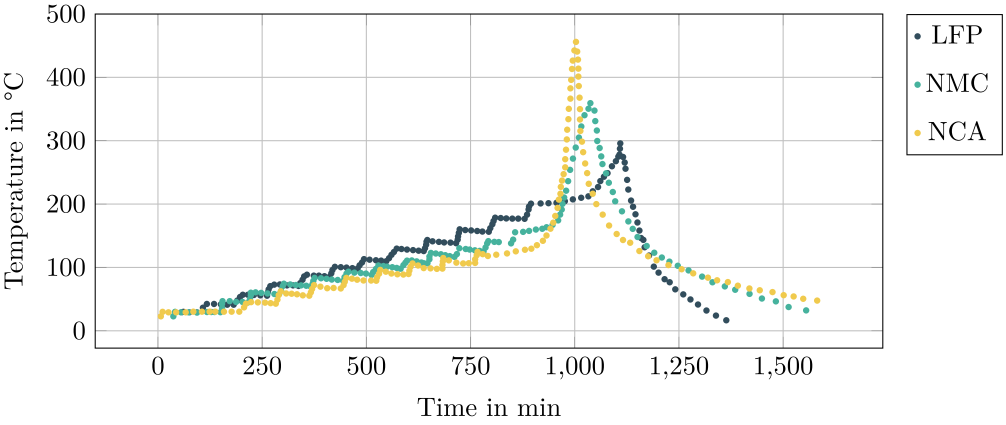

Figure 3.9: Heat-wait-search study for different cell types

Table 3.11: Exemplaric onset temperature values for selected cells

	NCA	**NMC**	**LFP**
Measured onset temperature in °C	**130**	**154**	**198**

3.5 Overview on experimental values for selected cells

Within the presented study, an universal approach of a passive thermal management concept should be highlighted and validated by real-life case studies. In order to represent a wide range of cell types, three cells have been selected. Their thermal properties are given in table 3.12. Data resembles average, minimum and maximum values of all conducted measurements.

Table 3.12: Overview on properties of selected cell types

	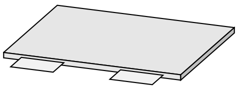	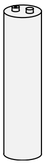	
Manufacturer	Dow Kokam LLC	Saft S.A.	Sony
Model	F900-0002	VL 41M	US26650FTC1
Form factor	Pouch	Cylindrical	Cylindrical
Dimensions	266 mm x 263 mm x 10.7 mm	ø 54.3 mm x 222 mm	ø 26.25 mm x 65.40 mm
Chemistry	NMC	NCA	LFP
Nominal voltage	3.7 V	3.6 V	3.2 V
Operating voltage	2.7 - 4.2 V	2.7 - 4.0 V	2.0 V - 3.65 V
Nominal capacity	60.0 Ah	41.0 Ah	3.0 Ah
Max. charge current	180 A	150 A	2.85 A
Max. d.charge current	480 A	150 A	20 A
Weight	1.49 kg	1.07 kg	0.085 kg
Grav. power density	1790 W/kg	794 W/kg	753 W/kg
Grav. energy density	149 Wh/kg	136 Wh/kg	113 Wh/kg

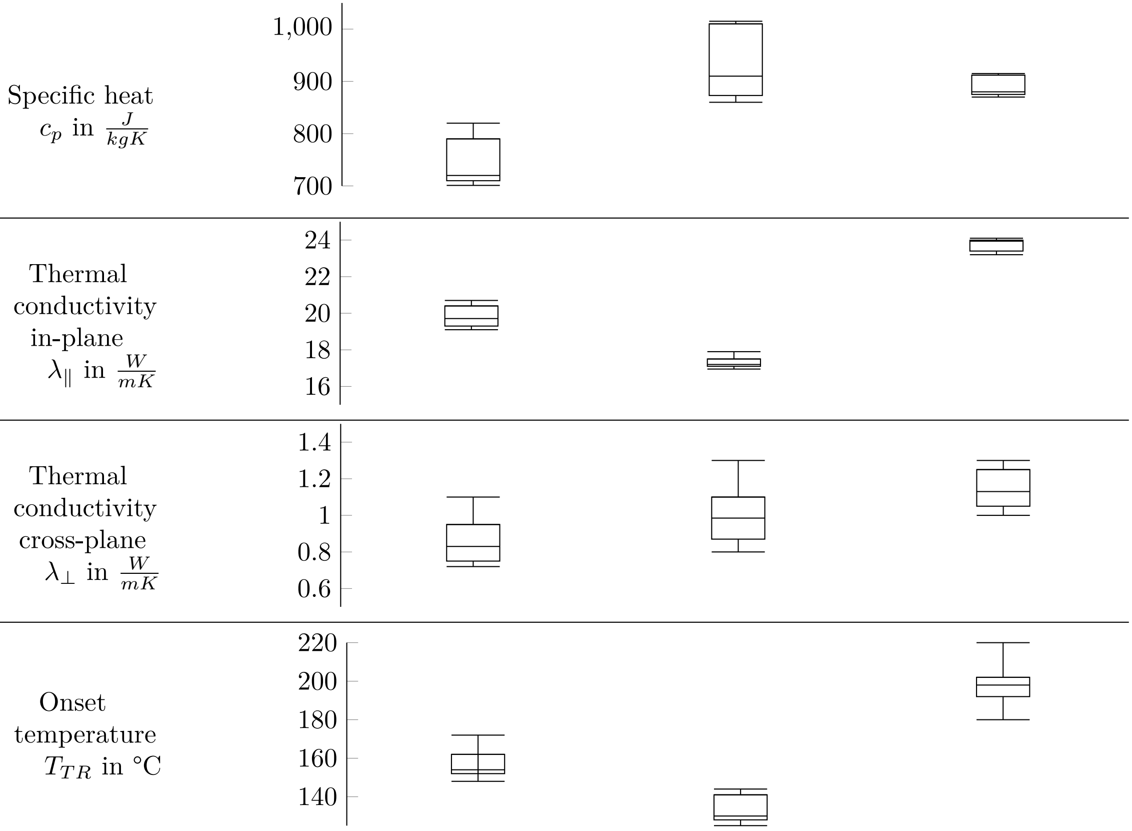

4 Battery thermal management: state of the art

Driven by the necessity of thermal management for battery packs highlighted in the previous chapters, several competing BTMS technologies have been developed since the commercialization of LIBs. To date, air, liquid and refrigerant based systems are defining state of the art and are present in most of the real life applications [56], [123]. The choice between those alternatives is mainly made depending on power requirements and space or weight constraints. Principal characteristics of the individual systems are briefly described in the following sections. System efficiency is quantified by a cooling performance coefficient η_{cool} which is calculated from accumulated values of electrical cooling power required and the total heat flux from the battery according to equation 4.1. Furthermore, a system efficiency value η_{sys}, defined as quotient of remaining usable energy and total energy drawn is introduced according to equation 4.2. In order to highlight the general differences, identical cells with a constant heat release $\dot{Q}_{Batt}$ are utilized for sample calculations. Their characteristics are given in table 4.1. At the end of each of the following sections, basic calculations allow an estimation of both efficiency values and additional parameters as minimum required coolant temperature. As within the whole thesis, in the following, the focus lies on systems for automotive and stationary applications.

$$\eta_{cool} = \frac{\int \dot{Q}_{Batt} dt}{\int P_{cool,el} dt} \tag{4.1}$$

$$\eta_{sys} = \frac{\int (P_{el} - P_{cool,el}) dt}{\int P_{el} dt} \tag{4.2}$$

Table 4.1: Sample data for 60 Ah NMC pouch cell used for exemplary comparative calculations

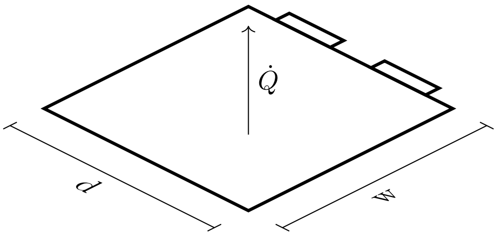

Parameter	Variable	Value	Unit
Cell width	w	0.3	m
Cell depth	d	0.25	m
Target cell surface temperature	T_{cell}	25	$°C$
Av. heat generation per cell (measured)	$\dot{Q}_{Batt}$	18	W
Number of cells in pack	n_{cells}	216	-

4.1 Air based systems

Air based systems utilize conditioned ambient air as medium to temper the battery cells. While very basic systems solely rely on air from outside, more complex systems profit by preconditioned air taken from the vehicle cabin or feature additional A/C units especially for the battery compartment. In addition to that, there are also systems combining all three approaches, switching between them based on ambient temperature and battery load [33]. All air based systems strongly benefit from the fact that there is no need for insulation between the air and the battery, resulting in relatively simple and highly adaptable setups. The lack of liquid components also facilitates battery swapping, minimizes maintenance efforts and allows lighter components [57]. However, there are also several inevitable drawbacks of using air as a medium. The very limited specific heat capacity of air necessitates high mass fluxes, resulting in spacious ducts, manifolds and fans. For the battery pack of a Toyota Prius shown in figure 4.1, cooling components require the same space as the battery modules themselves.

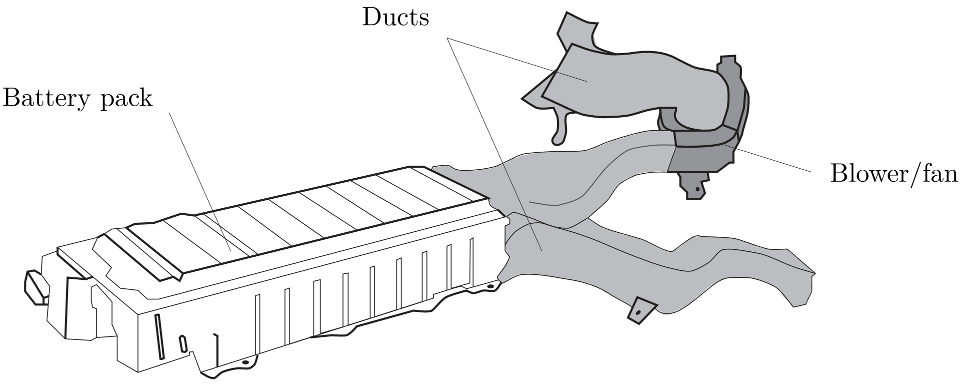

Figure 4.1: Main components of a Toyota Prius battery pack cooling system

As a consequence of its small heat capacity, air tends to show temperature spreads between inlet and outlet. In order to account for that, special attention is required when designing the coolant channel geometry. In higher load applications only a limited number of cells can be cooled in series, before spread between first and last cell gets critical due to the warm up of the downstream air. The issue can be addressed by higher flow velocity w_{air}, which then, however, also results in higher pressure losses and an decreased energy efficiency [94]. In order to prevent debris from entering the battery pack, additional filters are obligatory, adding to the pressure drop. The air flow through all those components can cause significant background noise, which is perceived as disturbing particularly in automotive applications. When used in vehicles, another safety-relevant issue arises. Due to the partial use of cabin air, for most system layouts a direct connection between passenger compartment and battery pack exists. In the event of gassing from the cells, major safety concerns arise and have to be handled, e.g. by additional emergency flaps or vents.

$$R_{th,conv} = \frac{1}{\alpha \cdot A_{air}} = \frac{l}{Nu \cdot \lambda_{air} \cdot A_{air}} \qquad (4.3)$$

Pure air cooling is present for some automotive applications, but driven by the trend of higher performance load cycles and fast charging gradually replaced by other concepts. However, for moderate power automotive and most stationary and portable applications it remains the prevalent BTMS.

Dimensioning

For air cooled systems, the decisive thermal resistance arises from the convective heat transfer α between cells and cooling air, which can be estimated with the help of Reynolds (Re), Prandtl (Pr) and Nusselt (Nu) numbers. Depending on the geometrical setup, common empirical formulas for overflown plates or cylinders can be used. As given in equation 4.3, besides the fluid flow parameters, only thermal conductivity of the air λ_{air} and transfer area A_{air}, equally to the overflown battery surface area, are of significance [5].

Nusselt, Reynolds and Prandtl numbers are depending on the geometric setup and the air's properties only. Temperature profile and cooling efficiency hence can be optimized by adjusting those parameters [133]. For the given case, those can be calculated from fluid velocity w_{air}, fluid thermal conductivity λ_{air}, fluid specific heat $c_{p,air}$ and kinematic viscosity ν_{air} according to equations 4.4 - 4.6. Depending on the Reynolds number, correlations for laminar or turbulent flow have to be applied. As convective heat transfer highly benefits from turbulence effects, for most applications fluid velocity should be chosen accordingly to ensure a turbulent flow pattern [152].

$$Nu = \frac{0.037 \cdot Re^{0.8} \cdot Pr}{1 + 2.443 \cdot Re^{-0.1} \cdot \left(Pr^{2/3} - 1\right)} \qquad (4.4)$$

$$Pr = \frac{\nu_{air}}{\lambda_{air}} \qquad (4.5)$$

$$Re = \frac{w_{air} \cdot l}{\nu_{air}} \qquad (4.6)$$

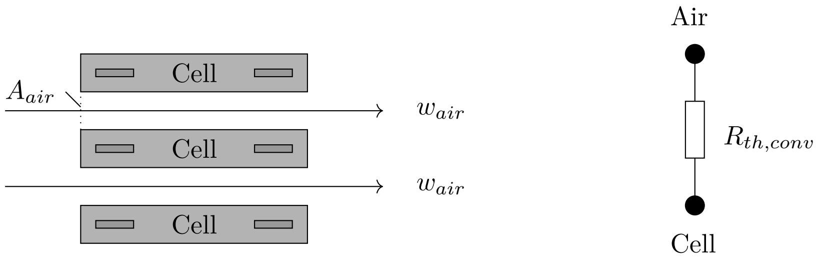

Figure 4.2: Layout of air cooled system - top view

With known R_{th}, the required temperature of the cooling air T_{air} can be calculated according to equation 4.7 as a function of the desired cell temperature. The coolant mass flux results from the velocity v_{air}, the air's density ρ_{air} and the cooling channel cross section A_{air} according to equation 4.8. As an open system is assumed, only ambient air is used, so that the difference between T_{amb} and the desired cooling air temperature T_{air} has major impact on the electrical cooling power required (equation 4.9). Due to the fact that an ambient temperature is assumed, which lies above the desired battery temperature, also parasitic heat fluxes $\dot{Q}_p$ into the system have to be considered. The corresponding amount of heat scales with temperature spread and battery pack insulation, but is assumed to be constant in the following, for simplification. The Coefficient of Performance (COP) of the Heating Ventilation Airconditioning (HVAC) system ϵ and the electrical power for the fans and blowers P_{fans} further affect system efficiency. With the assumed typical figures given in table 4.2, the values for cooling and overall efficiency can be calculated according to equation 4.1 to be 72.2 % and 92.5 % respectively.

$$T_{air} = T_{cell} - \dot{Q} \cdot R_{th,conv} \tag{4.7}$$

$$\dot{m}_{air} = w_{air} \cdot A_{air} \cdot \rho_{air} \tag{4.8}$$

$$P_{cool,el,air} = \frac{\dot{m} \cdot c_p \cdot (T_{amb} - T_{air}) + \dot{Q}_p}{\epsilon} + P_{fans} \tag{4.9}$$

$$\eta cool = \frac{\dot{Q}}{P_{cool,el,air}} \tag{4.10}$$

Table 4.2: Assumptions made for air based cooling system

Parameter	**Variable**	**Value**	**Unit**
Air channel cross section	A_{air}	10	cm^2
Air velocity	w_{air}	7.0	$\frac{m}{s}$
Air density	ρ_{air}	1.184	$\frac{kg}{m^3}$
Air kinematic viscosity	ν	$1.58 \cdot 10^{-5}$	$\frac{m^2}{s}$
Air th. conductivity	λ_{air}	0.0262	$\frac{W}{mK}$
Prandtl number	Pr	0.72	-
Nusselt number	Nu	391.6	-
Reynolds number	Re	$1.33 \cdot 10^5$	-
Total thermal resistance	R_{th}	0.39	$\frac{K}{W}$
Ambient air temperature	T_{amb}	30.0	°C
Required air temperature at A/C outlet	T_{air}	11.0	°C
Coefficient of performance [1]	ϵ	1.8	-
Parasitic heat flux [2]	$\dot{Q}_p$	250	W
Power for fans [3]	P_{fan}	200	W
Cooling efficiency	$\boldsymbol{\eta_{cool,air}}$	**72.2 %**	**-**
System efficiency	$\boldsymbol{\eta_{sys,air}}$	**92.5 %**	**-**

---

[1] Resulting from temperature spread between required air inlet temperature and ambient temperature according to compressor characteristics

[2] Based on an estimated pack surface of $2.4m^2$, a constant temperature difference between pack and ambient of $\Delta T = 5°C$ and a heat transfer coefficient $\alpha = 20.9 \frac{W}{m^2K}$

[3] Estimation based on reference automotive battery packs

4.2 Liquid based systems

A very common approach for cooling medium to high performance battery packs is the integration of liquid cold plates into the system. These components are put in thermal contact with individual cells or modules and driven by a liquid coolant. Heat is hence convectively transported from the cells towards a heat sink located at a remote position. While basic systems only utilize a radiator as heat sink, more advanced systems dissipate the heat via an evaporator into a refrigerant circuit. Especially for the use in automotive applications, also a combination of both layouts is common, dynamically switching the heat sink depending on ambient temperatures and current loads. An exemplaric dual circuit setup and its main components are presented in figure 4.3. Though adding several additional components, as piping, pumps and heat exchangers, liquid cooled systems still feature a compact design but normally add more weight than their air based counterparts. In addtion to that, several challenges arise from adding a liquid coolant in direct proximity to high voltage components. During all operation and crash scenarios, a safe insulation between coolant and live connectors has to be guaranteed [56], [153], [64]. During production, operation and maintenance leakage tests and continuous leakage sensing are mandatory.

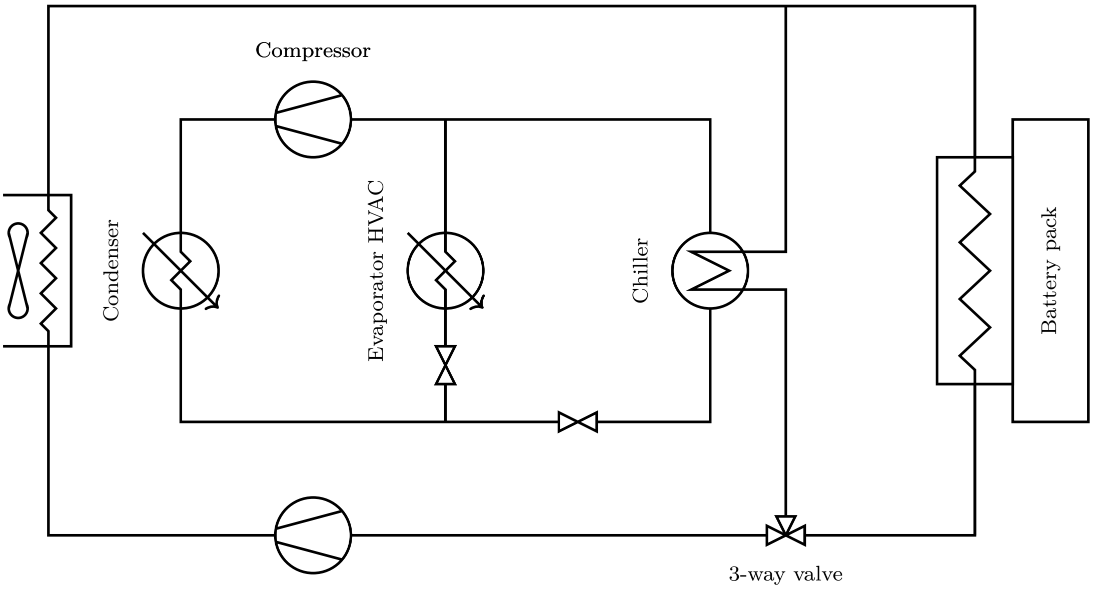

Figure 4.3: Dual circuit liquid cooling concept

According to market data and sales figures, the liquid cooled concept is the predominant concept for BEV and PHEV vehicles sold to date [30]. For stationary applications it is only used for few high power load profiles.

Dimensioning

For liquid cooled systems cooling power is mainly determined by conductive ($R_{th,cond}$) and convective thermal resistance ($R_{th,conv}$) between cell surface and coolant. The conductive part is dependent on the average length of the heat flow path between cell and coolant, and the material in between. The convective share is a function of channel diameter and fluid properties as viscosity, heat capacity and flow velocity. Total resistance can be modeled as a serial connection of the two indiviudal components (figure 4.4) and is assumed according to equation 4.11 in the following. The Nusselt number, describing the convective heat transfer coefficient α in most cases can be estimated using analogies for cylindrical pipes as they are given in equation 4.12 [12].

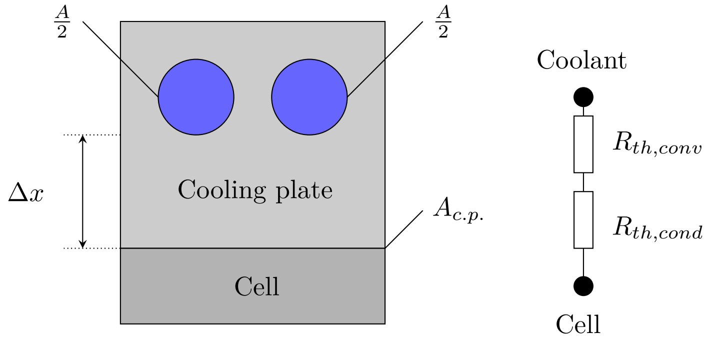

Figure 4.4: Cross section of liquid based cooling, heat flow path and schematic thermal model

$$R_{th} = R_{th,cond} + R_{th,conv} = \frac{\Delta x}{\lambda_{c.p.} \cdot A_{c.p.}} + \frac{1}{\alpha \cdot A} = \frac{\Delta x}{\lambda_{c.p.} \cdot A_{c.p.}} + \frac{0.5 \cdot d_{channel}}{Nu \cdot \lambda \cdot A} \tag{4.11}$$

$$Nu = 0.02 \cdot Re^{0.80} \cdot Pr^{0.43} \tag{4.12}$$

Prandtl and Reynolds numbers are calculated similarly to the air cooled case, but now based on the channel diameter $d_{channel}$ as characteristic length.

$$Pr = \frac{\nu_{liq}}{\lambda_{liq}} \tag{4.13}$$

$$Re = \frac{v_{liq} \cdot 0.5 \cdot d_{channel}}{\nu_{liq}} \tag{4.14}$$

The required temperature of the coolant medium again arises from R_{th} and $\dot{Q}$ as shown in equation 4.15.

$$T_{liq} = T_{cell} - \dot{Q} \cdot R_{th} \qquad (4.15)$$

$$\dot{m} = w \cdot A_{channel} \cdot \rho_{liq} \qquad (4.16)$$

Unlike the air cooled system, the liquid coolant is circulated inside a closed loop, so that only the actual heat release from the battery and parasitical heat flux from the ambient have to be considered. The overall COP is defined by the COP of the condenser and the chiller. As the coolant needs to be actively circulated, a certain amount of electrical power P_{pump} is also allotted to the circulating pumps. The resulting cooling efficiency (>100 %) significantly outnumbers the air cooled system and hence also results in a superior system efficiency, that lies 4 % above the air cooled variant.

$$P_{cool,el,liq} = \frac{\dot{Q} + P_{parasitic}}{\epsilon} + P_{pump} \qquad (4.17)$$

$$\eta cool = \frac{\dot{Q}}{P_{cool,el,liq}} \qquad (4.18)$$

Table 4.3: Assumptions made for liquid based cooling system

Parameter	**Variable**	**Value**	**Unit**
Coolant channel cross section	$A_{channel}$	19.6	mm^2
Coolant velocity [1]	w_{liq}	2.0	$\frac{m}{s}$
Coolant density	ρ_{liq}	997	$\frac{kg}{m^3}$
Coolant kinetic viscosity	ν_{liq}	$8.93 \cdot 10^{-7}$	$\frac{m^2}{s}$
Coolant th. conductivity	λ_{liq}	0.597	$\frac{W}{mK}$
Total thermal resistance	R_{th}	0.07	$\frac{K}{W}$
Required coolant temperature	T_{liq}	11.3	°C
Coefficient of performance [2]	ϵ	1.9	-
Parasitic heat input [3]	$P_{parasitic}$	500	W
Auxiliary pump power [4]	P_{pump}	200	W
Cooling efficiency	$\boldsymbol{\eta_{cool,liq}}$	**170.7 %**	**-**
System efficiency	$\boldsymbol{\eta_{sys,liq}}$	**96.8 %**	**-**

---

[1] Based on the actual BTMS dimensioning of the EVA vehicle (see section 8.1

[2] Resulting from temperature spread between required coolant temperature and ambient temperature according to compressor characteristics

[3] Based on an estimated pack surface of $2.4m^2$, a constant temperature difference between pack and ambient of $\Delta T = 10°C$ and a heat transfer coefficient $\alpha = 20.9\frac{W}{m^2K}$

[4] Estimation based on technical data of pumps used for automotive battery pack cooling e.g. Pierburg CWA 200

4.3 Refrigerant based systems

Instead of coupling air- or liquid cooling components to a refrigerant circuit, batteries can also be cooled directly by evaporators. This concept commes along with a series of advantages. Superseding interim steps as HVACs or chillers, transfer losses can be reduced. As this approach also significantly reduces the number of actively driven components, the concept allows to save weight and can be designed more compact than the other systems presented so far [88]. The well defined evaporation temperature enables a more homogeneous temperature level that can be achieved throughout the whole cooling surface and results in a very uniform distribution. As most of the refrigerant circuit's components are also required for the purpose of cabin thermal management, the need for additional piping is reduced to a minimum. Figure 4.5 depicts all relevant components and the direct link to the cabin evaporator.

The fundamental principle of operation allows those systems to be run in heat pump mode and hence heating up the battery without additional components. As an alternative, also electric heating foils can be placed inside or beneath the battery pack.

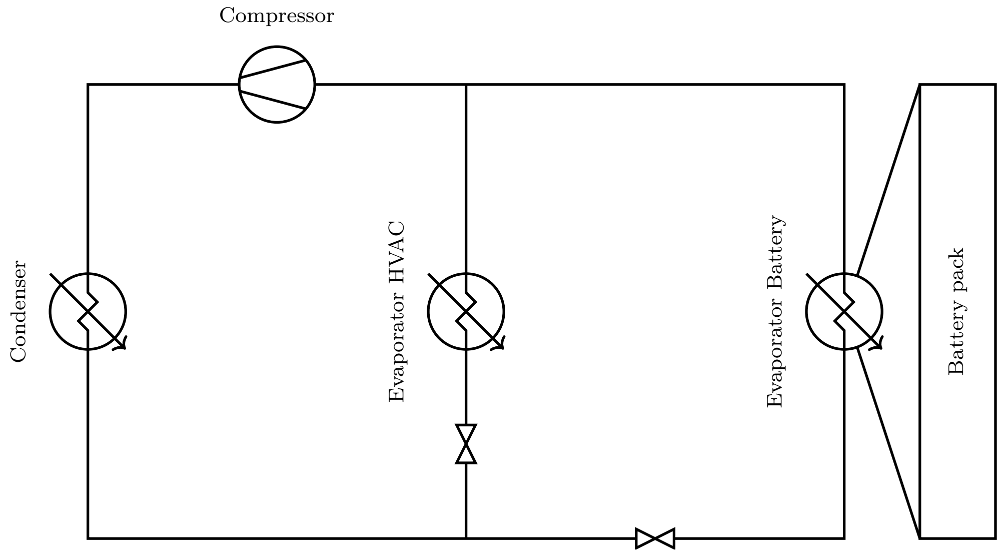

Figure 4.5: Refrigerant based cooling concept

As cabin and battery climatisation are directly linked to the same refrigerant cycle, an increase in battery cooling demand reduces the available cooling power for the passenger department. Studies show that even for smaller PHEVs, battery cooling demand adds up to 11 % of the total refrigerant cycle power [85]. Although the maximum overall system efficiency can benefit from the direct coupling with the cabin cooling and the arising synergies, in certain cases this link can be a disadvantage as well. This is especially the case, when the cabin does not require cooling at all but the whole circuit has to be kept active due to high battery loads.

Dimensioning

For direct refrigerator systems evaporator plates are directly mounted on the cell surface, hence thermal resistance between cell and refrigerant is dominated by the thickness and the material properties of the evaporator's wall only. The according schematic heat flux path is shown in figure 4.6. Under the assumed operation conditions, the refrigerated system features the highest efficiency of the three presented concepts.

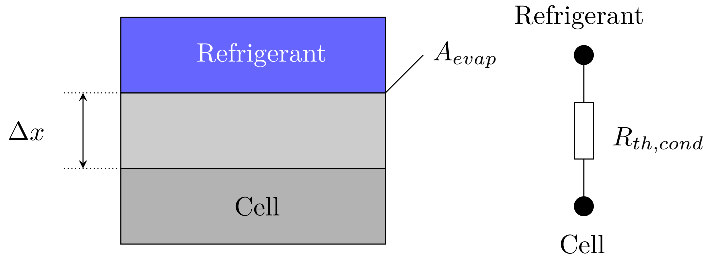

Figure 4.6: Cross section of refrigerant based cooling, heat flow path and schematic thermal model

$$R_{th} = R_{th,cond} = \frac{\Delta x}{\lambda_{evap.} \cdot A_{evap}} \quad (4.19) \qquad T_{ref} = T_{cell} - \dot{Q} \cdot R_{th} \quad (4.20)$$

$$P_{cool,el,ref} = \frac{\dot{Q} + P_{parasitic}}{\epsilon_{ref}} \quad (4.21) \qquad \eta cool, ref = \frac{\dot{Q}}{P_{cool,el,ref}} \quad (4.22)$$

Table 4.4: Assumptions made for refrigerant based cooling system

Parameter	**Variable**	**Value**	**Unit**
Total thermal resistance	R_{th}	0.036	$\frac{W}{K}$
Required refrigerant temperature	T_{ref}	16.7	°C
Coefficient of performance [1]	ϵ	2.3	-
Parasitic heat input [2]	$P_{parasitic}$	500	W
Cooling efficiency	$\boldsymbol{\eta_{cool,ref}}$	**216.1 %**	**-**
System efficiency	$\boldsymbol{\eta_{sys,ref}}$	**97.5 %**	**-**

---

[1] Resulting from temperature spread between required refrigerant temperature and ambient temperature according to compressor characteristics

[2] Based on an estimated pack surface of $2.4m^2$, a constant temperature difference between pack and ambient of $\Delta T = 10°C$ and a heat transfer coefficient $\alpha = 20.9\frac{W}{m^2K}$

4.4 Comparison of common concepts

Most of the battery packs used in stationary or automotive applications rely on one of the three thermal management systems described in the precedent sections. While each of the systems has been known in other fields for years and has further been refined and adapted to the use in battery systems, they all still feature some disadvantages. A summary of the individual strengths and weaknesses is given in table 4.5. The overview also considers issues of integration and interference with other components, as well as economic topics.

Table 4.5: Benchmark of common Battery Thermal Management Concepts

	System technology		
Criteria	**Air cooled**	**Liquid cooled**	**Refrigerated**
η_{cool}	**72.2 %**	**170.7 %**	**216.1 %**
η_{sys}	**92.5 %**	**96.8 %**	**97.5 %**
System complexity	◕	◑	◔
Ease of use	◕	◔	◑
System weight	◕	◔	◑
System volume	◔	◑	◕
Cooling power	◔	◑	●
Cooling uniformity	◔	◑	●
Integration of heating	●	●	◔
Interference with other components	◔	◑	◔
Initial system cost	◕	◑	◔
Maintenance effort	◕	◔	◑

Requirements ◔ not met ◑ partly met ◕ mostly met ● fully met

Shortcomings of all existing active concepts

All presented thermal management concepts utilize active components in order to cool or heat the battery directly or via a coolant medium. Besides the already mentioned drawbacks in terms of efficiency, costliness and space requirements, those active systems come along with additional shortcomings. Fans, pumps and compressors all create noise and vibrations, that can be perceived disturbing in quiet surroundings. Furthermore, all systems rely on the interplay of several components, that all for themselves face wearing and require regular maintenance. In case external power supply is cut, none of the active systems provides any cooling power. All those shortcomings encourage the integration of additional passive measures in order to entirely cool the battery or at least support existing active solutions by storing thermal energy.

4.5 Thermal energy storage

Instead of dissipating thermal energy to the ambient, it can be advantageous to temporarily store the heat or cold passively. Based on load scenarios and ambient conditions, the stored energy can then still be dissipated at a later point of time, or even be profitably used for another application. Three different fundamental approaches of storing thermal energy can be differentiated. The principle mechanisms and their eligibility for battery application are discussed in the following.

Thermochemical storage

Reversible chemical reactions and sorption processes can be used to store and retrieve heat. During an endothermic reaction a thermochemical material is dissociated into two or more reactants, while absorbing thermal energy [150]. The amount of energy required for this reaction equals the enthalpy of formation ΔH and also defines the amount of thermal energy that can be stored during the process. After the conversion, the individual reactants can be stored separately. In order to retrieve the stored thermal energy, both reactants are brought together again, exothermally combining into the original thermochemical material [91].

The total amount of energy stored can be calculated from the standard enthalpy of the chemical reaction according to the following equation 4.24.

$$\text{Educts} \Longleftrightarrow \text{Products} + \Delta H \tag{4.23}$$

$$Q = H_{\text{Products}} - H_{\text{Educts}} \tag{4.24}$$

As the individual reactants can be stored separately at ambient temperature, Thermochemical Storage (TCS) allows long storage periods at relatively low degradation and without the need for actively keeping the individual components at certain temperatures. The method also offers a comparatively high energy density of up to $410\frac{kWh}{m^3}$ [122]. However, the complexity of handling and especially separating/combining the liquid components prevents a broader use for virtually all battery applications.

Sensible heat

Storing sensible heat inside a material results in an increase of its enthalpy and a resulting sensible change in temperature. The effect is omnipresent and of immanent importance, due to the high weight of battery systems and their high heat capacity (see section 3). Within a defined state of matter, for a known temperature rise, the amount of heat stored can be calculated from the sample mass and temperature-dependent heat capacity according to equation 4.25 [40].

$$Q_{1\rightarrow 2} = m \int_{T_1}^{T_2} c_p\left(T\right) dT \qquad (4.25)$$

The given correlation is only valid for temperature ranges, where the whole sample is present in a defined and homogeneous solid, liquid or gaseous state. Furthermore a certain offset toward the phase change temperature regions should be kept. When approaching phase change temperatures, additional correlations for latent heat have to be taken into account [37]. Sensible heat storage is always present by nature, and hence also affects the dynamics of all BTMS. Depending on the battery mass, the thermal inertia due to sensible heat storage can support the mitigation of internal or external thermal peaks.

Latent heat

During the melting and vaporization process of a material sample its properties discountinously change and large amounts of heat energy can be stored at nearly constant temperatures. In the opposite direction, the same amount of heat is recovered during condensation or solidification of the corresponding material [18]. As the amount of heat stored during phase transition can not be sensed by a temperature change, the according energy is referred to as latent heat. Technical latent heat storage is already known for centuries (e.g. ice blocks used for cooling [32]) and features several advantages over the other thermal storage concepts:

- Heat is stored at a predefined temperature level or temperature range.
- Specific storage capacity is significantly higher than for sensible heat.
- The storage process is virtually infinitely repeatable.
- Unlike the TCS, no material transport is required.

The amount of heat stored/released during the phase change is only dependent on mass m and the specific latent heat L of the sample as presented in equation 4.26.

$$Q = mL \qquad (4.26)$$

Values for L typically differ for fusion and vaporization and are solely dependent on the material. Hence a certain group of materials being best suitable for storage of latent heat in different applications has evolved, widely being known as Phase Change Material (PCM). Their properties and the advantages of latent heat storage make them promising candidates for integration into battery applications.

5 Phase change material (PCM)

Using a material's phase transition in order to temporarily store heat and cold is already well established and present in numerous industrial applications as building climatisation or storage of solar energy [87]. Accordingly, there is a wide selection of known PCMs with strongly varying properties, especially in terms of melting temperature and storage capacity. Based on their molecular structure common phase change materials are divided into two categories that highly differ in their thermophysical characteristics [103].

5.1 Classification and properties

Inorganic

Inorganic materials used for latent heat storage applications are mainly salts, salt hydrates and metals. Due to their high phase change enthalpy, all of them are able to store a significant amount of energy. However, especially for salts and metals, phase change is located at high temperatures, inhibiting a broad technical application. Phase segregation and phase separation, as well as corrosion issues, further impede their utilization. Typically, salts are used for large scale industrial applications e.g. as energy storage for solar thermal power plants, but no battery applications are known [101].

Organic

The broad group of PCMs based on carbon and hydrogen structures is referred to as organic materials, with fatty acids, glycols and paraffins being the main representatives. All three undergo their phase change at low to medium temperatures in the range of 15 °C to 130 °C and show only limited subcooling and few irreversible effects [134]. Their heat of fusion typically increases with the length of the carbon chain, but still falls short of most comparable inorganic materials. Furthermore, fatty acids as e.g. capric acid, lauric acid, palmatic acid, or their eutectic mixtures bring along oxidation problems, when in contact with metallic components.

Paraffins, however, being non-corrosive, non-toxic and recyclable are easy to handle and present in several latent heat storage applications. Typical fields of use include building technology, but also first automotive applications e.g. for cabin heating [113].

Figure 5.1 presents a first overview over the most common material categories and their respective melting temperature ranges, as well as their specific latent heat storage capacity.

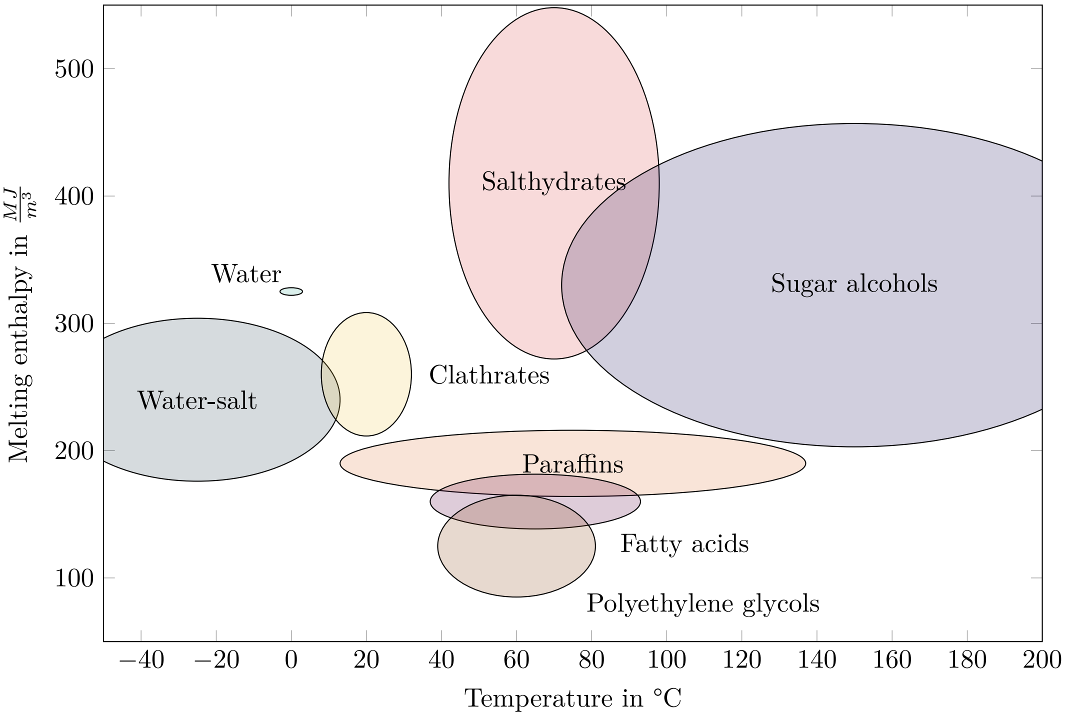

Figure 5.1: Overview on PCM types, temperature ranges and storage capacities [103]

By nature, those two properties are the most important characteristics for technical applications. However, there are additional properties that are very specific for those kinds of material and determine their proper selection. All of them are briefly presented in the following subsections.

Melting temperature and range

As for most technical applications, and especially battery thermal management, the desired operating temperature range is predefined. Hence, the first preselection of suitable PCM should be based on the melting temperature, that has to lie within the application's limits. Due to the variety of PCM, a wide temperature range can be covered. While imidazolium based ionic liquids melt between -100 °C and -20 °C, melting temperatures of inorganic salts can easily reach 800 °C and more [157], [124]. Materials most relevant for commercial application however feature a more moderate melting temperature between 0 °C and 100 °C [151]. The melting point of selected materials of this group can be read from figure 5.2.

Mainly three melting point regions are of interest in battery applications. For normal operation melting points aligned with the cell's recommended temperature (see also table 2.2) help to maximize the time the system remains near the respective range. When only used for peak mitigation, a slightly higher melting temperature should be considered, lying in a range that is only reached during the peak loads. In case the PCM is foreseen to add safety to the system during overload or thermal runaway, even higher melting temperatures are preferable. This way, it can be made sure that the material is in solid state and ready to dissipate power at any time. By combining two or more materials, phase change temperature ranges can also be covered, or materials with two distinctive storage levels can be created.

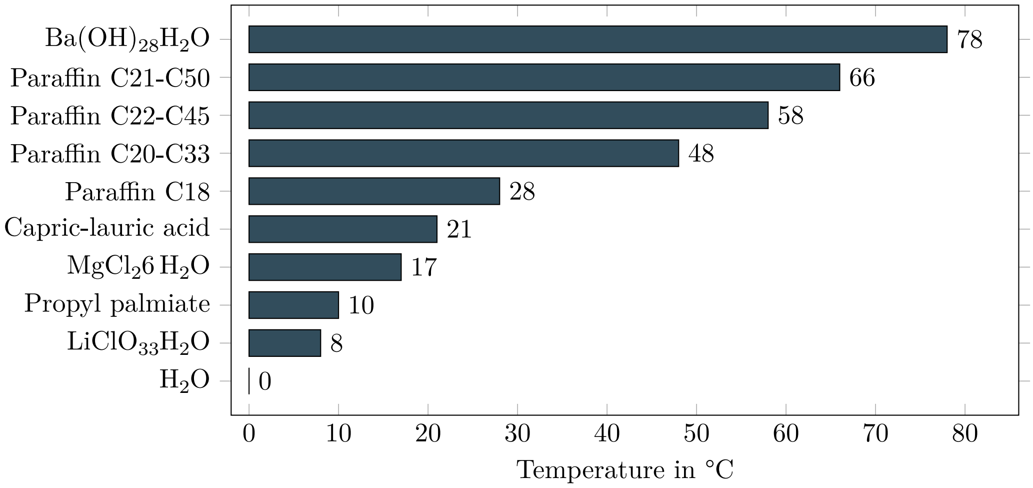

Figure 5.2: Melting temperatures of selected PCMs in the range of 0 °C to 100 °C [17], [86]

Latent heat storage capacity

As wide as the range of melting temperatures, is the range of storage density for the material. For battery applications, the selected material should preferably feature high specific latent energy density. Typical values for gravimetric latent energy range from 143 $\frac{kJ}{kg}$ to 333 $\frac{kJ}{kg}$, with selected values being given in figure 5.3.

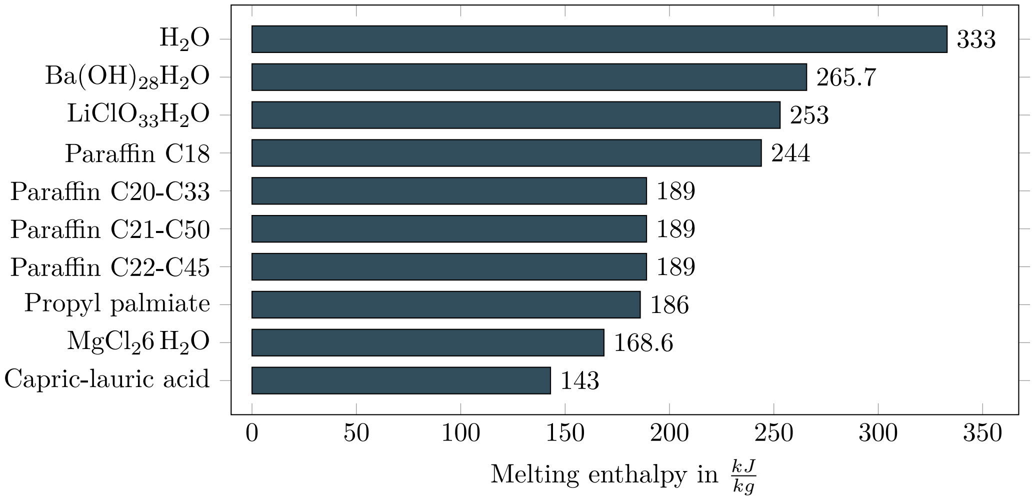

Figure 5.3: Gravimetric latent heat of fusion of selected PCMs [147], [84]

Due to the fact that materials highly differ in density, for some applications, especially with limited space, instead of gravimetric, the volumetric specific heat can be the decisive design criteria. Sample values can be read from figure 5.4.

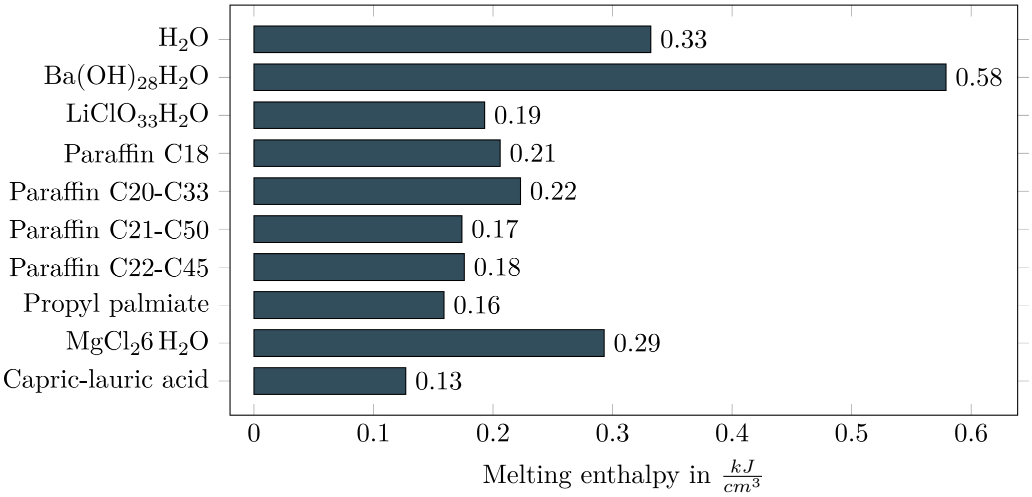

Figure 5.4: Volumetric latent heat of selected PCMs [141], [1], [61], [109]

Thermal conductivity

In general, for nearly all applications based on phase transition, a high thermal conductivity is favorable as it increases storage speed. However, most common PCMs feature very limited thermal conductivity, which, additionally can highly differ between solid and liquid phase. Values range from as low as $0.1088\frac{W}{mK}$ ($CaCl_2$) to moderate levels around $1.225\frac{W}{mK}$ for some salthydrates. Figure 5.5 summarizes thermal conductivity data for selected PCMs in solid/liquid state, available from literature. As battery applications demand a more dynamic behavior, advanced material composites, described in detail in section 5.3, are introduced in order to overcome the limitations in terms of rapid heat storage and release.

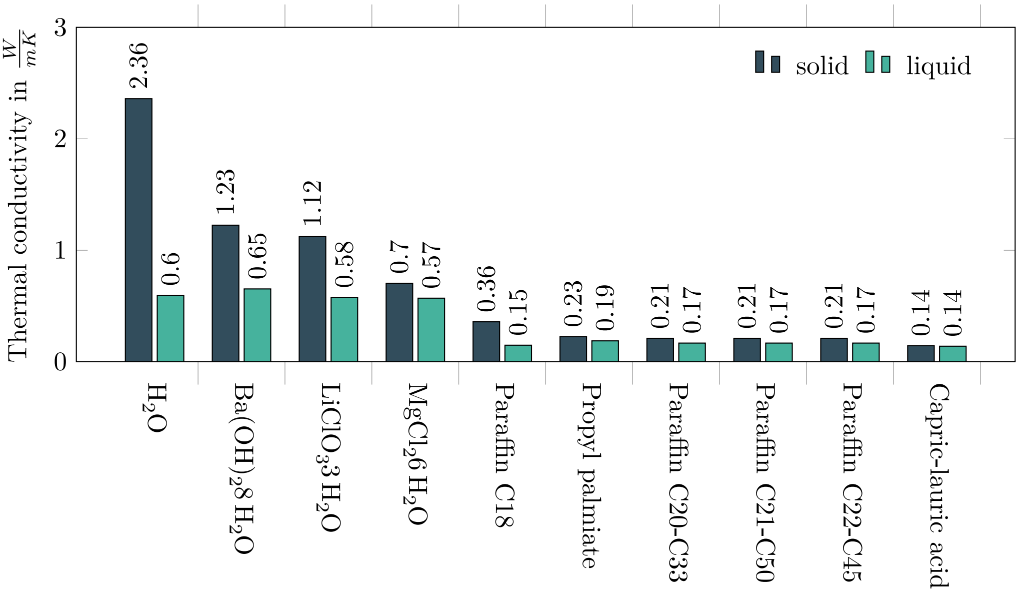

Figure 5.5: Thermal conductivity of selected PCMs in solid/liquid state

Subcooling

A big portion of common PCMs does not start solidifying directly when reaching the nominal phase change temperature, but can be cooled well below this temperature level before crystallization sets in [63]. As the effect, known as subcooling, widens the required temperature spread between hot and cold areas of cyclic operation, it is highly undesirable for most technical applications.

The effect of subcooling is driven by an energy balance at the small fraction of PCM that solidifies first, in the following referred to as nucleus [50]. During solidification the system has to release heat. However, surface energy is required to extend the surface around the growing nucleus. Surface energy is proportional to the nucleus' surface, while crystallization energy scales with the nucleus' volume. Hence, especially for small nuclei and low sub-cooling, it can be energetically advantageous for the material not to go into crystallization [117].

As impurities can also serve as starting point for crystallization, pure materials, in general, show deeper subcooling than composite or polluted liquids [49].

Figure 5.6 depicts a typical temperature-enthalpy correlation for a paraffin based PCM, experimentally recorded by Differential Scanning Calorimetry (DSC). With the red line reflecting the melting and the blue line reflecting the solidification process, one can clearly see the significant temperature hysteresis.

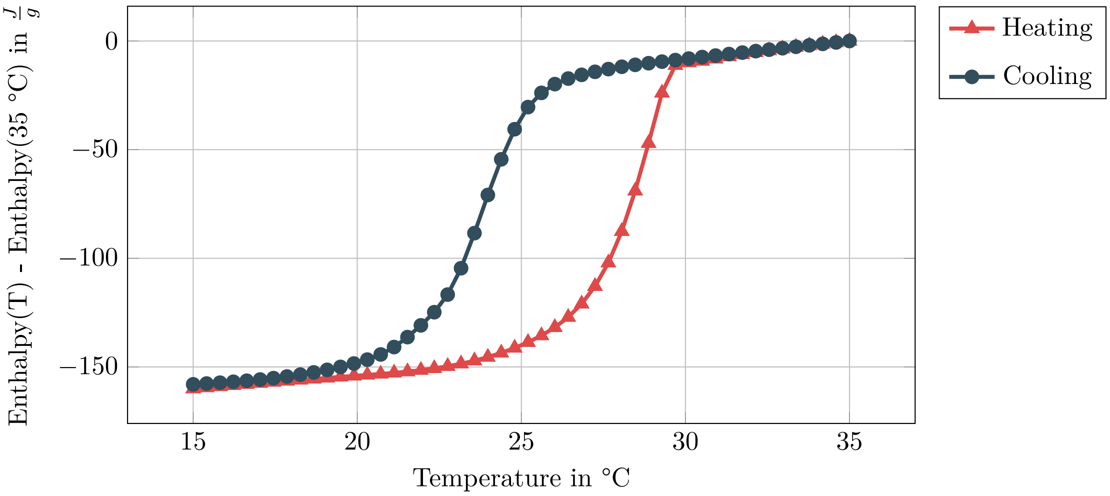

Figure 5.6: Melting/solidification of a paraffin based PCM with $T_{melt} = 28°C$ tracked by DSC

Toxicity, Flammability, economic considerations

Besides the thermophyiscal aspects covered in the precedent sections, additional criteria have to be considered, especially if the PCM is used in consumer applications. As the material mostly has to be integrated into closed volumes, low volume changes during phase transition are necessary or desirable. In order to facilitate handling during assembly, operation and maintenance, toxic, flammable and explosive materials are to be avoided wherever possible.

Acceptance for further integration of PCM is also highly linked to economic aspects. Figure 5.7 compares typical PCMs in terms of their cost per kg storage capacity. Prices are given for preprocessed raw material, ready for integration in thermal management applications.

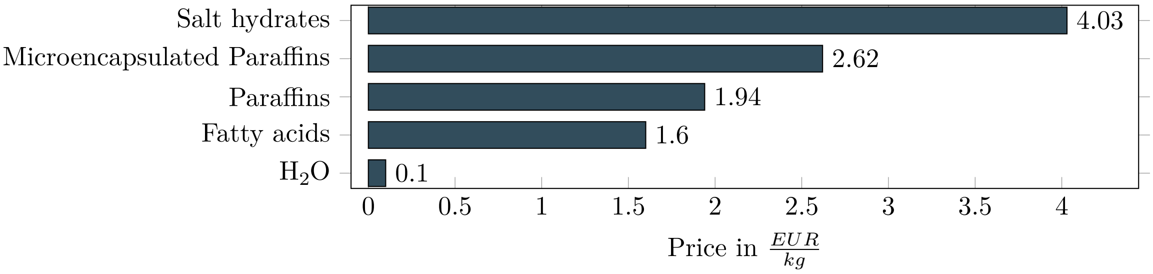

Figure 5.7: Cost of selected PCMs [82]

5.2 Characterization

As materials should be customized for the specific application and the variety of pure or composite materials is unconfined, a reliable characterization prior to integration is essential. One of the very well established methods for determining a material's capability of storing sensible and latent heat is DSC. It is based on tracking the differences in how the sample probe and a known reference probe respond to an externally imposed temperature profile [60]. In dynamic mode, constant heating and cooling rates are applied, and temperature difference between sample and reference is logged. With the help of the known material, temperature dependent specific heat of the sample and its overall storage capacity can be calculated [7].

The accuracy of DSC measurements highly depends on the applied rate of temperature change and the size of the probes. Especially larger heating/cooling rates applied to materials with low thermal conductivity or heterogenity can result in significant deviations [38].

T-history method

Particularly for larger sample sizes, as they are required for inhomogeneous materials, another measurement technique is viable and widely used. First proposed by Zhang et al. in 1999, the T-history method can be utilized to identify phase change temperature and melting enthalpy. Since its initial presentation, the method has highly evolved and is now established as a standard for characterizing phase change materials.

The fundamental principle is based on comparing the transient cooling and warming of both a probe and a well-known reference sample, which both see the identical ambient conditions [130].

Sample and reference are therefore placed inside a perfectly insulated environment with their temperature being tracked at high accuracy. Ambient conditions are controlled by heating and cooling elements and are also recorded. Following an abrupt change in ambient temperature, the resulting heat fluxes to, respectively from, the ambient can be measured.

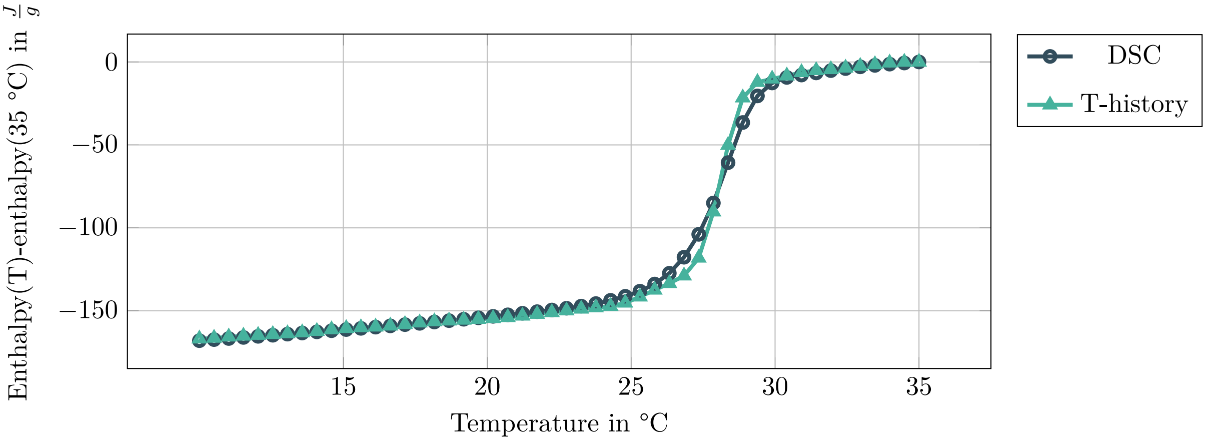

Figure 5.8: Comparison of DSC and T-history measurements

$$\dot{Q}_{sample} = \frac{1}{R_{th}} \cdot (T_{sample} - T_{ambient}) = -C_{sample} \cdot \frac{d}{dt} T_{sample} \tag{5.1}$$

$$\dot{Q}_{reference} = \frac{1}{R_{th}} \cdot (T_{reference} - T_{ambient}) = -C_{reference} \cdot \frac{d}{dt} T_{reference} \tag{5.2}$$

Using samples of identical geometry and exposing them to similar controlled ambient conditions, R_{th} is assumed to be the same for both cases. As for the reference, all material data is known, R_{th} can hence be calculated from equation 5.2. This now allows determination of temperature dependent values for C_{sample} in equation 5.1. Based on the data acquired, temperature-enthalpy correlations can be postulated.

A typical result of a T-history measurement on a composite phase change material is already shown in figure 5.6, highlighting the different profiles for melting and solidifying. Figure 5.8 opposes the results of enthalpy determination using DSC and T-history method on the identical sample.

5.3 Composite functional materials

Especially for dynamic load scenarios, all phase change materials, except for low-melting metals, feature one severe common bottleneck. Their very limited thermal conductivity between as low as 0.14 $\frac{W}{mK}$ and 1.1 $\frac{W}{mK}$ prevents any use in dynamic load cases, where fast heat rejection is required. Those limitations can be overcome by combining the latent heat storing materials with highly thermal conductive materials, forming a sort of composite structure [103]. Based on the application's requirements and boundary conditions, this can be achieved on a macroscopic or microscopic level.

Macroscopic encapsulation

In order to facilitate handling and safely contain the PCM while in liquid phase, many PCMs are enclosed in containers. Those metal or plastic housings make sure the PCM does not get into contact with the environment and is not contaminated with external particles. The inner surface of those containers can also be utilized to improve the heat deposition into and the extraction from the PCM. By adding fins or thin internal walls, the contact surface area can be significantly increased and hence the length of the heat flux path within the low-conducting material is reduced. Especially for larger containers, internal structure can furthermore help to increase structural stability while the PCM is in its liquid phase. The principal concept and its impact is visualized in figure 5.9 comparing the melting process for the identical amount of Paraffin, (a) without and (b) with internal container compartments. For both simulations containers are filled with the identical PCM and exposed to the same thermal ambient conditions.

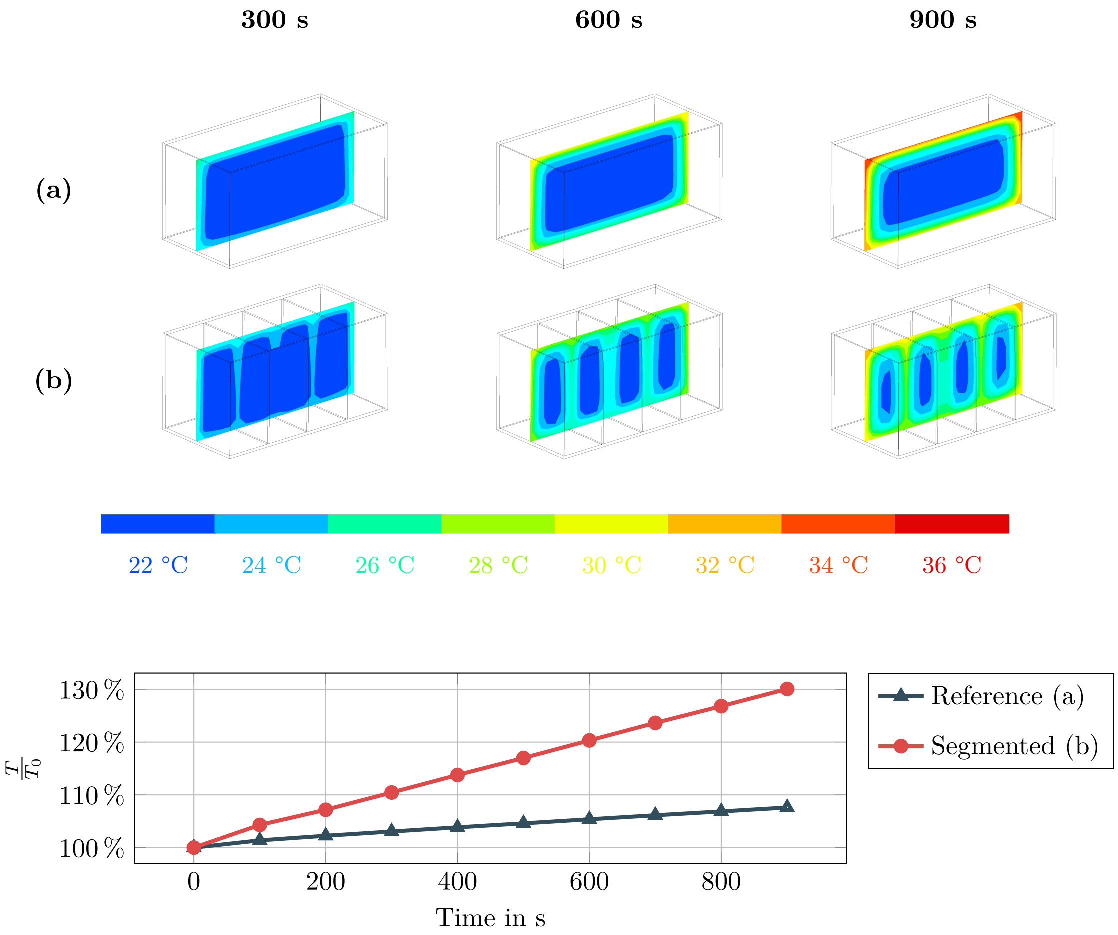

Figure 5.9: Positive impact of internal macro heat spreaders

The simulation results highlight that, due to the smaller individual compartment size in variant (b), heat is stored more rapidly, and is also more evenly distributed than in the reference (a). At the end of the 900 s period under review, the average bulk temperature is more than 20 % higher compared to the base scenario and also the temperature spread within the PCM is reduced by approximately 40 %.

Microscopic encapsulation

Instead of being contained in a macroscopic way, PCM can also be microencapsulated. Therefore, small particles of only a few µm are chemically, physicochemically or physicomechanically coated with a protective solid shell [41].

Depending on the material class, interfacial polymerization, suspension polymerization and spray drying are the most common methods for PCM coating [66]. A frequently used shell material is polymethylmethacrylate, which is suitable and highly compatible with most organic PCMs. Alternative materials used for the capsule are Polyvinyl Chloride (PVC) or polystyrene. Independently from the material-pairings and the production technique, the process results in spherical microencapsulated elements as small as 1 µm. Those microencapsulated PCM parts can then be further processed into suspensions, emulsions or dispersions and also be incorporated into other materials [73]. In technical applications mainly metal foams, as aluminum, are used [159]. The almost perfect spheric shape, the thin coating and the varying diameters depicted in figure 5.10 allow a very dense packing. When stored within spongy carriers, volume fractions of up to 95% of PCM can be achieved [43].

The size and shape of the individual microencapsulated spheres, as well as their integration inside the carrier material can be investigated under the Scanning Electron Microscope (SEM). The schematic material composition and SEM-imagery for a paraffin-graphite composite material is shown in figure 5.10

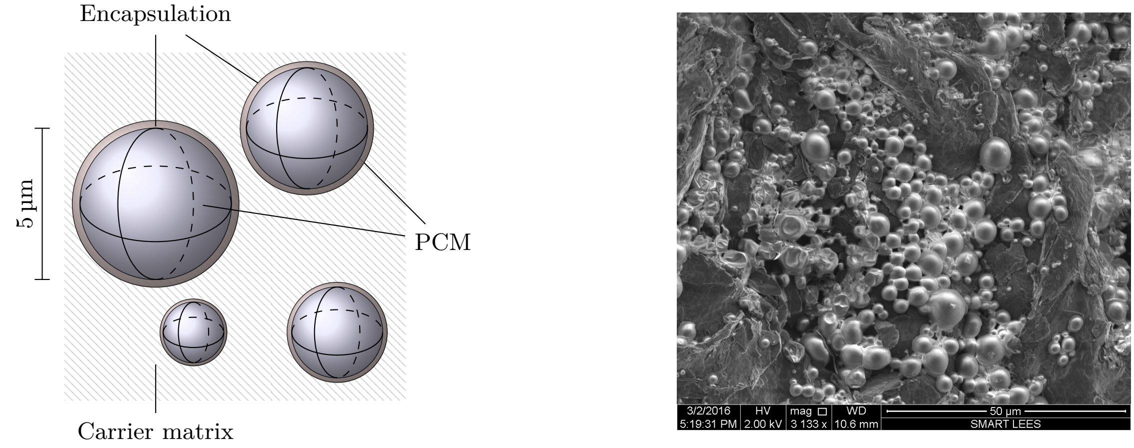

Figure 5.10: Schematic structure and SEM images of microencapsulated PCM

The opportunity to create virtually any mass composition of the individual components allows to specifically adjust PCM properties to the particular application. It is also possible to combine microencapsulated material of different kinds into the same matrix or vary storage density over different portions of the carrier.

5.4 Graphite Paraffin composite

A very promising, novel matrix material for the use with PCM is expanded graphite, which is very versatile, able to store large volumes within and comes with further advantages over other carriers. The resulting composite combines the high heat conductivity of graphite with the latent heat storage capacity of e.g. paraffin, while, thanks to the microencapsulation, keeping its macroscopic form even during phase change. Furthermore, graphite is chemically and thermally highly resistant and highly impermeable. The expanded graphite is processed from natural graphite in a three-step-process shown in figure 5.11. Imagery has been obtained using SEM. First, the natural graphite flakes are blended with an intercalation agent. The resulting graphite salt (I) is then exposed to a high temperature shock. The intercalation agent evaporates instantly, and the graphite flakes grow in volume by factor 200 to 400, forming long vermicular graphite particles (II). In a final step, the material is compressed by rollmilling into airy foams, sheets or compact foils (III) [19].

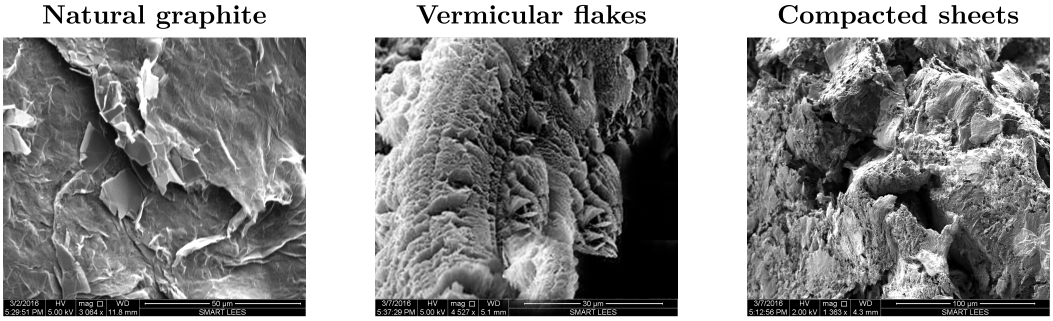

Natural graphite **Vermicular flakes** **Compacted sheets**

Figure 5.11: Steps of expanded graphite production

Due to the flexibility of the final compacting step, material properties and resulting thermophysical behavior can be controlled accurately. By defining the density, also other properties, as thermal conductivity and specific heat of the matrix can be adjusted directly. Figure 5.12 illustrates the almost linear dependancy between density and thermal conductivity for five selected and experimentally investigated samples.

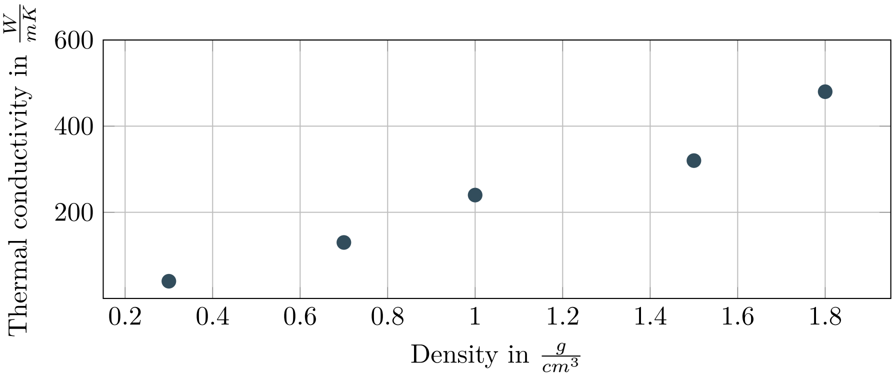

Figure 5.12: Thermal conductivity as a function of graphite matrix density

The change in density also has an impact on the plasticity of the matrix, resulting in a variation of thermal contact resistance. Lower densities lead to a more plastic deformation of the material, and hence, a significantly reduced thermal resistance even at low contact pressures. Data from four different samples of expanded graphite with densities between 0.7 $\frac{g}{cm^3}$ and 1.8 $\frac{g}{cm^3}$ is presented in figure 5.13.

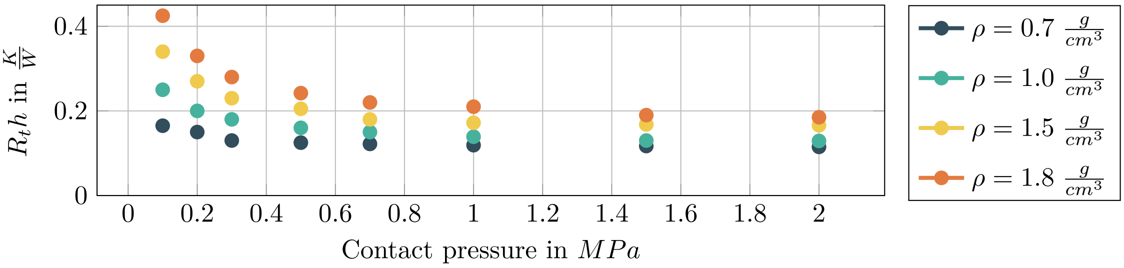

Figure 5.13: Thermal contact resistance as a function of graphite matrix density

In the end, the density of the expanded graphite by nature also determines the maximum amount of encapsulated paraffin, that can be stored within, and hence, the maximum latent heat storage capacity of the composite material. In the context of this work, three different variants have been investigated in more detail. Recorded micro-CT cross section views and thermophysical data of the graphite carriers are presented in figure 5.1. Thermal conductivity is stated separately for in-plane ($\lambda_{\parallel}$) and cross-plane ($\lambda_{\perp}$), with reference to the rolling plane. The highly anisotropic character, allows for deliberate design choices. Depending on the application, the PCM can be mounted in an orientation that enhances heat dissipation into the material or the perpendicular orientation, that accelerates heat spread within the material.

Table 5.1: Selected types of expanded graphite matrices

	(A) 0.1 $\frac{g}{cm^3}$	**(B) 0.15 $\frac{g}{cm^3}$**	**(C) 0.2 $\frac{g}{cm^3}$**
	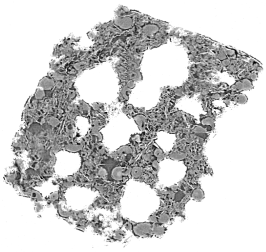	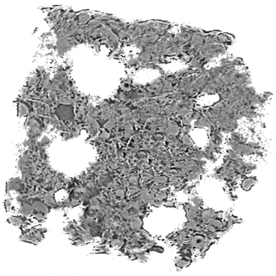	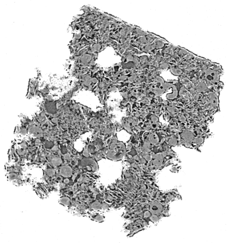
$\boldsymbol{\lambda_{\parallel}}$	12 $\frac{W}{mK}$	23 $\frac{W}{mK}$	30 $\frac{W}{mK}$
$\boldsymbol{\lambda_{\perp}}$	9.1 $\frac{W}{mK}$	8.7 $\frac{W}{mK}$	8.5 $\frac{W}{mK}$
$\boldsymbol{c_p}$	0.77 $\frac{J}{gK}$	0.74 $\frac{J}{gK}$	0.72 $\frac{J}{gK}$

Each of the three matrices has been infiltrated with two different microencapsulated paraffins, differing in melting temperature T_{melt} and latent heat L, resulting in a total of six different sample materials (A1-C2), that are used throughout the following BTMS considerations. Table 5.2 summarizes the samples' thermophysical properties and displays SEM images of the respective sample types, that clearly show the varying package density of encapsulated paraffin spheres. TPS measurements confirm, that with higher paraffin mass share, thermal conductivity, especially in-plane, decreases. Due to the aligned layered structure of the graphite, changes in cross-plane direction turn out less noticeable.

Table 5.2: Selected types of graphite based PCM composites

	(A1)	**(B1)**	**(C1)**
	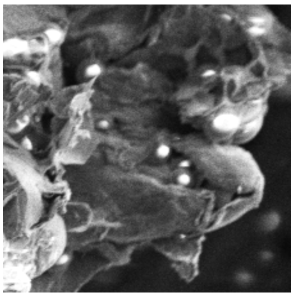	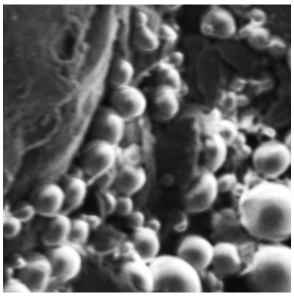	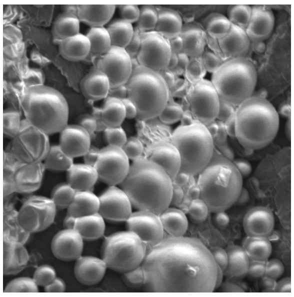
	Mass fraction of paraffin ↗		
$\boldsymbol{T_{melt}}$	**28 °C**	**28 °C**	**28 °C**
$\boldsymbol{L}$	**83 $\frac{kJ}{kg}$**	**115 $\frac{kJ}{kg}$**	**140 $\frac{kJ}{kg}$**
$\frac{m_{Paraffin}}{m_{tot}}$	0.34	0.47	0.58
ρ	0.372 $\frac{g}{cm^3}$	0.503 $\frac{g}{cm^3}$	0.601 $\frac{g}{cm^3}$
$\lambda_{\parallel}$	22 $\frac{W}{mK}$	16 $\frac{W}{mK}$	7 $\frac{W}{mK}$
$\lambda_{\perp}$	4.2 $\frac{W}{mK}$	4.3 $\frac{W}{mK}$	3.9 $\frac{W}{mK}$
	(A2)	**(B2)**	**(C2)**
$\boldsymbol{T_{melt}}$	**38 °C**	**38 °C**	**38 °C**
$\boldsymbol{L}$	**79 $\frac{kJ}{kg}$**	**112 $\frac{kJ}{kg}$**	**132 $\frac{kJ}{kg}$**
$\frac{m_{Paraffin}}{m_{tot}}$	0.38	0.53	0.63
ρ	0.399 $\frac{g}{cm^3}$	0.548 $\frac{g}{cm^3}$	0.637 $\frac{g}{cm^3}$
$\lambda_{\parallel}$	21.8 $\frac{W}{mK}$	15.2 $\frac{W}{mK}$	6.8 $\frac{W}{mK}$
$\lambda_{\perp}$	3.8 $\frac{W}{mK}$	4.0 $\frac{W}{mK}$	3.6 $\frac{W}{mK}$

Dynamic behavior

As already highlighted in section 5.1, the dynamic behavior of PCMs is among the most limiting factors in real applications, as it determines the rate at which energy can be stored and released. For practical dimensioning, the dynamic behavior can be described by the speed, the phase change front penetrates into the material. When considering a sample with infinite extent in x- and y-direction, and a constant heat flux, transient penetration depth in z-direction ($\lambda_\perp$ perpendicular to the rolling plane) is only dependent on the material properties. Simulation data for the samples A1 to C2, obtained by the models described in section 6, is summarized in figure 5.14. The data allows to estimate the time it takes to fully transform a sample of 30 mm thickness, depending on the selected material. Values range from 300 s for the highly conductive low melting sample A1, up to more than 3000 s for the more inert high storage/high melting point material C2.

In case the available PCM volume is given, those simulations can be utilized in order to select the optimum material, making sure no fraction remains unused during regular operation.

Obtaining such simulation data requires a computational model of PCM properties and behavior. Accordingly, a selection of modeling approaches is presented in the following section in more detail.

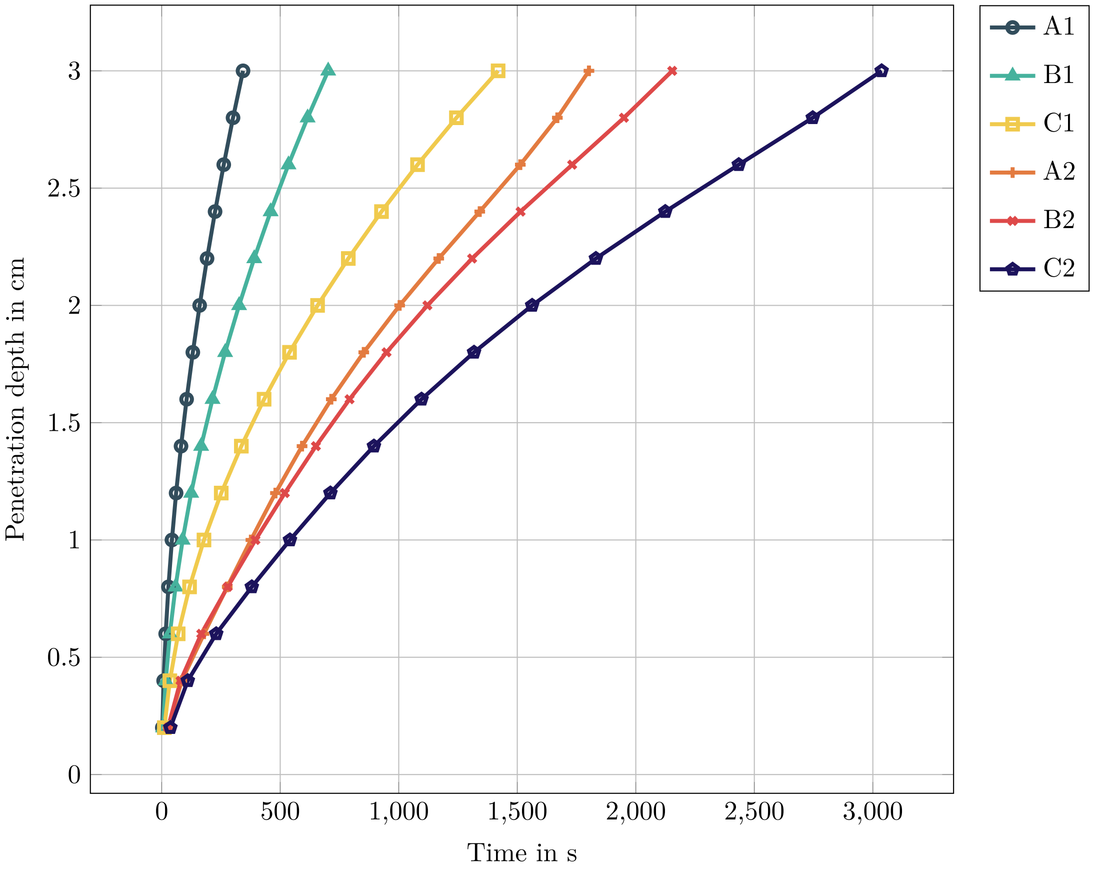

Figure 5.14: Transient penetration depth of selected PCM samples

6 Modeling PCM

There are several possible ways of providing analytic and numerical solutions for phase change processes. Their common goal is to predict properties and behavior with high spatiotemporal precision in order to deliver input for design and layout decisions.

6.1 The Stefan problem

The fundamental boundary value problem related to phase transition processes is widely know as "Stefan problem" or "free boundary value problem". A partial differential equation is utilized to describe a moving boundary $s(t)$ between two distinctive but seperate phases and determine their internal temperature distribution [69]. As the exact location of the phase interface $s\left(t\right)$ is a priori unknown, its determination is part of the problem. Per definition, the temperature at $s\left(t\right)$ equals the melting temperature (equation 6.1) and the boundary values for both sides are identical (equation 6.2). For melting or solidifying, the interface plane is moving in one or the other direction. Assuming the setup in figure 6.1, and $t_2 > t_1$, for the melting case the following hypothesis is applicable: $s\left(t_2\right) > s\left(t_1\right)$. The reverse case of solidification is characterized by $s\left(t_2\right) < s\left(t_1\right)$ [67].

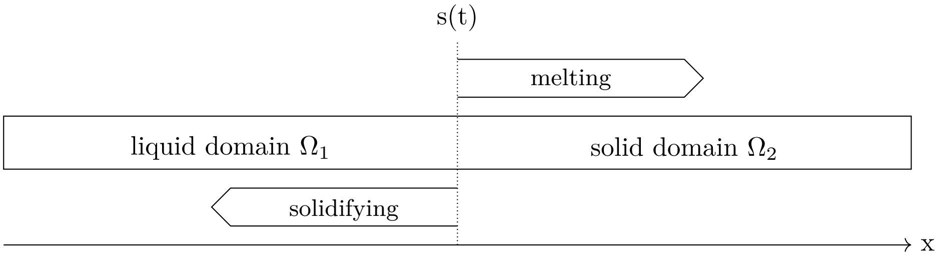

Figure 6.1: Fundamental layout of a one-dimensional Stefan Problem

$$T\left(s\left(t\right),t\right) = T_m \qquad (6.1)$$

$$\lim_{x \to s(t)^+} T\left(x,t\right) = \lim_{x \to s(t)^-} T\left(x,t\right) = T_m \qquad (6.2)$$

For the very simple setup mentioned above, heat energy turnover over a timestep Δt can be calculated as a function of the interface displacement, the interface area A, material density ρ and specific latent heat L according to equation 6.3.

$$Q = A \cdot \left[s\left(t + \Delta t\right) - s\left(t\right)\right] \cdot \rho \cdot L \qquad (6.3)$$

6.2 Analytical solution

In order to analytically solve the Stefan problem for a melting sample and determine the position of the interface area $s\left(t\right)$, the temperature distribution in the solid domain $T_{sol}\left(x,t\right)$ and the liquid domain $T_{liq}\left(x,t\right)$, functions that fullfil the requirements stated in equations 6.4 to 6.6 have to be identified [102].

$$\frac{\partial^2 T_{sol}}{\partial x^2} = \frac{1}{\alpha_{sol}}\frac{\partial T_{sol}}{\partial t} \qquad \text{in} \quad 0 < x < s\left(t\right) \tag{6.4}$$

$$\frac{\partial^2 T_{liq}}{\partial x^2} = \frac{1}{\alpha_{liq}}\frac{\partial T_{liq}}{\partial t} \qquad \text{in} \quad s\left(t\right) < x < \infty \tag{6.5}$$

$$k_{sol}\frac{\partial T_{sol}}{\partial x} - k_{liq}\frac{\partial T_{liq}}{\partial x} = \rho L\frac{\partial s(t)}{\partial t} \tag{6.6}$$

Therefore, several simplifying assumptions have to be made [143]:

- Interface $s\left(t\right)$ is a sharp and plane front with no thickness.
- Melting temperature T_m at the interface is constant and known ($T_s < T_m < T_l$).
- Amount of specific latent heat L is constant.
- Specific heat capacities $c_{p,sol}$ and $c_{p,liq}$ are different but constant within the two phases.
- Thermal conductivity λ_{sol} and λ_{liq} is different but constant within the two phases.
- There is no change in volume during phase change ($\rho_{liq} = \rho_{sol}$).
- Temperature is only dependent on x and t.
- Subcooling and nucleation are neglected.

Furthermore, boundary conditions and initial values have to be defined as follows:

Boundary conditions

- Dirichlet type boundary conditions can be set, defining fixed temperatures at the domain boundaries $T(x = 0, t) = T_1$.
- As an alternative, also Neumann boundaries, defining a fixed heatflux $\frac{dT}{dx}(x) = const.$ can be considered.

Initial conditions

- At the start, the phase change front is at the outer lateral side and has not emerged into the material yet. $s\left(t=0\right)=0$
- Initial temperature is uniform and lies below the melting temperature at all locations. $T\left(x,0\right)=T_0<T_m$

Exact solution

Under these prerequisites, a solution for the showcased melting problem can then be of the form that is given in equations 6.7 to 6.9 and referred to as Neumann solution [2]:

$$T_l\left(x,t\right)=T_0+B\cdot erf\left[\frac{x}{2\sqrt{\alpha_l t}}\right] \tag{6.7}$$

$$\text{with} \qquad B=\frac{T_m-T_0}{erf\left(\lambda\right)} \tag{6.8}$$

$$\text{and} \qquad \lambda=\frac{s\left(t\right)}{2\sqrt{\alpha_l t}} \tag{6.9}$$

λ must now be defined in a way that satisfies the heat balance at the interface, e.g. as stated in equation 6.10. Several further methodologies for the analytical solution of the Stefan problem can be found in literature inter alia in [2], [102] and [105].

$$\lambda e^{\lambda^2}erf\left(\lambda\right)=\frac{c_p\left(T_0-T_m\right)}{L\sqrt{\pi}} \tag{6.10}$$

6.3 Numerical models

Analytical models help to understand the fundamental physical dependencies and predict $s(t)$ and $T(x,t)$. However, their drastic simplification and the limitation to simple geometries require another approach for most complex real-life problems. With the everlasting increase in available computational power, numerical methods based on finite elements or finite voluminas are used in order to model phase change processes numerically and generate approximate solutions for the Stefan problem today. Therefore, the calculation domain is divided by a calculating mesh, and solution data is generated at the mesh's nodes. The description of phase change behavior via numerical models can be realized by several approaches [62]. The most common ones are presented in the following and compared at the end of the section, before a selection for the model used in the following case studies is made.

Temperature dependent heat capacity

One approach to calculate the new temperature of the node and reflect the latent heat stored, is to utilize a temperature dependent specific heat capacity, featuring a distinct peak at the melting temperature. The integral over the c_p peak then equals the latent heat storage capacity according to equation 6.11 [119]. If T_1 and T_2 are chosen to delimit the melting range exactly, $\Delta h_{T_1 \to T_2} 2$ equals the latent heat storage capacity L.

$$\int_{T_1}^{T_2} c_p\,(T)\,dT = \Delta h_{T_1 \to T_2} \approx L \qquad (6.11)$$

Depending on the type of material, a single melting temperature or a temperature range can be modeled according to figure 6.2. The approach is straightforward, simple to implement and allows efficient simulation [23]. However, the fact that it does not distinguish between cooling and heating, makes it not suitable for materials with a large temperature hysteresis. In addition to that, the method has one very critical drawback that can lead to significant errors. If, for any reason, e.g. a very coarse mesh or large timesteps, temperature increase over two successive timesteps is too big, the latent heat energy might be completely neglected, resulting in a total miss of the phase transition.

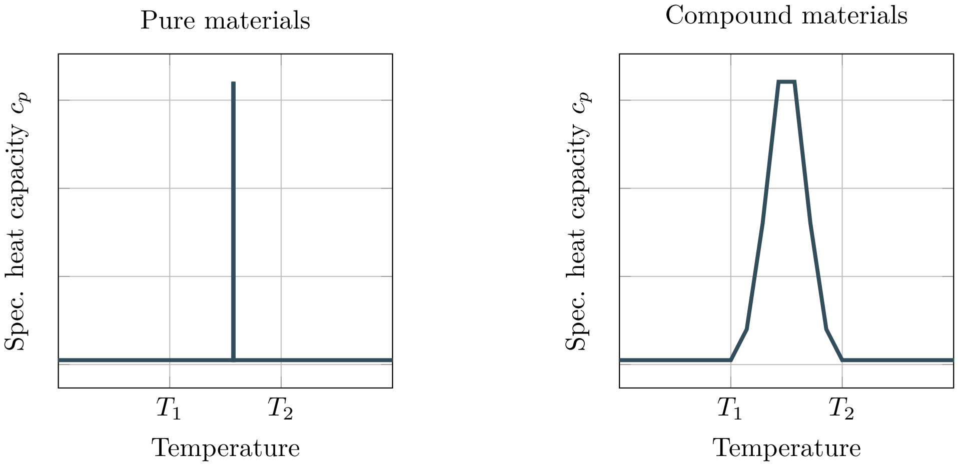

Figure 6.2: Modeling phase change by temperature dependent c_p

Direct enthalpy method

Another more sophisticated method for simulating phase change behavior and latent energy storage relies on the direct coupling between sample temperature and sample enthalpy. Therefore, heat flux into an element is directly linked to a change in enthalpy. It is valid for pure or arbitrary compound materials and easy to implement. The approach also solves the problem of small timesteps, but still does not reflect the temperature hystheresis respectively subcooling. Neither does it allow to set different melting and solidifying start temperatures for heating or cooling direction [138]. As depicted in figure 6.3 the principle for pure and compound materials only differs by the incline of the enthalpy curve.

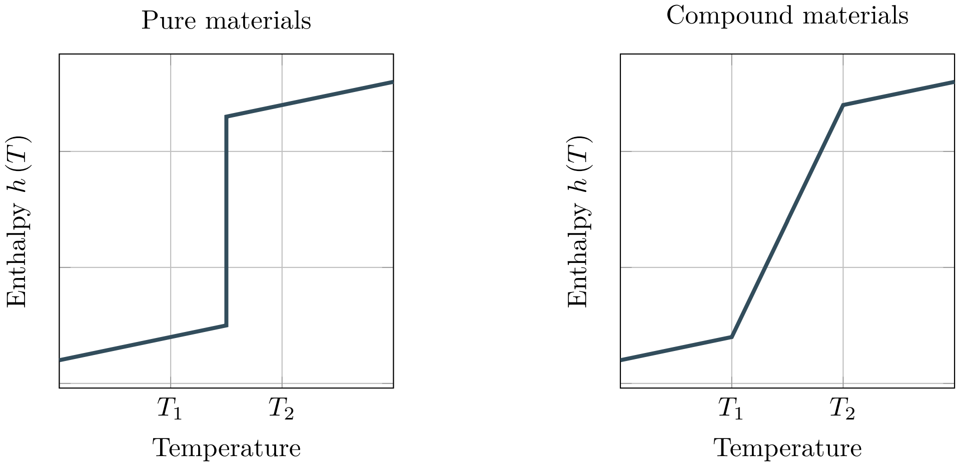

Figure 6.3: Modeling phase change by direct enthalpy method

Path dependent, heat source model

As, especially for high frequent and numerous phase changes within a small temperature region, it is essential to exactly reflect the PCM's behavior and differentiate between the melting and solidifying path of process, the two presented models have to be developed further.

This can be achieved by modeling the impact of latent heat, in form of an added source term to the enthalpy function according to equation 6.12 [39].

$$\frac{d}{dt}\rho H = \frac{d}{dx_j}\left[\lambda \frac{dT}{dx_j}\right] + Q_{PCM} \tag{6.12}$$

The source term can now be adjusted to represent the actual enthalpy-temperature relation of the sample, which can be experimentally recorded, e.g. using DSC. In order to differentiate between melting and solidifying, also the precedent timestep is taken into account when solving the current timestep. Melting is identified if $T_t > T_{t-1}$. Solidification occurs for $T_t < T_{t-1}$. The value for the additional source term Q_{PCM} can then be defined depending on actual temperature level and direction of the phase change. Real DSC data can be incorporated by defining two enthalpy functions $f(T)_m$ and $f(T)_f$ for melting and freezing. This way, the actual phase change behavior of the material, including any hysteresis is resembled. Furthermore, melting temperatures can be defined separately for freezing ($T_{sol,f}$ and $T_{liq,f}$) and melting ($T_{sol,m}$ and $T_{liq,m}$) [83]. Therefore, the following alternatives, shown in table 6.1 are considered. As this methodology by all means allows the most detailed description of actual phase transition, it has been implemented as ANSYS Parametric Design Language (APDL) script and been used for all following simulations.

Table 6.1: Temperature and path dependent source terms Q_{PCM}

	Temperature range	**Source term Q_{PCM}**	**Description**
1	$(T_t > T_{liq})$ & $(T_{t-1} < T_{sol})$	$-\frac{\rho}{\Delta t}L$	Crossing the entire slurry area within one timestep
2	$(T_t < T_{liq})$ & $(T_{t-1} > T_{sol})$	$-\frac{\rho}{\Delta t}\int_{T_{t-1}}^{T_t} f(T)_m \, dT$	Timestep completely within the slurry region
3	$(T_{sol} < T_t < T_{liq})$ & $(T_{t-1} < T_{sol})$	$-\frac{\rho}{\Delta t}\int_{T_{sol}}^{T_t} f(T)_m \, dT$	Entering slurry region
4	$(T_t > T_{liq})$ & $(T_{sol} < T_{t-1} < T_{liq})$	$-\frac{\rho}{\Delta t}\int_{T_{t-1}}^{T_{liq}} f(T)_m \, dT$	Leaving slurry region
	Temperature range	**Source term Q_{PCM}**	**Description**
5	$(T_t < T_{sol})$ & $(T_{t-1} > T_{liq})$	$\frac{\rho}{\Delta t}L$	Crossing the entire slurry area within one timestep
6	$(T_t > T_{sol})$ & $(T_{t-1} < T_{liq})$	$\frac{\rho}{\Delta t}\int_{T_{t-1}}^{T_t} f(T)_f \, dT$	Timestep completely within the slurry region
7	$(T_{sol} < T_t < T_{liq})$ & $(T_{t-1} > T_{liq})$	$\frac{\rho}{\Delta t}\int_{T_{liq}}^{T_t} f(T)_f \, dT$	Entering slurry region
8	$(T_t < T_{sol})$ & $(T_{sol} < T_{t-1} < T_{liq})$	$\frac{\rho}{\Delta t}\int_{T_{t-1}}^{T_{sol}} f(T)_f \, dT$	Leaving slurry region

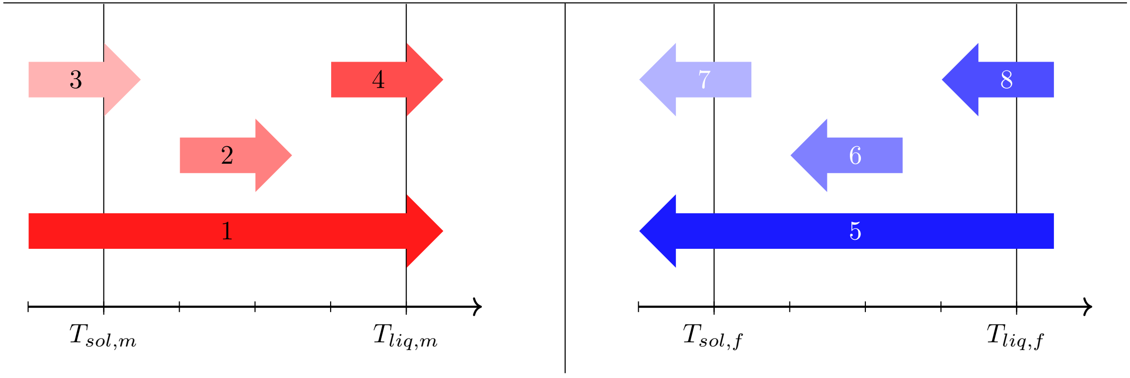

6.4 Model validation

In order to validate the suitability and accuracy of the different numerical phase change models, results of a simple experimental study are compared to the results of simulations based on the different methodologies described in the previous section. As a reference, a composite PCM slab with properties according to table 6.2 has been placed in contact with a heating plate and kept at a constant temperature of 50 °C for 1200 s at one lateral side. The transient temperature distribution of the front-facing area is recorded with an infrared camera, hence minimum, maximum and average temperatures can be calculated from the visual data obtained.

Table 6.2: Material properties for PCM sample

Dimensions	w x l x h	50 mm x 50 mm x 200 mm
Density	ρ	$0.601\ \frac{g}{cm^3}$
Melting temperature	T_{melt}	$28\ °C$
Melting temperature range	ΔT_{melt}	$2\ °C$
Specific latent heat	L	$140\ \frac{kJ}{kg}$
Thermal conductivity in plane	$\lambda_{\parallel}$	$7\ \frac{W}{mK}$
Thermal conductivity cross plane	$\lambda_{\perp}$	$3.9\ \frac{W}{mK}$

Comparing the corresponding values with the results of different simulation methods, allows a statement regarding their quality and robustness. Figure 6.4 shows an overlay of average surface temperature curves and especially highlights the weakness of the temperature dependent c_p method at large timesteps. Table 6.5 sets out the differences between the methods in more detail and compares the simulated temperature profile along the slab with the experimental thermal images at different points of time.

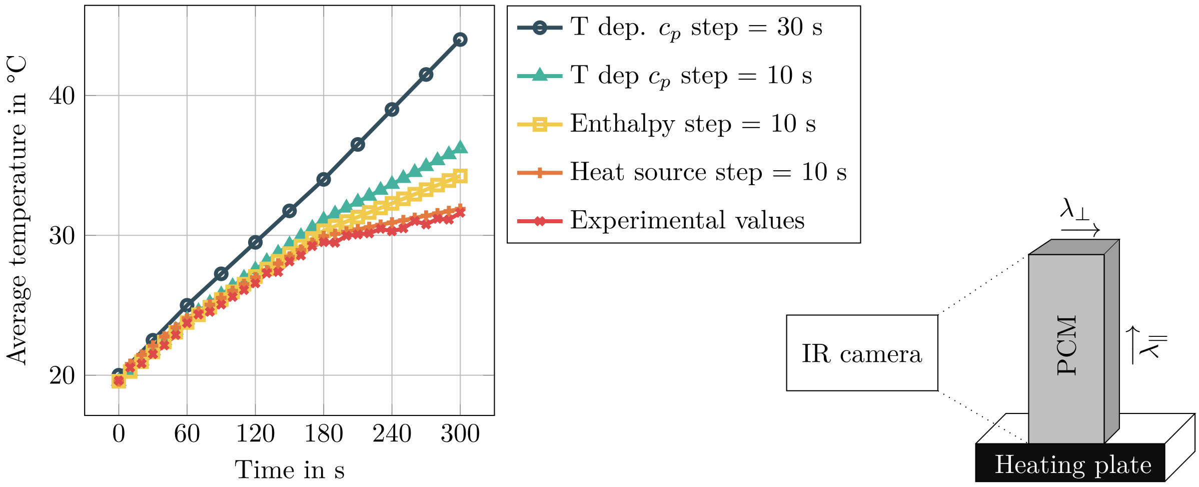

Figure 6.4: Average temperature of front surface - experiment vs. simulation models

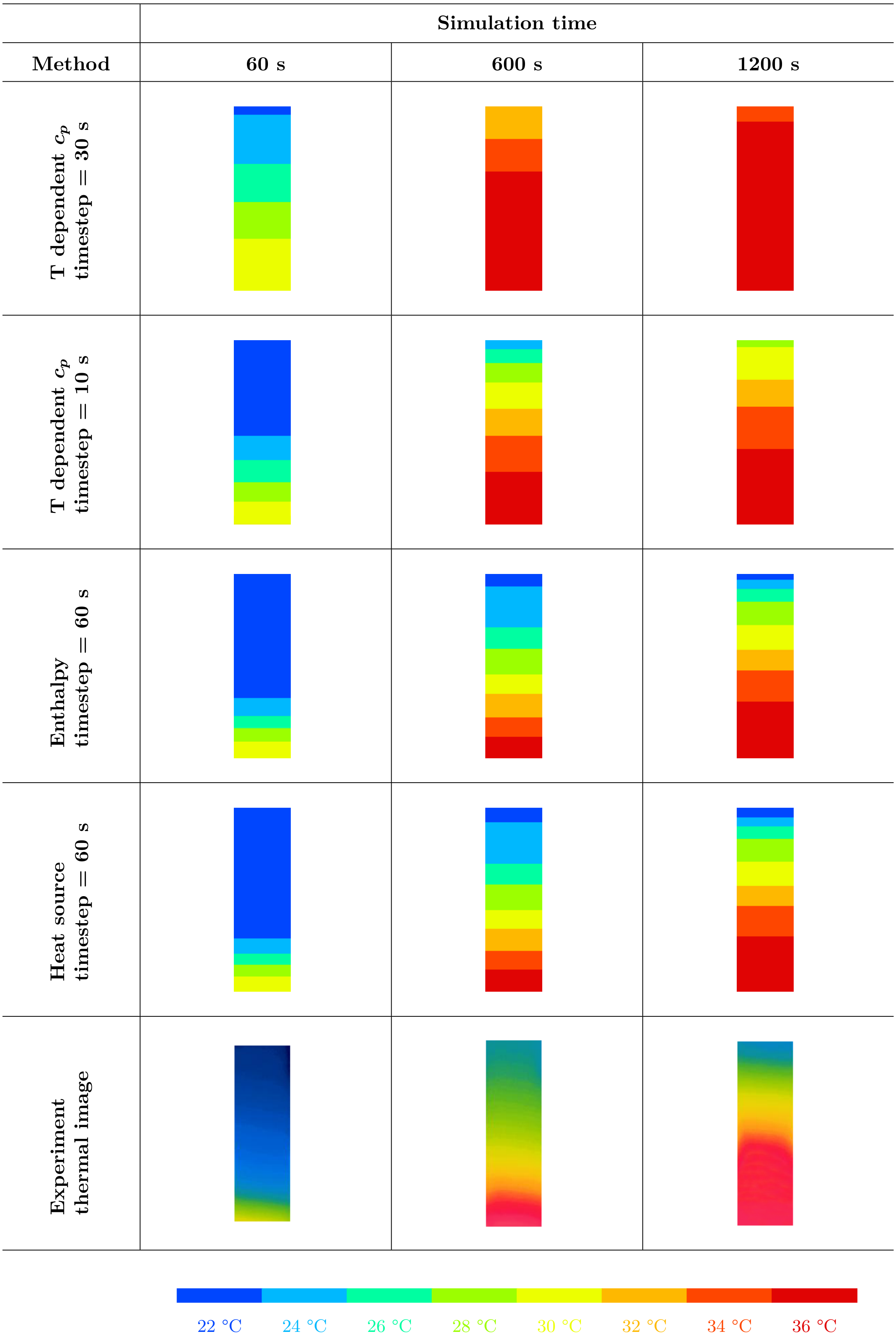

Figure 6.5: Comparison of selected numerical PCM models

7 PCM in LIB applications

7.1 Overview on existing research and implementation

PCM has already been investigated and frequently proposed for the application inside battery packs, e.g. for electric scooters or mild hybrid vehicles [98]. Detailed coupled simulation models for PCM battery interaction have been developed and are proposed among others by Greco et al. [47], experimental studies have been conducted inter alia by Tomizawa et al. [139]. However, most of the precedent work has been carried out with single cells or small modules only, mainly focusing on cylindrical form formats. Although PCM can be utilized for various applications, prior research has mostly been focusing on passive cooling and an increase of overall BTMS efficiency.

Figure 7.1 highlights the recent activities of research, differentiated by cell form factor, application and PCM use case. The form of representation points out the clustered focus of precedent work, but also the remaining blank spots, of which some shall be covered by the presented thesis. In contrast to many other publications, not only single aspects, but the whole process chain of designing, simulation and experimental validation is pictured.

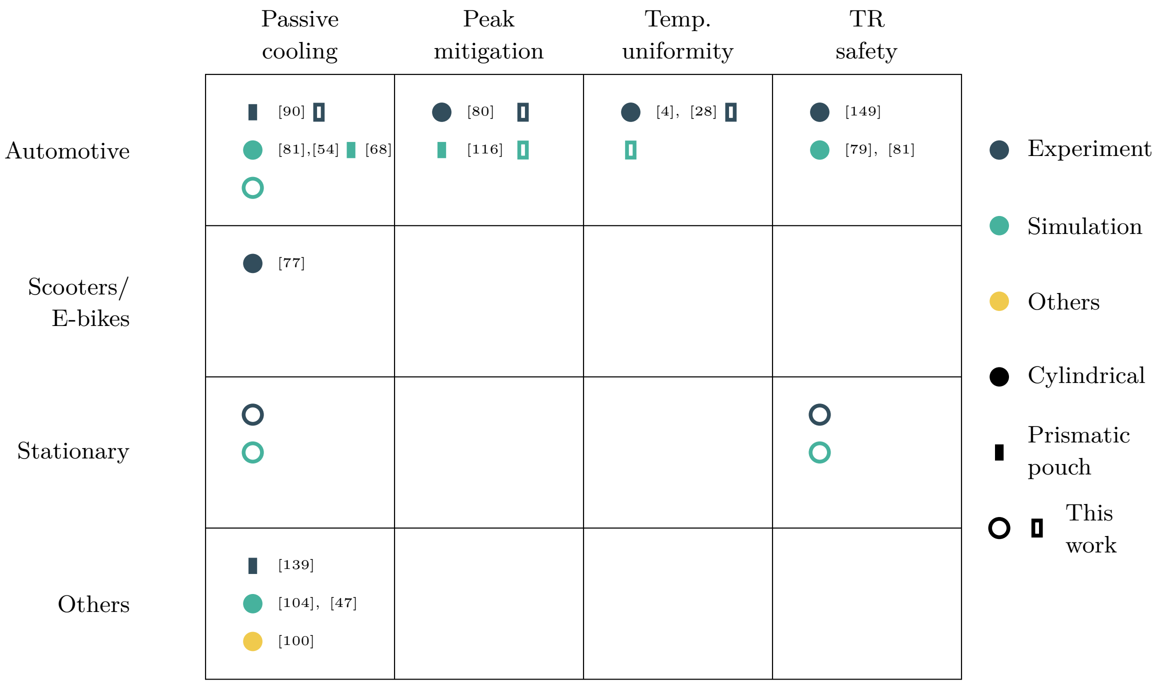
Passive cooling
Peak mitigation
Temp. uniformity
TR safety
Automotive
Scooters/ E-bikes
Stationary
Others
[90]
[81],[54]
[68]
[80]
[116]
[4], [28]
[149]
[79], [81]
[77]
[139]
[104], [47]
[100]
Experiment
Simulation
Others
Cylindrical
Prismatic pouch
This work

Figure 7.1: Overview on research landscape of PCM use in LIB applications

Although passive and energy efficient BTMS is the most obvious motivation for integration of PCM, there are also other additional possible applications, as enhancing the temperature uniformity or increasing thermal safety in case of abuse conditions. The nature of these applications highly differs in initial temperature of the battery $T_{Bat}(t_0)$, the desired maximum operating temperature $T_{Bat,max}$ and the amount and profile of heat released over the entire load cycle $\int \dot{Q}(t)dt$. Hence, different applications also demand PCM with varying material properties.

7.2 Experimental single cell studies

In order to determine the impact of different material composition on the selected applications, numerous experimental studies on LIB - PCM interaction have been conducted. In the following experiments, mainly the material samples (A1 - C2) described in section 5.4 have been utilized.

For each experimental run, the test setup comprises four 60 Ah NMC pouch cells of the same type. All cells are mounted vertically at their terminals in an identical way, depicted in figure 7.2. One reference cell is hanging free, only cooled by natural convection, while each of the other three cells is mounted symmetrically in between two identical slices of varying composite PCM samples. Initially cells and PCM are at the same temperature $T_0 = 25°C$, identical to the ambient air temperature. As experiments are conducted within a climate chamber, surrounding air is kept at approximately 25 °C at all time. During each of the experiments all four cells are exposed to the identical application specific current profile, imposed by a battery testing device. Load curves are chosen to resemble typical real life applications, as BEV charging or stationary home storage (also see section 3.3). In order to derive hints on the proper PCM selection, temperature level and distribution during the different load cycles are tracked by nine evenly distributed PT1000 Resistance Temperature Devices (RTDs) sensors, read by an Agilent data logger with a sample rate of 10 Hz.

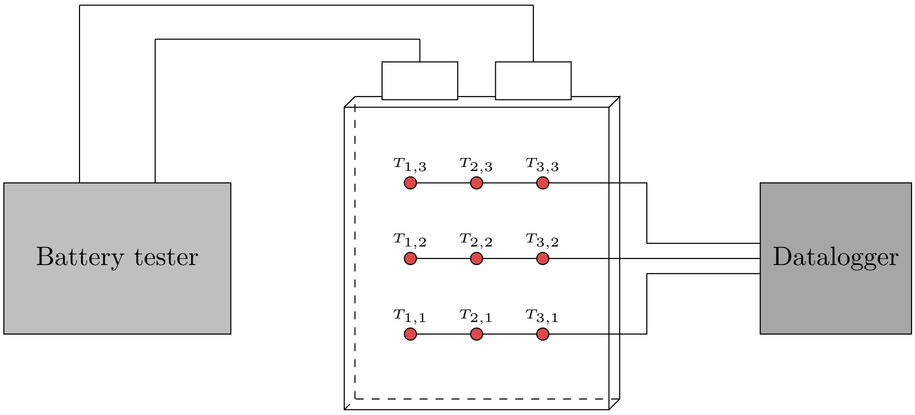

Figure 7.2: Experimental setup for single cell experiments

In the following, the results for the three most significant samples per application are presented in detail.

7.3 Passive control of temperature rise (constant moderate load)

The most obvious task for a PCM based BTMS is the control of system temperature rise under low to moderate load, in order to achieve a completely passive system, or enable the downsizing of existing cooling components. Precedent work inter alia by [81], [54], [77] has also been focused on this type of application and already proven the positive impact of PCM based systems. For the presented comparative study, a constant load during CCCV charging at the rate of 1 C is applied to the cells, resembling a typical charging process.

In the interest of the PCM being utilized efficiently, several boundary conditions have to be met. The melting temperature $T_{PCM,m}$ has to lie above the ambient temperature, guaranteeing that the latent heat storage is not consumed without battery operation. On the other hand, $T_{PCM,m}$ has to be significantly below the maximum battery temperature $T_{Batt,max}$, as the temperature difference causes the heat flux into the PCM (equation 7.1). In order to achieve an entirely passive cooling, the total latent heat storage capacity $L \cdot m_{PCM}$ must meet the amount of energy released from the cell over the cycle (equation 7.2). After the load, there has to be sufficient idle time for the cell temperature to drop below $T_{PCM,m}$ and the material to recuperate. In addition to that, the thermal conductivity of the PCM should allow a sufficient heat flux into and out of the material, as otherwise fractions of the latent heat capacity remain underutilized.

$$T_{Batt,0} << T_{PCM,m} < T_{Batt,max} \quad (7.1)$$

$$\int_{t=t_0}^{t=t_{end}} \dot{Q}\left(t\right) \mathrm{d}t < L \cdot m_{PCM} \quad (7.2)$$

As volumetric specific latent heat differs between the samples, the requirements necessitate slices of different thickness. The results of the experimental study are presented in table 7.2 and show that, for the moderate load case, all PCM setups are superior to the air cooled base scenario. The temperature peak and the temperature at the end of the charging cycle can both be reduced by 4 °C and also the average temperature is decreased by 2 °C.

Furthermore, it can be seen that the individual variants only differ slightly, which allows the assumption that even the limited thermal conductivity of the most dense material (I) is sufficient for this application. As it also allows for the most compact structural form, it is the recommended choice for the application.

Table 7.1: Properties of selected PCM samples for passive temperature control

	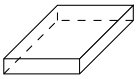	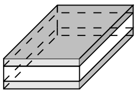	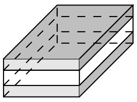	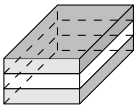
Sample	0	**C1**	**B1**	**A1**
Thickness PCM t_{PCM}	n.a.	3 mm	4 mm	5 mm
Mass PCM m_{PCM}	n.a.	227 g	302 g	378 g
Melting temp. T_m	n.a.	28 °C	28 °C	28 °C
Spec. latent heat. L	n.a.	140 $\frac{kJ}{kg}$	115 $\frac{kJ}{kg}$	83 $\frac{kJ}{kg}$

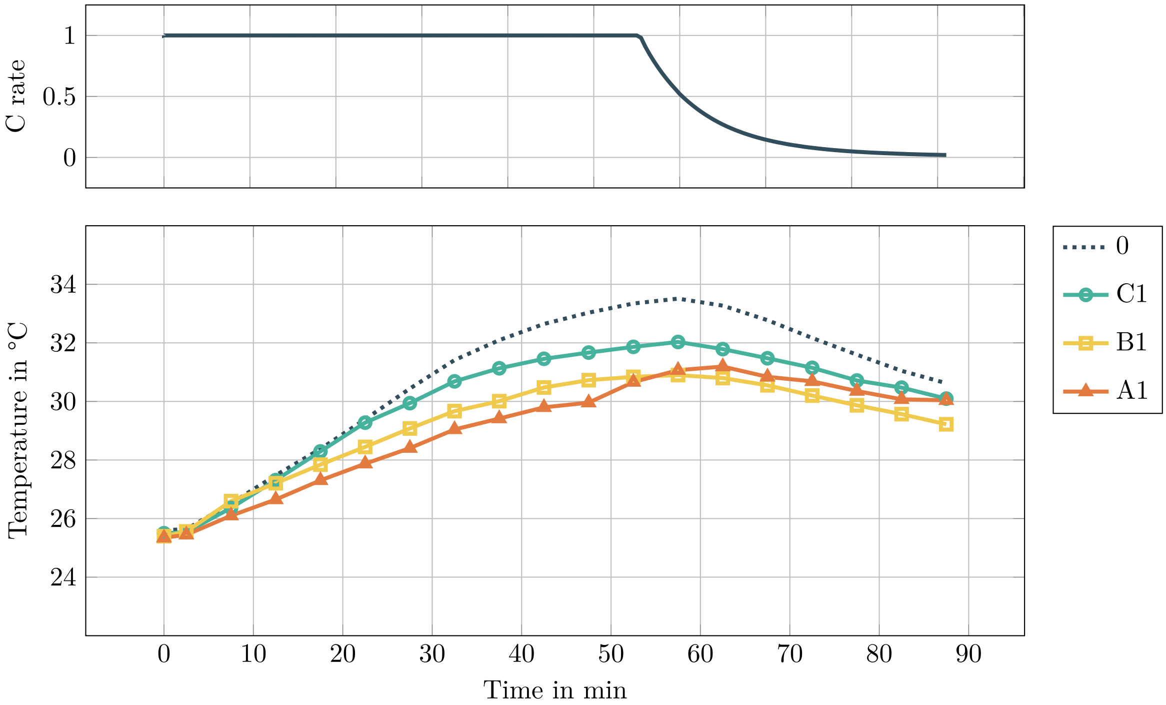

Figure 7.3: Transient temperature profiles

Table 7.2: Impact of different PCM samples used for temperature control

	0	**C1**	**B1**	**A1**
Max. Temp. T_{max}	33.56 °C	32.06 °C	30.98 °C	31.27 °C
End Temp. T_{end}	30.40 °C	29.96 °C	29.12 °C	29.99 °C
Average Temp. T_{av}	30.69 °C	29.94 °C	29.15 °C	28.92 °C

7.4 Mitigation of peak loads

Another potential application for PCM is the mitigation of peak loads, as they occur during strenuous driving maneuvers or during the fast charging at high currents. Characteristically, the peak load is limited to a certain period of time and lies significantly above the average load level. In this scenario the PCM must not necessarily absorb the whole amount of energy released. A certain controlled temperature rise ΔT_{rise} is allowable, reducing the required amount of heat storage capacity according to equation 7.4. As important as the amount of energy, is the ability of the material to absorb the heat energy fast enough. In order to achieve this, the melting point should be as low as possible as the temperature difference acts as driving force (equation 7.3). Good thermal contact and high thermal conductivity support the heat flux.

$$T_{Batt,0} < T_{PCM,m} << T_{Batt,max} \tag{7.3}$$

$$\int_{t=t_0}^{t=t_{end}} \dot{Q}\left(t\right) \mathrm{d}t - m_{Bat} \cdot c_{p,Bat} \cdot \Delta T_{rise} < L \cdot m_{PCM} \tag{7.4}$$

For the experimental study, a typical CCCV fastcharging peak has been selected, featuring a maximum C rate of three, kept constant over 16 minutes. The resulting battery temperature profiles are summarized in table 7.4. Again, the PCM equipped cells all feature lower temperature levels, but in contrast to the precedent experiment, now significant differences can be identified between cases (C1) to (A1). Due to the limited thermal conductivity of sample (C1), at a certain point, the heat flux into the material stays below the two other probes as the melting front can not move through the material fast enough. Also for probe (B1), something similar occurs at a later point of time, resulting in probe (A1) being capable of dissipating the highest amount of energy. Maximum measured battery temperature of probe (A1) lies more than 20 % below the air cooled reference and still more than 5 % below probe (C1).

The restrained rise in temperature comes with a significantly reduced average temperature that lies more than 17 % below the air reference for all three PCM samples.

In addition to the reduced peak temperature and the average temperature level, the higher thermal conductivity of probe (A1) also leads to a faster recuperation, so that at the end of the cycle, it also features a battery temperature that is more than 38 % below the reference and still 15 % below sample (C1).

Results point at the fact that for peak mitigation, a sufficient thermal conductivity of the PCM is decisive and hence favorable over pure storage capacity. However, the lower density results in more voluminous cooling elements. It is inherent that, after every peak, the material must be brought back into its initial state before it can be reused again. Depending on the frequency and extent of the peaks, ambient air can be sufficient or an additional active cooling can be required.

Table 7.3: Properties of selected PCM samples for peak load mitigation

	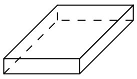	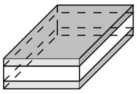	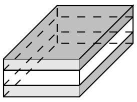	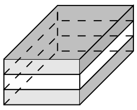
Sample		**C1**	**B1**	**A1**
Thickness PCM t_{PCM}	n.a.	3 mm	4 mm	5 mm
Mass PCM m_{PCM}	n.a.	227 g	302 g	378 g
Melting temp. T_m	n.a.	28 °C	28 °C	28 °C
Spec. latent heat. L	n.a.	140 $\frac{kJ}{kg}$	115 $\frac{kJ}{kg}$	83 $\frac{kJ}{kg}$

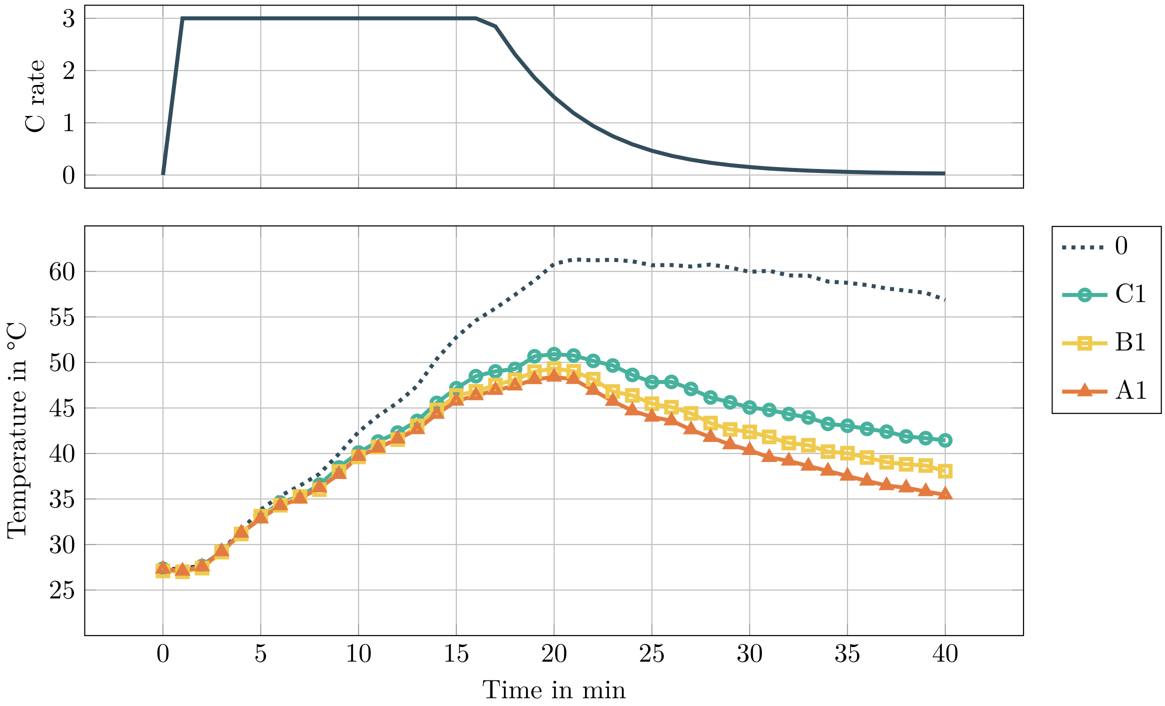

Figure 7.4: Transient temperature profiles

Table 7.4: Impact of different PCM samples used for peak mitigation

	0	**C1**	**B1**	**A1**
Max. Temp. T_{max}	61.25 °C	51.07 °C	49.17 °C	48.72 °C
End Temp. T_{end}	57.13 °C	41.34 °C	38.38 °C	35.32 °C
Average Temp. T_{avg}	50.96 °C	42.38 °C	40.64 °C	39.58 °C

7.5 Increasing temperature uniformity

The precedent experiment has shown that for certain load profiles, a highly thermally conductive PCM can be advantageous. This suggests that, during low or medium load, the same material also has positive effect on the temperature distribution within the cell, as it transfers heat from hot spots to the cooler portions of the cell surface. Furthermore, if the material is reactive enough, local hot spots can also be mitigated by local melting and freezing of the PCM. In order to estimate this effect, the sample cells are confronted with a typical stationary storage profile that shows very limited average heat release. C rates idle around approx. 0.2 during night time and feature one distinctive peak during daytime, when the storage is charged by Photovoltaics (PV) feed-in. As a consequence of this profile, the expected temperature rise is only moderate. Accordingly, a melting point near the average operating temperature and a high thermal conductivity are advantageous, as they allow utilization of the phase change even with small temperature gradients. Hence, three material samples with a melting temperature of 26 °C have been selected for the experiment (equation 7.5).

$$T_{Batt,0} \approx T_{PCM,m} << T_{Batt,max} \tag{7.5}$$

$$\Delta T\left(t\right) = max\left[T_{1,1}\left(t\right)...T_{3,3}\left(t\right)\right] - min\left[T_{1,1}\left(t\right)...T_{3,3}\left(t\right)\right] \tag{7.6}$$

The decisive figure of merit used for comparison is the measured temperature spread $\Delta T\left(t\right)$, defined by equation 7.6. As table 7.6 showcases, the additional heat capacity of the PCM leads to a slower temperature rise in all three PCM cases. However, only the two highly conductive samples have a positive impact on the overall temperature spread as they can redistribute the heat over the cell surface quickly enough. Data shows that the highest temperature spread is always measured between the sensors $T_{1,3}$ and $T_{3,3}$. By applying material A1, the maximum temperature spread can be reduced by more than 50 % to less than 4 °C, reducing local differences in internal resistance and aging. In addition to that, also the temperature recovery after the load phase occurs faster and average spread is below the air reference by 53 %.

Table 7.5: Properties of selected PCM samples for increasing temperature uniformity

	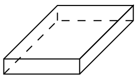	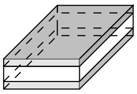	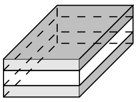	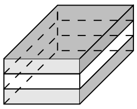
Sample		**C1**	**B1**	**A1**
Thickness PCM t_{PCM}	n.a.	3 mm	4 mm	5 mm
Mass PCM m_{PCM}	n.a.	236 g	315 g	394 g
Melting temp. T_m	n.a.	26 °C	26 °C	26 °C
Spec. latent heat. L	n.a.	137 $\frac{kJ}{kg}$	111 $\frac{kJ}{kg}$	78 $\frac{kJ}{kg}$

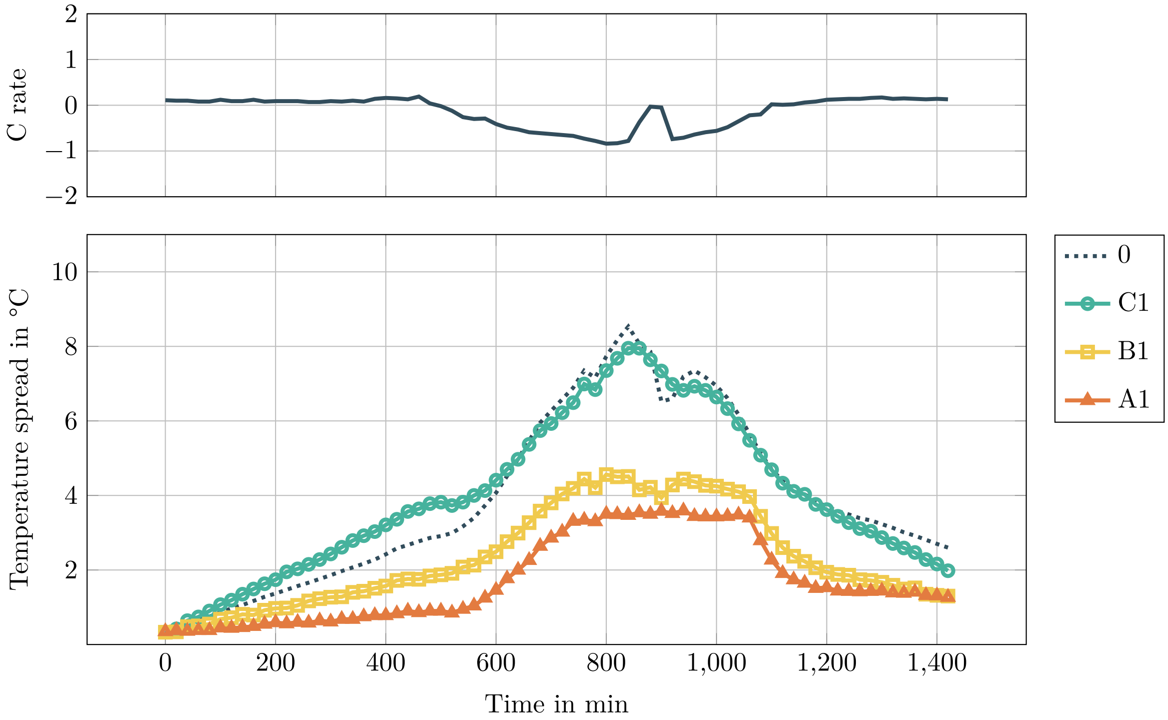

Figure 7.5: Transient temperature profiles

Table 7.6: Impact of different PCM samples used for increasing temperature uniformity

	0	**C1**	**B1**	**A1**
Max. Spread ΔT_{max}	8.62 °C	8.09 °C	4.57 °C	3.65 °C
End Spread ΔT_{end}	2.49 °C	1.82 °C	1.22 °C	1.32 °C
Average Spread ΔT_{avg}	3.90 °C	3.98 °C	2.34 °C	1.72 °C

7.6 Preventing thermal runaway

As section 2.5 has already highlighted, thermal runaway is considered one of the most critical abuse situations and results from a condition where heat can not be removed quickly enough from the cell. Storing heat temporarily inside the PCM can hence help to prevent or limit the fatal temperature rise, and can significantly add intrinsic safety to the system.

For safety reasons, this last experiment has not been conducted with a real cell, but with a cell dummy whose temperature can be controlled by resistance heating foils. The thermal load profile applied, resembles the actual heat generation during an external short circuit, that has been recorded in an ARC measurement before. The peak heat generation maxes at 2.1 kW and over the whole cycle, 250 Wh of thermal energy are released. The cell is considered safe if the maximum surface temperature remains below 120 °C. The offset between $max\left(T_{i,j}\left(t\right)\right)$ and the onset temperature can be seen as safety margin and hence is to be maximized. Samples have been chosen in a way that allows a comparison between different melting temperatures and thermal conductivity.

Material samples of moderate and high thermal conductivity at different temperature levels are used for this study.

Result data presented in table 7.8 allows to draw mainly two conclusions. For thermal runaway propagation an elevated phase change temperature is beneficial. Furthermore, high thermal conductivity is more decisive than the absolute storage capacity, which can be especially seen when comparing case (I) and (II). With known onset temperature T_{TR}, safety margin ΔT_{safe} can be derived according to equation 7.8.

$$T_{Batt,0} \approx T_{PCM,m} << T_{Batt,max} \tag{7.7}$$

$$\Delta T_{safe} = T_{TR} - max\left[T_{1,1}\left(t\right)...T_{3,3}\left(t\right)\right] \tag{7.8}$$

Experimentally obtained temperature values hint that only the higher conducting samples (II) and (III) are capable of dissipating heat fast enough away from the cell surface and ensure a safe thermal runaway prevention.

Table 7.7: Properties of selected PCM samples for prevention of thermal runaway propagation

	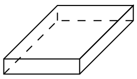	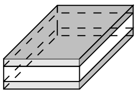	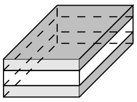	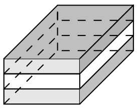
Sample		**C1**	**B1**	**A1**
Thickness PCM t_{PCM}	n.a.	3 mm	4 mm	5 mm
Mass PCM m_{PCM}	n.a.	227 g	388 g	412 g
Melting temp. T_m	n.a.	28 °C	48 °C	68 °C
Spec. latent heat. L	n.a.	140 $\frac{kJ}{kg}$	108 $\frac{kJ}{kg}$	65 $\frac{kJ}{kg}$

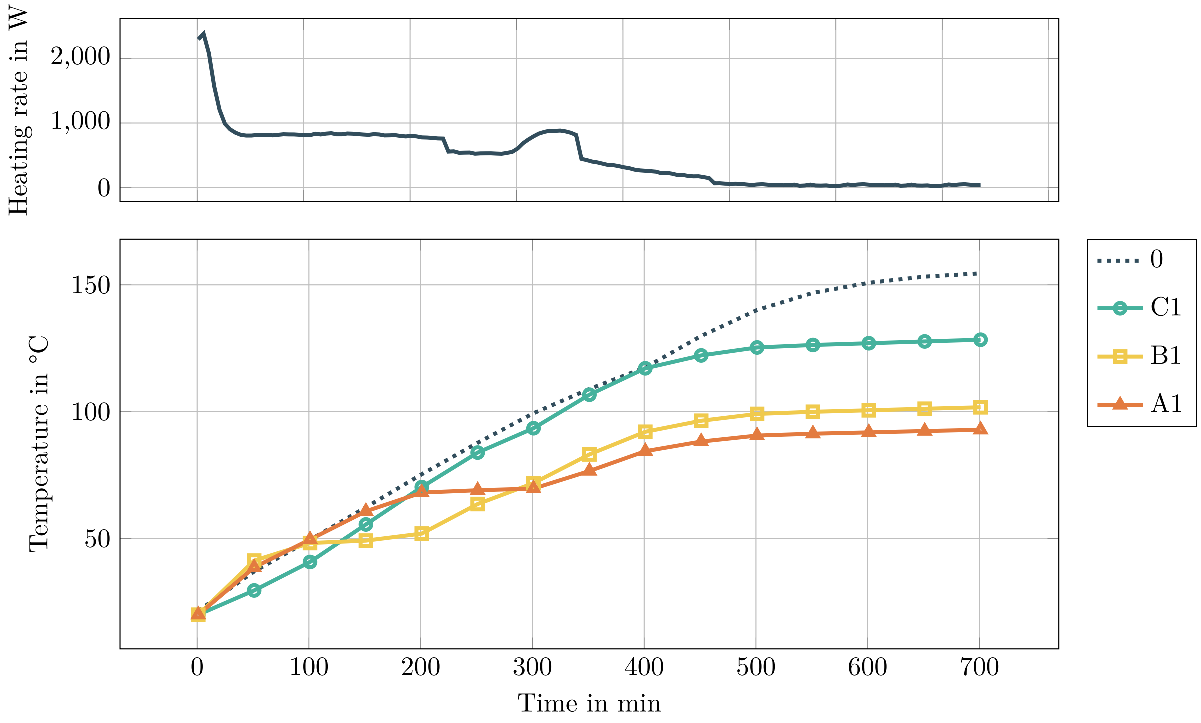

Figure 7.6: Transient temperature profiles

Table 7.8: Impact of different PCM samples used for TR propagation prevention

	0	**C1**	**B1**	**A1**
$\Delta T_{safety,min}$	-15.14 °C	11.13 °C	37.82 °C	46.74 °C
$\Delta T_{safety,avg}$	34.26 °C	45.40 °C	62.89 °C	65.55 °C

7.7 Summary of single cell experiments

The precedent section has proven that different target applications require different PCMs in order to benefit from the latent heat storage capability. Based on the observations made and data from additional experiments, the qualitative sensitivity towards single parameters can be estimated and a descending order of importance can be defined for all the individual applications. Table 7.9 summarizes the findings and proposes an order of priority for the design parameters. Naturally, those parameters can not be independently changed, as they interfere, but the proposed scheme can be used as starting point.

Table 7.9: Basic requirement scheme for different applications

	Decreasing impact ↘		
Application	**1.**	2.	3.
Passive cooling	$\boldsymbol{T_{melt}}$	L	λ
Peak mitigation	$\boldsymbol{\lambda}$	T_{melt}	L
Temperature uniformity	$\boldsymbol{\lambda}$	L	T_{melt}
TR prevention	$\boldsymbol{\lambda}$	T_{melt}	L

As the overview shows, some of the applications feature conflicting design requirements, whereas others are more aligned and may be combined. E.g. peak mitigation and thermal runaway prevention seem to be achievable with almost similar material, so that both applications can be considered in parallel.

The actual benefit of PCM integration for real life applications, however, also depends on several additional aspects as ambient temperatures and is furthermore limited by boundary conditions as available space or weight constraints. Limitations can be mitigated by an adapted overall cooling strategy, that actively controls at what point of time and to what extent the PCM is utilized. When combined with an active cooling system, even more opportunities arise, e.g. adapting the PCM use to the battery SOC or SOH.

An indication of the usefulness and efficiency of PCM integration can be derived from the fraction of thermal storage capability that is frequently used. By putting this parameter in relation to the electric energy amount turned over, a use-factor according to equation 7.9 can be defined. Using this parameter, the single cell experiment data and the simulation models of section 6, BTMS can also be designed, dimensioned and layouted for more complex multicell systems.

$$\eta_{PCM} = \frac{\int \dot{Q}}{\int P_{el}} \tag{7.9}$$

8 Design methodology - case studies

When designing a PCM based BTMS, a unified and structured approach is proposed following standardized steps. As shown in the previous section, the order of defining the individual properties shall be derived depending on the targeted application, as in table 7.9. Accordingly, standardized design schemes can be postulated. The example steps depicted in figure 8.1 are given for a passive cooling application, where, as a starting point, the melting temperature has to be selected according to the desired cell temperature, ambient temperature and the overall-system design. Afterwards the required amount of PCM latent heat can be determined from the heat generation of the respective application cycle.

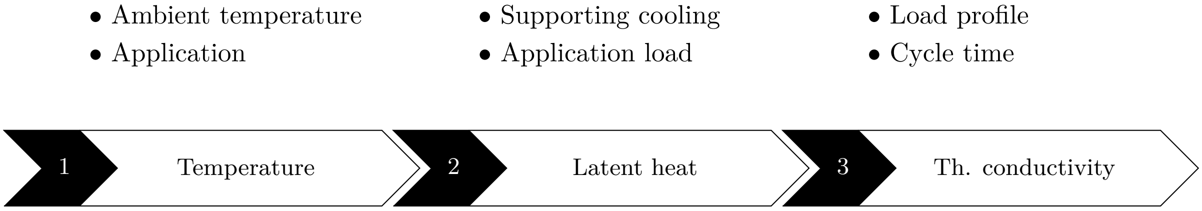

Figure 8.1: Methodology for PCM selection

The resulting requirements in terms of temperature affect the selection of the paraffin type - the required amount of heat affects its mass. The importance of dynamics determines the mass fraction of paraffin and graphite and hence the final composition as well as volume and weight.

Case studies

In the following, three detailed case studies of PCM integration based on the proposed design methodology are presented. Hereby, the most relevant applications in automotive and stationary storage are covered and investigated in simulation and experiment. In order to allow a comparison between the cases, the reports are structured in the same way. The starting point is a brief description of the application, followed by an estimation of load profile and heat generation. Subsequently, the reference cooling design and the battery layout are presented, before the simulation-based design methodology is applied. Wherever applicable, the proposed design is validated experimentally and a conclusion is drawn from the observations made.

8.1 Case study: Mitigation of peak loads during fast charging

According to market studies, limited range and long charging time are the main barriers that restrain a higher market share of electric cars. This is especially valid in professional applications, where non-operational charging times directly cause economic costs. Hence, there is a trend towards fast charging with charging between 1 C and 5 C [108]. However, as highlighted in chapter 2, those currents lead to a drastic increase in heat release and therefore increase the load on the BTMS. High thermal load and larger temperature spreads furthermore accelerate aging and reduce the lifetime of the battery system [107].

In order to investigate the impact of frequent fast charging and BEV operation under challenging tropical ambient conditions, a Singaporean German research cooperation named TUM CREATE has been established in 2011. Within the project the prototype of an all electric taxi vehicle EVA has been developed. The main design goal was to enable a continuous two-shift taxi operation with driving ranges of more than 200 km per charge and extremely reduced recharging times. Resulting vehicle design specifications and the technical key data are given in figure 8.2. The novel approach and the consequent orientation towards a purpose driven BEV design, have given the unique opportunity to integrate novel technologies as PCM battery cooling and evaluate their benefit under real life conditions.

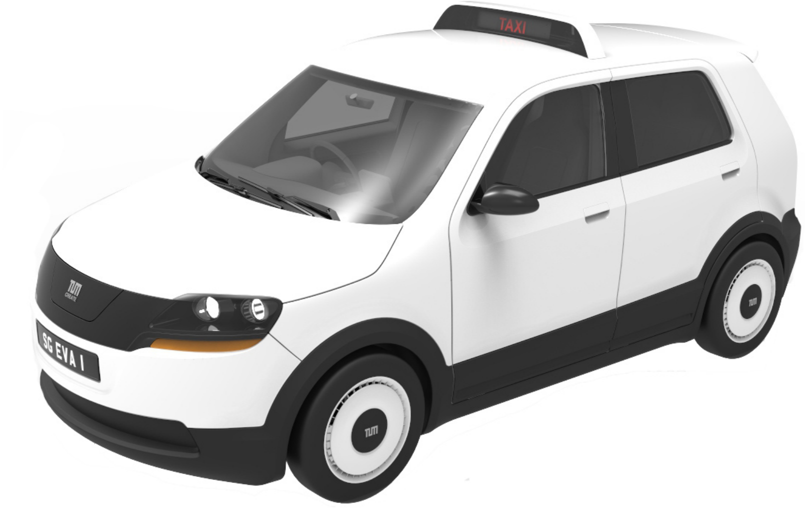

Figure 8.2: Electric taxi concept EVA

Table 8.1: Specifications of electric taxi concept EVA

Overall dimensions (l × w × d):	4,316 mm × 1,794 mm × 1,679 mm
Overall weight:	1,500 kg
Driving range:	330 km (U.S. FTP72 standard) 200 km (Real daily driving pattern)
Max. power:[1]	60 kW
Max. speed:[1]	111 $\frac{km}{h}$

---

[1] Electronically limited

Load profile

The proposed vehicle shall replace conventional Internal Combustion Engine (ICE) taxi vehicles, and hence has to match or even excel their performance. Based on real-life driving data, recorded with a fleet of taxi vehicles, a reference Singapore driving cycle is postulated that acts as corner stone for the derivation of vehicle and battery dimensioning and design. In combination with the vehicle energy model and the data of the selected battery topology, the velocity and acceleration data is transformed into a current profile covering the time between two charging breaks. The profile is complemented by the charging periods that are limited to constant current phase only, at a C rate of three and account for approximately 20 minutes. Figure 8.2 depicts the current profile for a single battery cell over one operational day, which is clearly dominated by the four recurring fast charging peaks.

The heat release from the whole battery pack over such a load pattern is estimated from adiabatic ARC measurements on single cells, cycled with the modeled current profile. Values are verified by comparison to the simple ohmic heat release, based on equation 8.1. In order to account for aged cells and their increased internal resistance, the following BTMS dimensioning comprises a safety factor $\beta = 2.0$, doubling the heat generation values.

$$\dot{Q}(t) = I(t)^2 \cdot R(t) \tag{8.1}$$

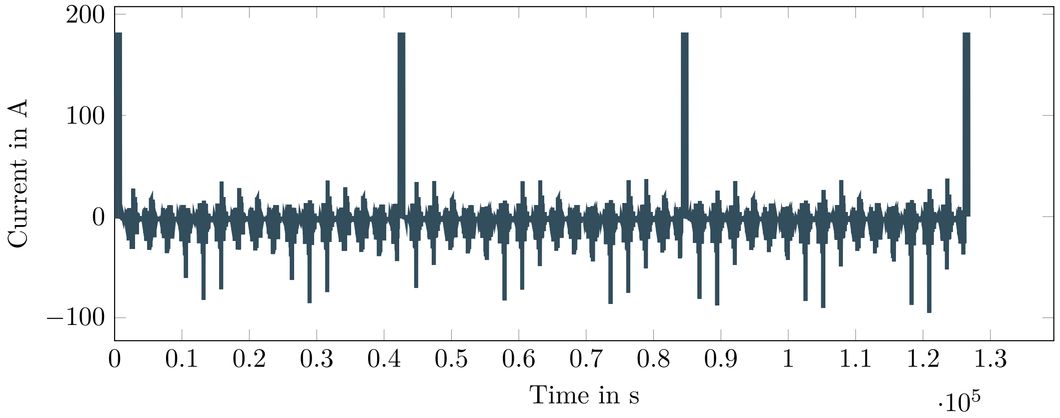

Table 8.2: Singapore driving cycle - single cell load profile

	driving	**charging**
Average current:	-16 A	165 A
Max. current:	-75 A	180 A
Average heat generation:	0.23 W	15.12 W
Max. heat generation:	3.03 W	16.75 W

Cooling concept

Given the tropical ambient temperatures, the concept vehicle features a powerful refrigerant circuit for cabin cooling, that also acts as heat sink for the BTMS. The active battery cooling is achieved via liquid cooling plates, integrated into a water-glycol based coolant cycle. This loop is coupled to the vehicle's main refrigerant circuit via a high performance chiller. By using a three-way-valve, cooling power can actively be distributed between the cabin cooling loop and the battery chiller. Hence, the overall cooling power can be estimated by superposing cabin cooling and battery cooling requirements. Unfortunately, both applications feature high peak values. For the cabin, peak power is mainly originating from initial cool down after parking, battery cooling requires the maximum power during the fast charging process. In order to achieve maximum operational flexibility, all cooling components must be dimensioned in a way that allow both power demands to be fulfilled at the same time.

This leads to the challenge that if cooled solely by active components, power requirements and hence dimensions of the whole cooling system would be significant. As a result, heavy and voluminous cooling components would have to be integrated that are only intermittently used and do not operate at their optimum operating point during most of the time. Therefore, a combined layout is chosen, in which the active refrigerant-based cooling system is supported by passive PCM elements, allowing for smaller component sizes. The basic layout of the system and assumed power requirements are given in figure 8.3. Values have been determined in close collaboration with the department responsible for vehicle thermal management [65].

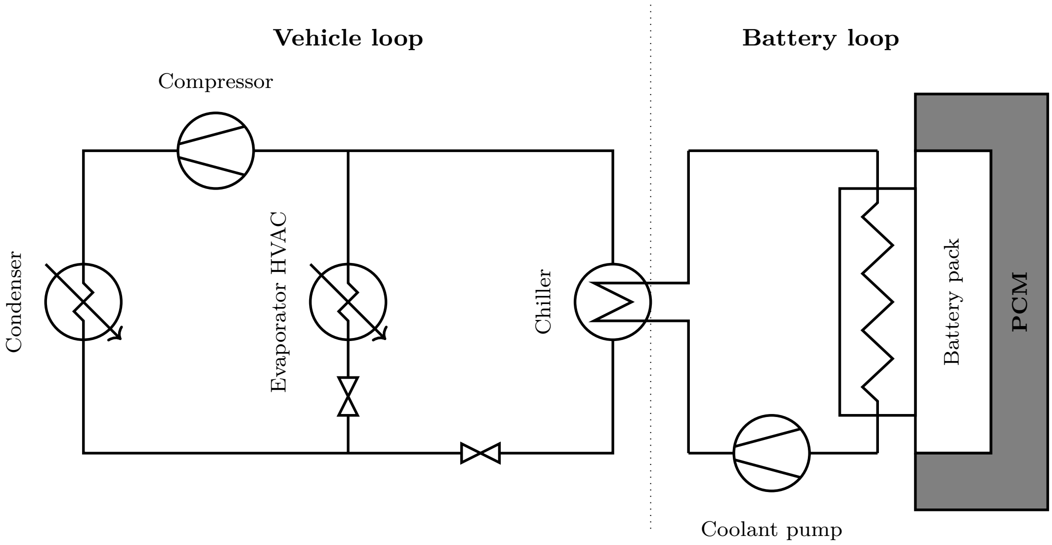

Figure 8.3: EVA cooling concept

Table 8.3: Specifications of EVA cooling loops

	Cabin loop	**Battery loop**
Average power requirement:	2.2 kW	1.5 kW
Max. power requirement:	7 kW	12 kW

Battery system layout

The core component of the vehicle's drivetrain is the battery pack mounted in its underfloor. The available packaging space of approx. 2100 mm x 1200 mm x 182 mm results in a flat design covering almost the entire area in between the vehicle axles. Due to crash requirements and the large width of the battery, the pack is structurally integrated and acts as load bearing component which is capable of absorbing crash loads. The battery pack is composed out of 18 identical cell stacks, which are attached to two aluminum cooling plates in groups of three. All stacks are connected in series in order to achieve the nominal voltage of 400 V. Focusing on an integral design and using lightweight materials, as Carbon Fibre Reinforced Plastic (CFRP) for the casing and base plate, the overall weight of the system is kept below 500 kg, resulting in an gravimetric energy density of 100 Wh/kg on pack level. The key components are shown in figure 8.4 and specifications are summarized in table 8.4.

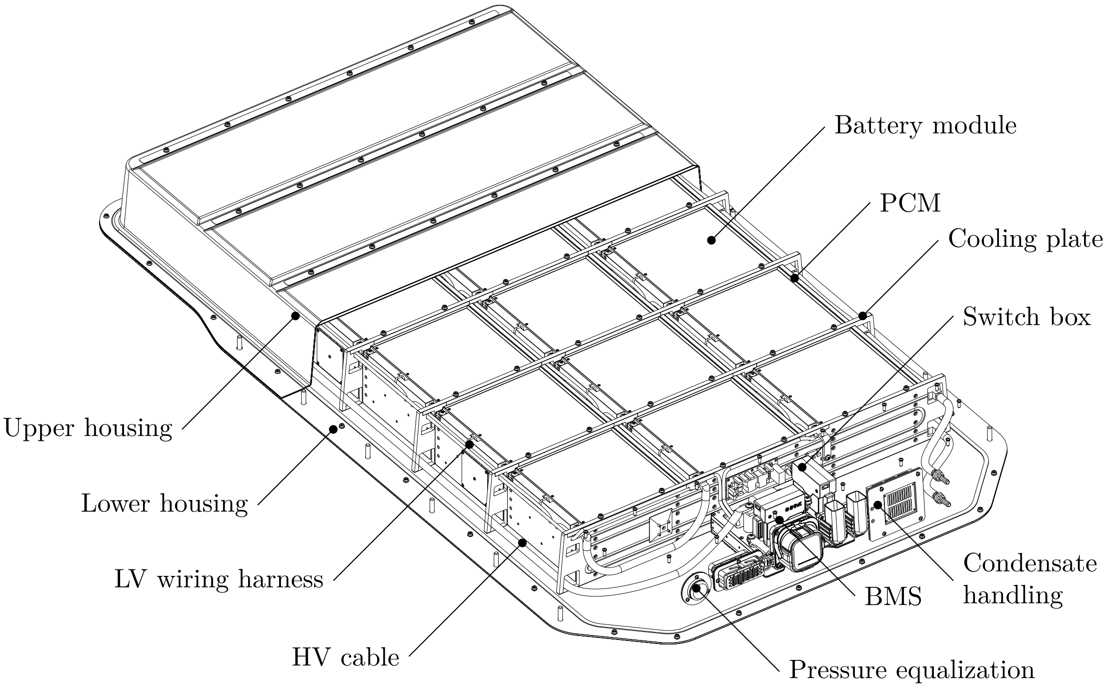

Figure 8.4: Battery pack of the electric vehicle EVA

Table 8.4: Technical data of the EVA battery pack

Nominal voltage:	400 V
Max. voltage:	450 V
Nominal energy content:	50 kWh
Overall weight:	495 kg
Overall dimensions ($\mathbf{l} \times \mathbf{w} \times \mathbf{d}$):	2,100 mm × 1,200 mm × 182 mm
Gravimetric energy density:	101 $\frac{Wh}{kg}$
Volumetric energy density:	109 $\frac{Wh}{l}$

The battery modules consist of twelve pouch type lithium-ion cells, arranged in parallel connected pairs of two cells, which share one aluminum shell. Those aluminum casings fix the soft pouch-bag cells mechanically and also provide the mounting interfaces to the cooling system and the battery housing. Six of those pairs are stacked on top of each other and connected in series, resulting in a 6s2p configuration (six series- connected and two parallel-connected cells). Electrical interface towards the neighboring modules is provided by the cell interconnection system, located in the front of the cell module. The wiring harness is connected to the cell connectors of the interconnection system to sense the differential voltages between the individual cells and also to the temperature sensors, which are centrally located in between the pouch-bag cells. The wiring harness itself is connected to the cell supervision circuit, which is mounted to the housing of the cell interconnection system. At the back of each cell stack, a holder is placed, that allows to tightly mount PCM slices to the aluminum shells. A designated clamp allows for even and adjustable surface contact.

The main components of the individual battery stacks are depicted in figure 8.5.

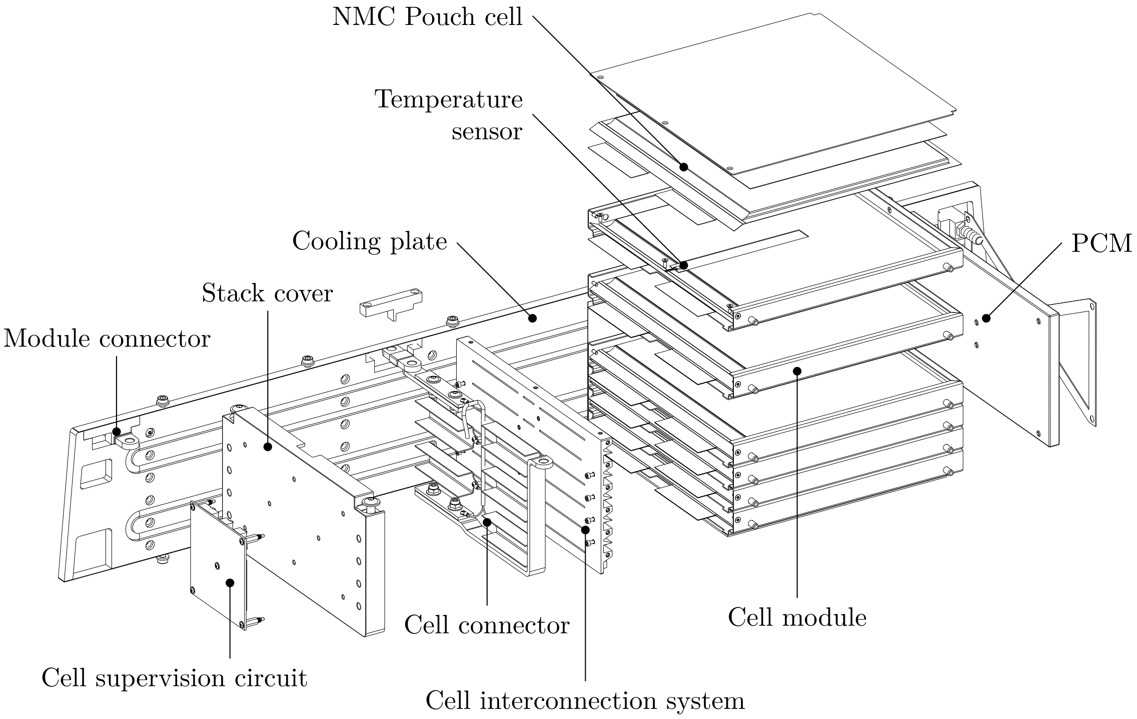
NMC Pouch cell
Temperature sensor
Cooling plate
PCM
Stack cover
Module connector
Cell module
Cell connector
Cell supervision circuit
Cell interconnection system

Figure 8.5: Battery module of the electric vehicle EVA

Simulation based layout and PCM selection

In order to prepare and dimension PCM integration, a numerical simulation model is implemented in ANSYS, serving as a tool for the design process of all case studies. With the help of the model, the selection scheme presented in 7.7 can be repeatedly passed without the need for expensive and time consuming experiments. Experimental validation can be limited to selected candidates only, that have proven to be auspicious.

According to the target application of peak mitigation, the focus lies on thermal conductivity and melting temperature as a start, before the dimensions and absolute storing capacity are defined in the following. During all iterative simulation runs, the utilization factor η_{PCM} is calculated after every time step and seen as a measure of the design variant's suitability. In order to justify the additional weight of the PCM integration, the whole latent heat storage capability should be used during every load cycle ($\eta_{PCM} \approx 1$). As temperature uniformity and mild temperature gradients are favorable, the heat flux should be constant and last over the whole charging process.

Model

For numerical simulation the battery pack geometry is simplified to contain only the main components: cells, cell connectors, cell casings, cooling plates and PCM. The resulting geometry is discretized and meshed into 230.000 tetrahedral elements. The battery cells are modeled as homogeneous material, with anisotropic material parameters according to the overview in section 3. Their heat generation is reproduced as a transient volumetric heat source, based on the data from the experimental measurement in section 7.4. PCM behavior is modeled by the heat source method described in section 6. A constant time step size of one second is used for dividing the 20 minutes fast charging phase into 1200 defined steps. The resulting model setup leads to a moderate computational time of 2.8 core hours on an Intel Core i7 workstation per transient run, which enables extensive parameter studies.

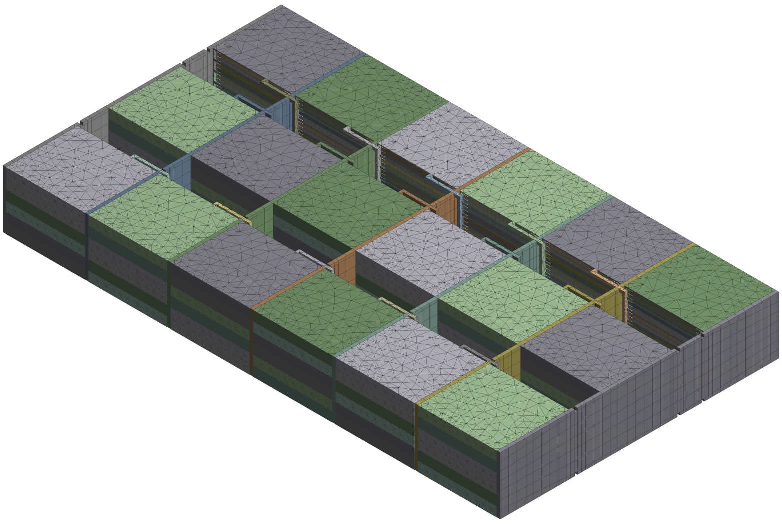

Figure 8.6: Meshed model for battery pack simulation

Design of experiment and material selection

In order to enable identification of the most promising parameter combination, discrete variants of identical total mass m_{PCM} are defined according to table 8.5 and evaluated. Average η_{PCM} over all 18 installed PCM slices, as well as minimum and maximum values, are calculated in post processing and plotted in figure 8.7.

Table 8.5: PCM candidates for integration in EVA battery pack

	(I)	**(II)**	**(III)**	**(IV)**	**(V)**	**(VI)**
	high energy PCM			high power PCM		
$\boldsymbol{T_{PCM}}$	25 °C	28 °C	32 °C	25 °C	28 °C	32 °C
$\boldsymbol{L}$	128 $\frac{kJ}{kg}$	140 $\frac{kJ}{kg}$	134 $\frac{kJ}{kg}$	81 $\frac{kJ}{kg}$	83 $\frac{kJ}{kg}$	78 $\frac{kJ}{kg}$
$\boldsymbol{V_{PCM}}$	15.12 dm^3	15.09 dm^3	14.39 dm^3	24.67 dm^3	24.19 dm^3	23.59 dm^3
$\boldsymbol{m_{PCM}}$	9.02 kg	9.08 kg	8.93 kg	9.08 kg	8.99 kg	9.22 kg
$\boldsymbol{E_{stored}}$	202 Wh	140 Wh	83 Wh	204 Wh	206 Wh	118 Wh

As expected, the different materials result in distinctive transient profiles of $\eta_{PCM}(t)$. For all three samples with moderate thermal conductivity (I-III) only a very limited fraction of the latent heat storage potential is utilized during the short charging time. As elevated melting temperatures additionally lead to a delayed beginning of latent energy storage, the amount of heat being stored within those samples is further limited down to 0.25 in case of sample (III).

Increased thermal conductivity of samples (IV) to (VI) significantly accelerates the propagation of the phase change front through the material. In this case, only the highest temperature sample (VI) does not completely melt during the charging process. At the other side, the sample melting at 25 °C has already completely undergone phase change after 15 minutes. Sample (V) shows the most even and continuous melting process, reaching $\eta_{PCM} = 1$ just right before the end of the fast charging and is hence considered as most appropriate candidate for the following steps.

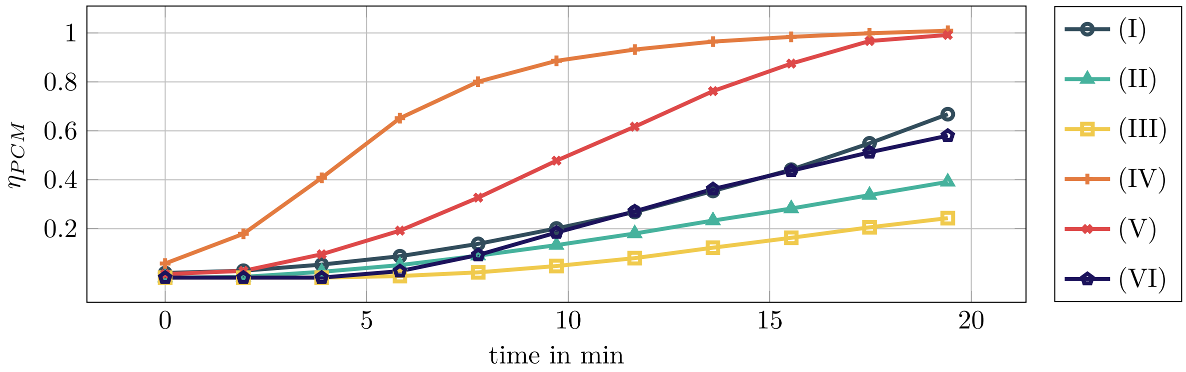

Figure 8.7: PCM utilization factor as a function of material properties

Dimensioning

The very modular design of the individual cell stacks offers the opportunity to attach different amounts of PCM without changing the overall system. In the context of the precedent simulations, PCM has always been dimensioned in a way, that theoretically allows to store a large fraction of the energy released during the current peak. However, in the following, also several configurations are investigated, that are based on a reduced amount of PCM. In these cases the PCM acts as supporting measure for active cooling. As the BTMS cooling power can be actively controlled via the three-way-valve, two different utilization modes are achievable. The PCM can support the conventional cooling system during charging or during driving. In either case, the PCM has to be recuperated during the respectively other period. As the temporarily stored energy has to be additionally dissipated, the power demand during the recuperation period increases.

Figure 8.8 highlights the effect that different sized PCM support has on the required cooling power. The three chosen variants with two operation modes each (charging/driving) and one reference without any PCM result in seven scenarios.

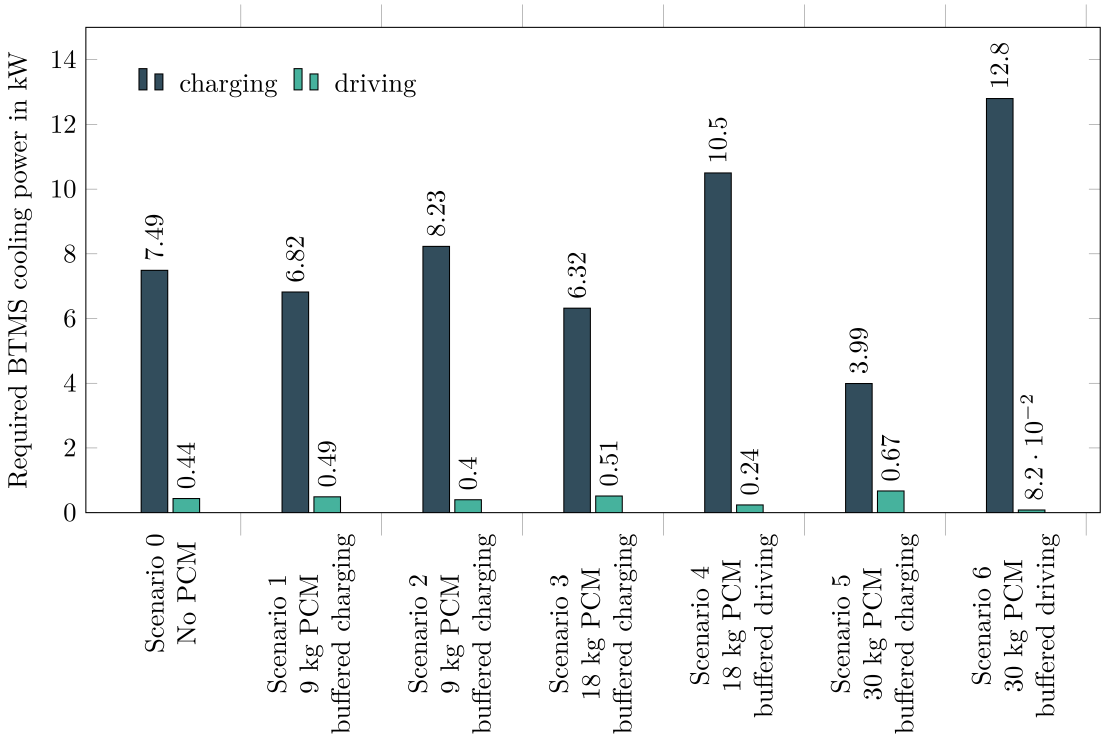

Figure 8.8: Selected PCM configurations for fast charging case study

When utilized during charging, depending on the mass of PCM, active cooling power can be reduced by up to 46 % down to 3.99 kW during this period (scenario 5). If the PCM is solidified during charging, e.g. during a regular over night charging period, and acts as buffer during driving, scenario 6 enables an almost completely passively cooled driving cycle.

Impact on driving range

However, at this point, it is important to keep in mind that the additional PCM also adds to the vehicle overall weight and hence increases the required energy for driving. To a certain extent this effect can be compensated for by the fact that additional PCM allows the downsizing of other components as compressors or pumps. For the seven scenarios presented in figure 8.8, the impact on overall vehicle weight and resulting driving range is summarized in table 8.6. Values are obtained with the help of the vehicle energy model, and reflect differences in weight as in electric consumption for the BTMS. The underlying vehicle model parameters are presented in more detail within [8].

Table 8.6: Impact of PCM scenario on cooling system and driving range

Scenario	**0**	**1**	**2**	**3**	**4**	**5**	**6**
Utilization	n.a.	🔌	🚗	🔌	🚗	🔌	🚗
PCM mass in kg	0	9	9	18	18	30	30
PCM type	-	V	V	V	V	V	V
Compressor mass in kg	8	6	9.5	5	12	5	18
Delta mass in kg	0	+7	+10.5	+16	+23	+28	+41
Range in km	**206**	**205**	**218**	**212**	**230**	**193**	**204**
Delta range in km	**0**	**-1**	+12	+6	+24	**-13**	**-2**

Results suggest that the impact on range is significantly higher, if the PCM is acting as storage during driving, with scenario 4 resulting in an 10 % increase in achievable range. However, it can also be derived that when dimensioned properly, also a buffered charging process has positive effects (as in scenario 3). What seems contradictory at first, can be explained by the fact, that the model's driving cycle includes standby times, e.g. while waiting for passengers. As for a certain fraction of those periods ambient temperature lies below 28 °C, a small portion of the PCM can be recuperated at no energetic cost. Finally, scenario 5 and 6 point at the fact that, at a certain size, energy saving can no longer make up for the additional weight, so that any material added leads to a further decrease in driving range.

Presented values are only a snap-shot for one defined use scenario and a certain battery State Of Health (SOH). They do not provide any information on temperature levels, temperature spreads and hence the impact on battery performance and aging. Even if from a solely range perspective, buffered driving seems to be advisable, over the whole life cycle buffered charging can be more rewarding if it extends the battery lifetime. The lower average temperature levels and a significantly reduced temperature peak allow the assumption that there is a positive effect on safety, performance and aging. In order to quantify this long term effects, temperature studies and aging experiments are conducted.

Experimental validation of temperature profiles

For validation of the assumptions made, two exactly identical cell stacks are assembled, whereas one stack is equipped with PCM ($T_{melt} = 28\,°C$, type V), while for the reference stack the PCM holding bracket remains empty. Both stacks are mounted in between two cooling plates, in a setup identical to the one used in the vehicle battery pack. Coolant at an inlet temperature of 14 °C is supplied by a refrigerated circulator and evenly distributed between the two samples, that are stored in a climate chamber set to 25 °C. Both samples are then undergoing the vehicle CCCV fast charging peak, while temperatures are tracked, using the six temperature sensors per stack. The resulting temperature profiles show significant differences and are opposed in figure 8.9 and table 8.7.

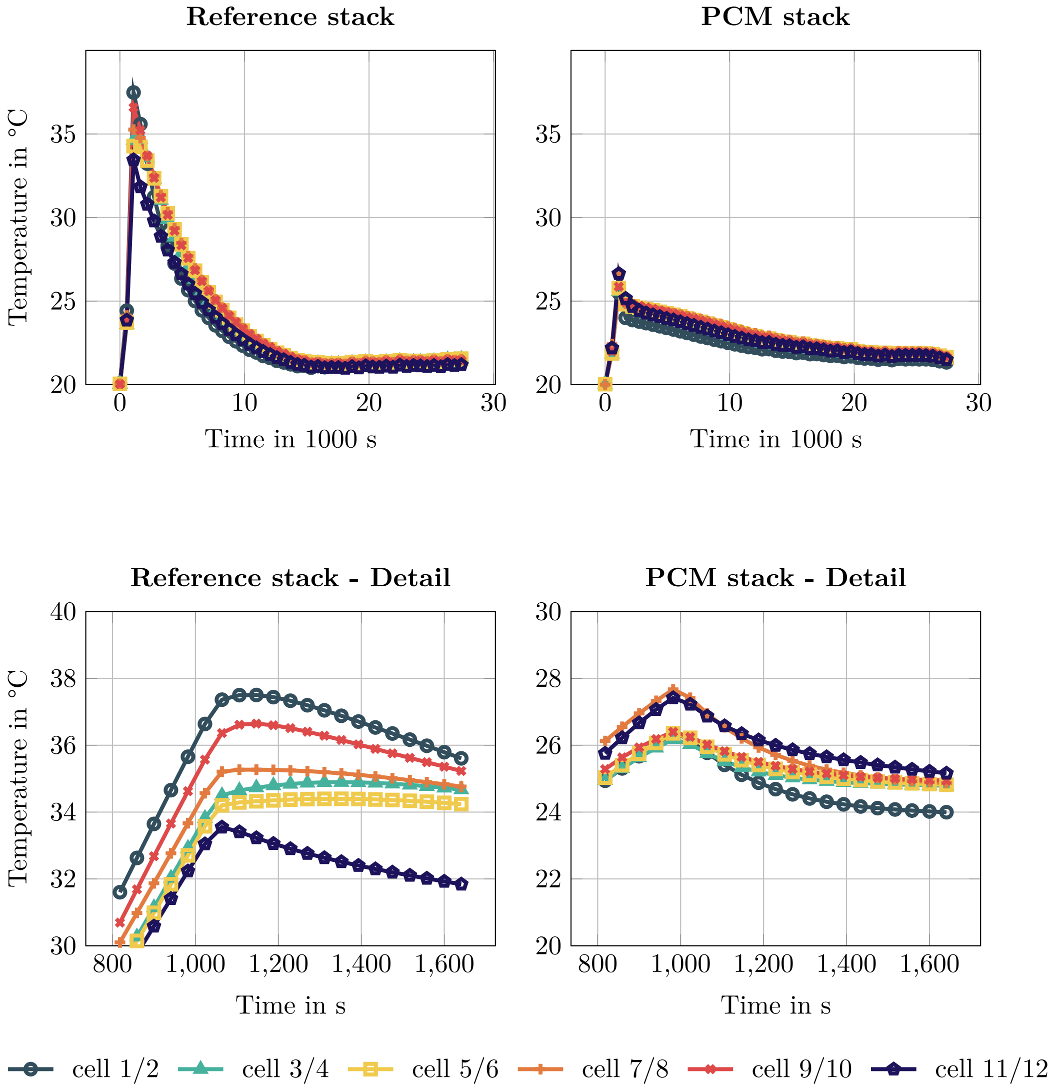

Figure 8.9: Individual cell temperatures - Reference stack vs. PCM stack

Table 8.7: Impact of PCM integration on battery stack temperature distribution

	Reference stack	**PCM stack**	**Δ**	
Temperature peak	37.5 °C	27.8 °C	**-9.7 °C**	**-25.9 %**
Max. temperature spread	5.1 °C	1.7 °C	**-3.4 °C**	**-66.7 %**
Average temperature	24.9 °C	22.1 °C	**-2.8 °C**	**-11.2 %**
Average temperature spread	1.9 °C	1.1 °C	**-0.8 °C**	**-42.1%**

The additional heat sink provided by the PCM significantly mitigates the thermal impact of the current peak, as the maximum measured temperature can be reduced by more than one quarter. Although temperature recovery after the peak is slower due to the higher thermal mass, the average temperature of the PCM equipped stack lies more than 11 % below the reference. The fact that measured temperatures remain below the nominal phase change temperature is mainly caused by two effects. The temperature sensors are located inbetween the cell terminals and not at the hottest spot of the cell. Furthermore, as figure 5.6 shows, phase change already starts at a temperature 3-5 °C below the nominal T_{melt}.

A detailed look at the peak period also clearly marks that the temperature spread within the stack is reduced and cell temperatures are virtually perfectly aligned, bringing down the maximum temperature delta from more than 5 °C to 1.7 °C. As the additional heat flux path via the PCM remains present, even beyond the phase change temperature region the positive effect on temperature uniformity remains for the whole cycle, resulting in an average temperature spread, that lies 42 % below the reference.

The combination of lower temperature level and increased uniformity highly points towards a positive effect on a more uniform aging of the individual cells, and hence a positive effect on cycle life. In order to evaluate this impact, the existing setup of two comparable stacks has been transferred to a long term aging study, resembling the actual use cycle of vehicle operation.

Aging experiments

For the following aging studies, additional battery stacks are assembled, in order to account for stochastic differences between the individual samples. In total, three reference stacks are compared to three stacks equipped with PCM. All six samples are cycled continuously with driving and fast-charging cycles and similar end-of-discharge/charge voltages of 3.2 V and 4.2 V respectively. Battery stacks are kept in climate chambers set to 25 °C. For each cycle, the amount of energy transferred during the charging step is tracked and compared to the value of the first cycle. The corresponding progression of the ratio between remaining capacity and initial capacity is interpreted as indicator for the cell aging.

Although a positive impact of PCM could have been expected, all three stacks equipped with PCM start to decay rapidly already after 250 - 300 cycles, while the reference stack shows a more foreseeable behavior. Whereas all three reference stacks range between 92 % and 95 % SOH, the other three samples have all lost 50 % of their initial capacity within less than 360 cycles and had to be removed from the test for safety reasons. Intensity and pace of the capacity loss point at sudden changes within the cell, as they typically occur during lithium plating. Post-mortem analysis of the cycled cells substantiates this hypothesis, as the surface of the cell's graphite anode features a metallic veil, which might be explained by the deposition of metallic lithium. Whereas the reference cell anode still features a dark black color, figure 8.10 highlights the metallic areas on the anode of the cell which saw the abrupt capacity loss.

One possible explanation for the effect observed might be that, due to high thermal conductivity and low melting point, cooling during the fast charging period is too effective and hence even harmful as it contradicts the natural temperature rise. In order to test this hypothesis, another three cell stacks have been assembled, utilizing a PCM of a higher melting temperature. Whereas the first batch was equipped with material melting at 28 °C, this second batch features a melting temperature of 32 °C. Confronted with the identical load pattern, these revised stacks no longer show the destructive behavior

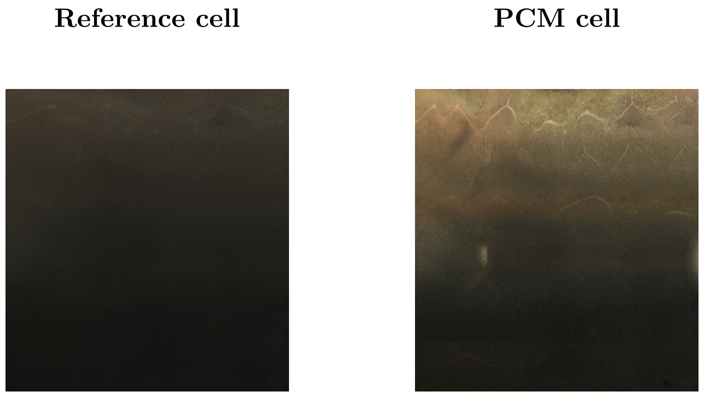

Figure 8.10: Photos of anode surfaces, comparing reference cell and abruptly aged cell

and perform similarly to the reference samples. It is assumed that the reduced heat flux from the cells, is responsible for the improvement. However, within the first 360 cycles, no positive effect on aging can be observed. The results of both experimental studies are compiled in figure 8.11.

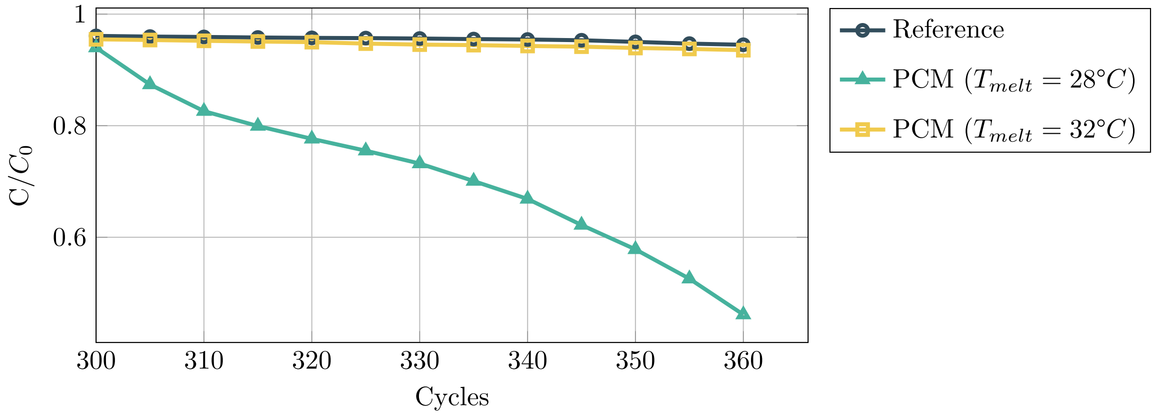

Figure 8.11: Sudden aging for PCM cooled cell stacks

Conclusion

The first case study effectively highlights the potential of passive PCM cooling, e.g. for increasing driving range. Yet, it also discloses the complexity of integrating PCMs effectively and with respect to all requirements in terms of utilization, actual benefit and long time stability. Thanks to experimental results, the proposed simulation model is confirmed to resemble the actual thermal behavior and also the design and dimensioning are expected to work according to the proposed scheme. However, the unexpected problems arising from the significant heat dissipation during fast charging leading to damaged cells, raise attention on implementation, operational aspects and the sensitivity of the overall system.

8.2 Case study: Passive cooling

A very common and well documented application of PCM for thermal management is the thermal conditioning of buildings. Different temperature levels during night and day are used to store heat and cold for later use. A similar approach is feasible for the use in Stationary Energy Storage (SES) systems. These systems benefit from the fact that layout and dimensioning is facilitated thanks to the known installation environment, predictable ambient conditions and less strict volume/weight constraints.

The layout of such a system and the impact of PCM integration on system efficiency is investigated as part of the EEBatt project, run by TUM's Munich School of Engineering. The study is conducted for a stationary storage of 200 kWh energy content operated in multiple use scenarios (amongst others: grid stabilization, primary/secondary balancing power and increase of autarchy) [163]. Inside the container more than 19.900 LFP cylindrical cells are combined in form of 104 modules. Performance parameters and the reference design of the single modular components are given in figures 8.12, 8.19, 8.20 and 8.23.

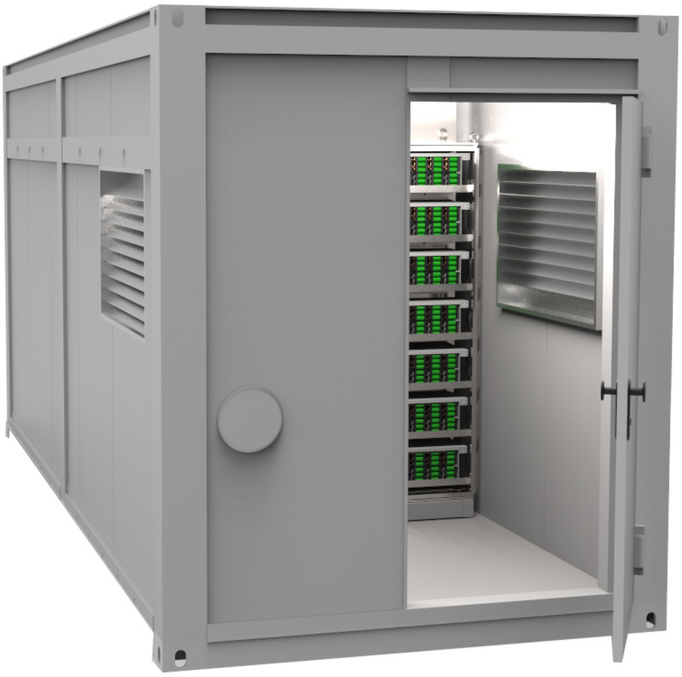

Figure 8.12: Stationary Energy Storage System - Energy Neighbor

Table 8.8: Specifications of Energy Neighbor

Overall dimensions (l × w × d):	6,000 mm × 2,900 mm × 2,400 mm
Overall mass:	approx. 9,800 kg
Energy content:	200 kWh
Peak power:	250 kW

Load profile

In the following, only the operation mode "autarchy increase" is considered, where the battery system is used to balance energy feed-in and consumption throughout the day and reduce the need for grid energy. The according storage load profile arises from the two load curves of PV feed-in and current consumption, as shown in figure 8.13 over three full days in August 2015. Data has been provided by the local network operator "Kraftwerke Haag". As during the day significantly more energy is stored than consumed, the storage is capable of covering the night's consumption, even if there is no, or only little feed-in [162].

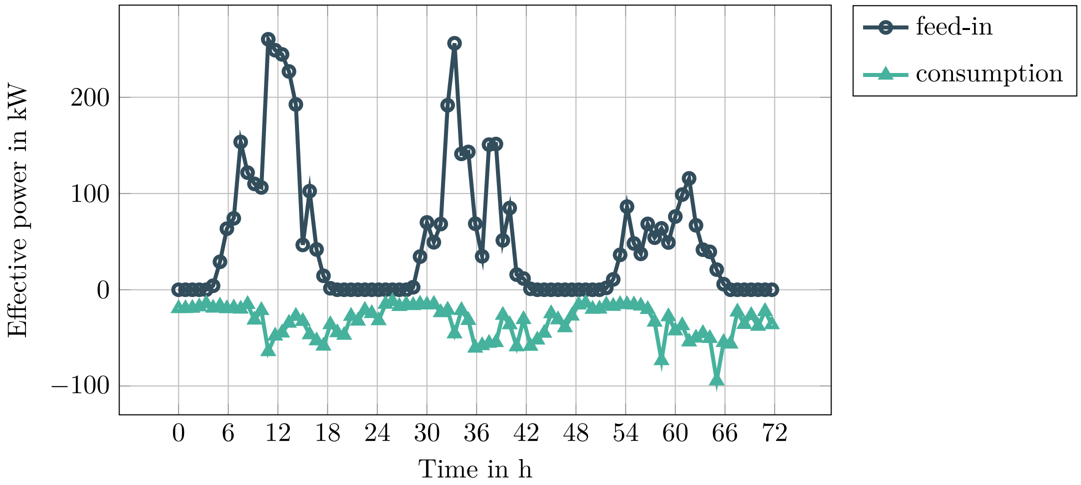

Figure 8.13: Power generation and load curve of a small village close to Munich

The resulting load curve for a single battery cell is depicted in figure 8.14. Characteristically, there are no significant peaks and the battery cells see maximum C rates of 0.5 in charging, respectively 0.2 in discharging direction, with the average idling around 0.1.

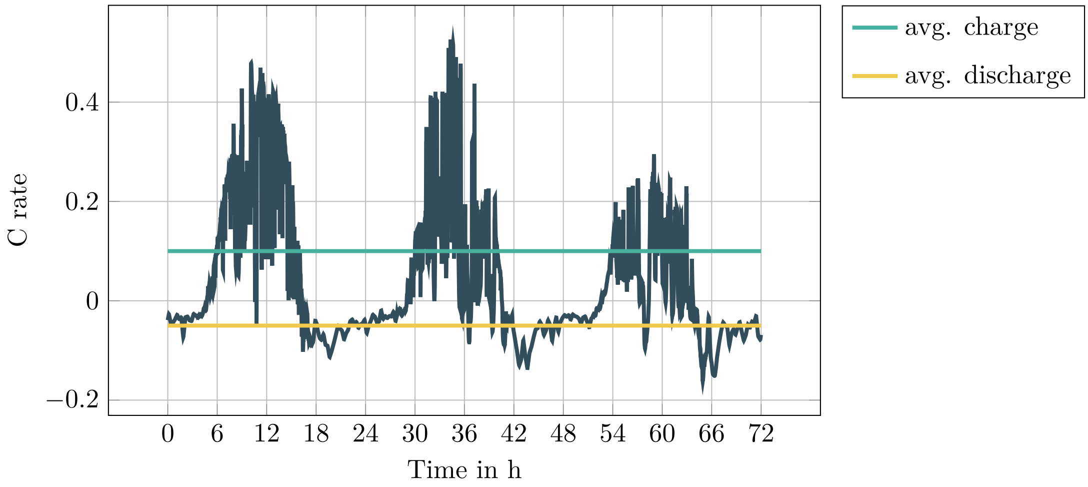

Figure 8.14: Load curves for stationary storage application

Heat generation and ambient temperature

The contour of the current profile is also reflected within the heat generation rate, measured adiabatically for a single cell during the above-mentioned three day cycle. Values are then extrapolated to resemble the entire storage system. Due to the moderate C rates, also heat release is limited and mainly occurs during the PV charging at day time. Time-averaged values per container can be assumed to be 180 W and 1.126 W for night respectively day time. The heat generation profile for the entire storage can be derived from extrapolating single cell values as given in figure 8.15.

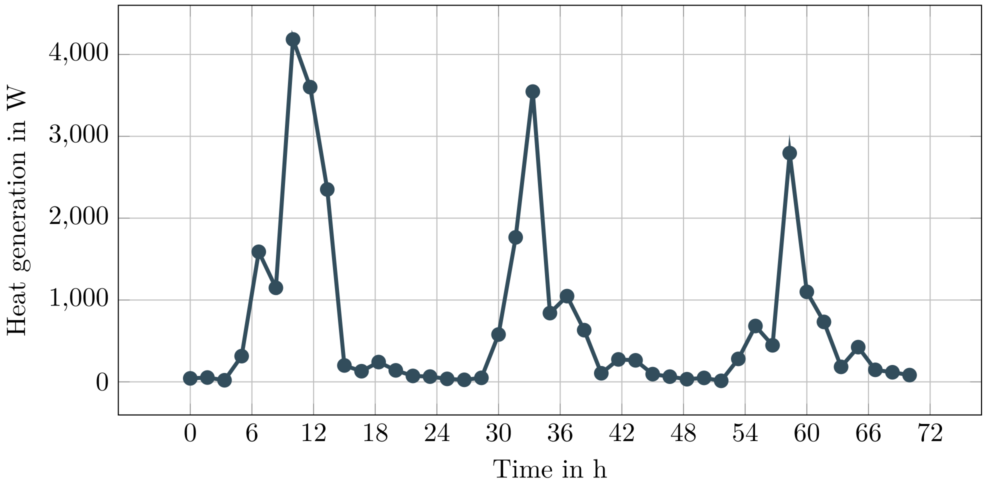

Figure 8.15: Heat generation per container resulting from the load profile shown in figure 8.14

For the selected location in Western Europe, absolute temperature levels strongly differ for the individual seasons. Minimum and maximum daily temperature values for the year 2015 are indicated in figure 8.16. However, though absolute levels are varying throughout the year, there is a distinct spread between day and night temperature of minimum 5 °C and averaging at 10 °C as figure 8.17 shows.

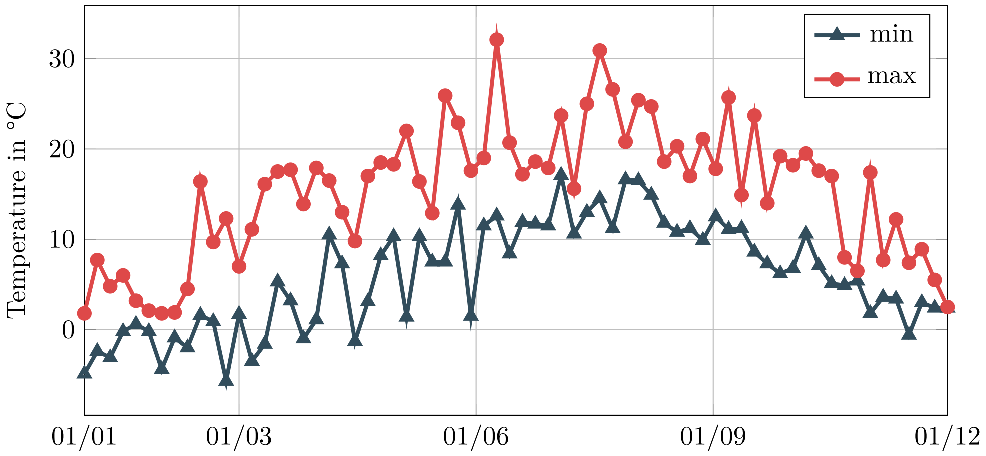

Figure 8.16: Ambient temperature range over one year [29]

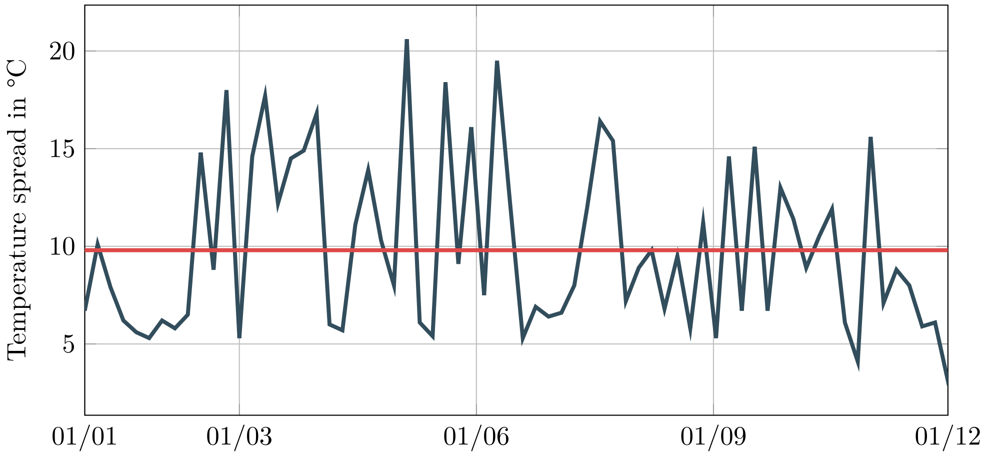

Figure 8.17: Daily temperature spread over one year [29]

Table 8.9 summarizes the monthly temperature profile and indicates the accumulated periods of time for ambient temperatures below 20 °C and above 30 °C. It can be seen that, for 90.8 % of all time, ambient temperatures lie below 20 °C and hence are low enough for PCM recuperation.

Table 8.9: Monthly temperature profile and temperature distribution for Moosham, Germany [29]

Month	**(J)**	**(F)**	**(M)**	**(A)**	**(M)**	**(J)**	**(J)**	**(A)**	**(S)**	**(O)**	**(N)**	**(D)**
T_{max} in $°C$	14.1	16.4	21.4	20.7	28.7	32.1	31.1	28.4	25.7	24.5	21.3	13.2
T_{min} in $°C$	-5.6	-6.4	-4.9	-3.6	-0.6	4.3	8.0	5.6	0.1	0.8	-0.6	-15
T_{avg} in $°C$	1.8	3.2	6.5	10.2	12.5	17.0	18.6	16.4	14.4	11.1	5.7	3.0
$T_{avg,day}$ in $°C$	2.7	5.2	9.8	13.1	15.0	20.6	21.4	18.9	16.6	13.1	6.7	3.5
$T_{avg,night}$ in $°C$	0.9	1.2	3.2	7.2	10.0	13.4	15.7	13.8	12.1	9.2	4.6	2.4
$t\,(> 30\,°C)$ in h	0	0	0	0	0	11	7	0	0	0	0	0
$t\,(< 20\,°C)$ in h	744	672	740	707	679	515	472	600	649	718	717	744

The presented load case and its boundary conditions for several reasons suggest to be suitable for a PCM based thermal management approach. There is a distinctive load pattern, that repeatedly occurs, and shows phases of alternating high and low load periods. Phases of high loads are concurrent with phases of higher ambient temperatures. Hence, a temporary storage of heat and its dissipation during colder night seems promising. This is enabled by the fact that night temperatures are well below the targeted operating temperatures, even during summer months.

Cooling concept

The reference cooling concept is based on utilizing air from outside the container, that is preconditioned (heated/cooled) depending on the ambient temperatures and the storage's state. Therefore the evaporator of a conventional stationary air conditioning unit is connected to a fan, distributing the air equally to the individual battery racks. In order to protect the cells during winter season, an electric heater is part of the air circuit. Energy efficiency is increased as the system dynamically switches fresh ambient air and recirculation.

Besides the standard air cooled approach, within this study an additional, passively cooled variant is investigated. Therefore, a PCM is added to the battery modules, completely enclosing the individual cells. The overall layout and its main components are depicted in figure 8.18. Power ratings for refrigerant loop and the air loop of the actively driven reference system are given separately for cooling and heating mode each.

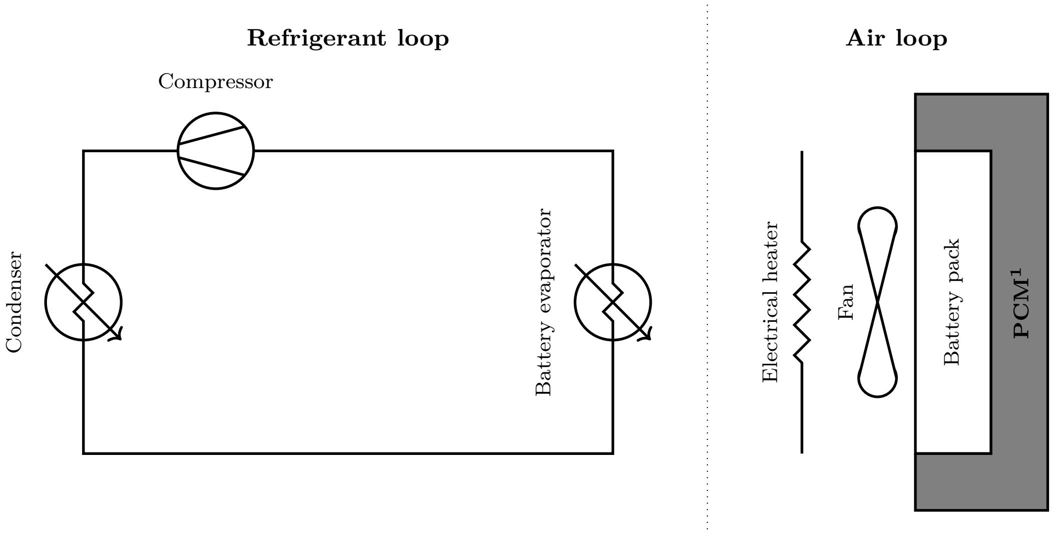

Figure 8.18: System design of Energy Neighbor cooling concept

Table 8.10: Specifications of Energy Neighbor cooling concept

	Refrigerant loop	**Air loop**
Average power requirement (cooling):[2]	800 W	150 W
Max. power requirement (cooling):[2]	4,500 W	400 W
Average. power requirement (heating):[2]	1,200 W	150 W
Max. power requirement (heating):[2]	6,000 W	400 W

---

[1] optional, only considered in simulation and small-scale experiment

[2] for reference scenario w/o PCM - Data provided by project's heating/cooling contractor

Battery system layout

The core element and largest individual unit of the stationary storage are cell racks, consisting of up to 13 single cell modules. These box-shaped modules are arranged around a centrally located cooling lance in a shelf-like layout, as depicted in figure 8.19. Within the rack, all modules are connected in series, in order to achieve the nominal system voltage of 800 V and an energy content of approx. 25 kWh. The 200 kWh storage system considered in the case study is then composed out of eight such racks.

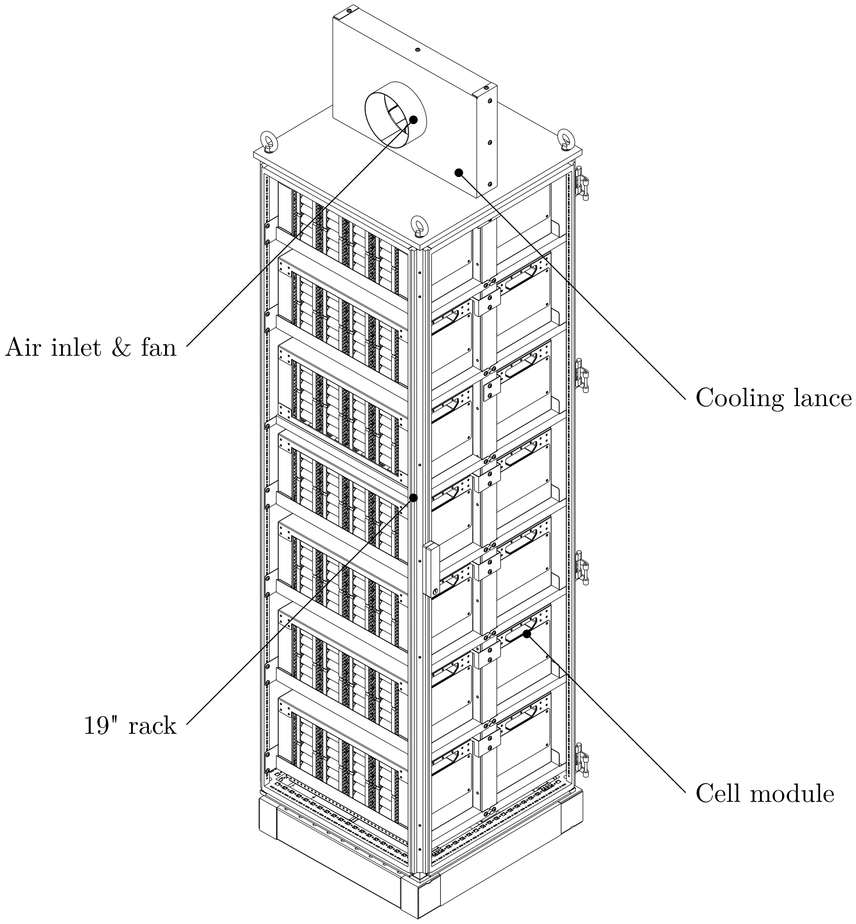

Figure 8.19: Design and core components of the stationary storage unit battery rack

Table 8.11: Technical specifications of the stationary storage unit battery rack

Overall dimensions (l × w × d):	590 mm × 590 mm × 2,400 mm
Mass:	500 kg
Energy content:	25 kWh
Nominal voltage:	800 V

The cell modules shown in 8.20 house 16 cell blocks, with 24 cells each. Furthermore, each module includes its own BMS as well as a combined power and data plug. The standardized design allows to swap modules between racks. In addition to that, the individual cell blocks within one module can also be exchanged. This enables a direct comparison between different layouts and a simple integration of PCM modules.

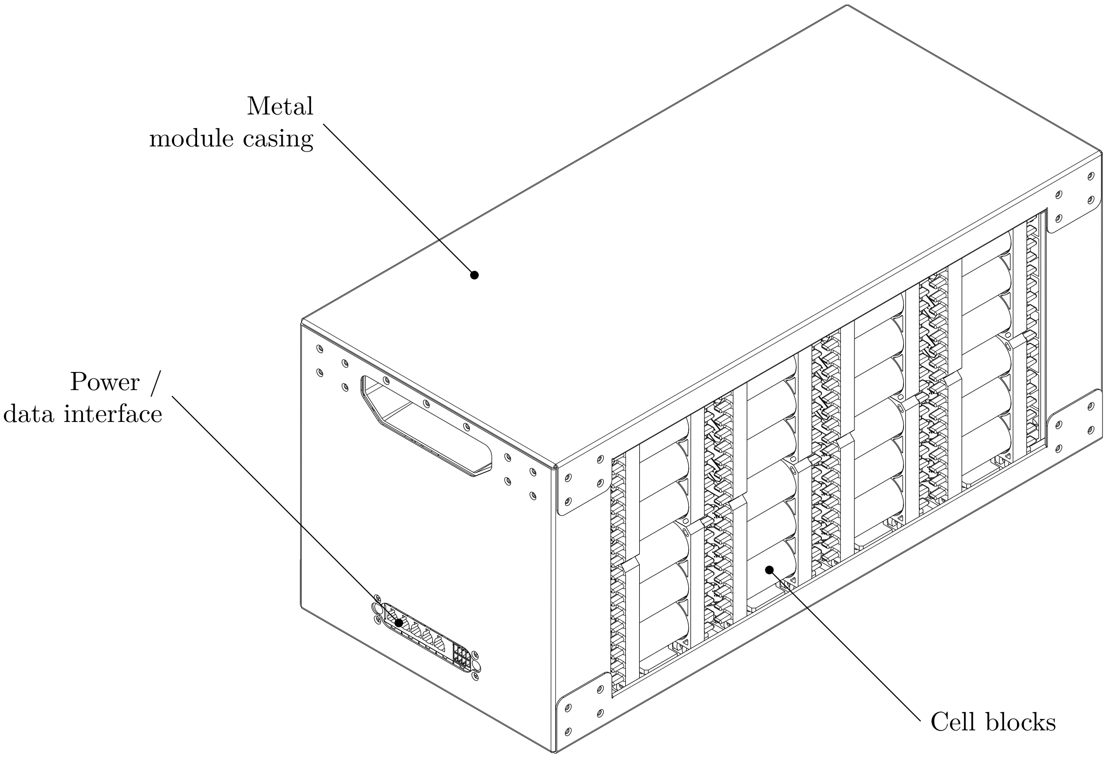

Figure 8.20: Design and core components of the stationary storage unit battery module

Table 8.12: Specifications of the stationary storage unit battery module

Overall dimensions (l × w × d):	475 mm × 215 mm × 215 mm
Overall mass:	24 kg
Energy content:	1.92 kWh
Nominal voltage:	62 V

Simulation based layout and PCM selection

As a first step towards dimensioning and designing the PCM components, the most strenuous load case has been identified. The most challenging operating conditions occur during summer days, when ambient conditions, PV feed-in powers and night temperatures reach their annual maximum values.

Hence, a 24 hour period of data, recorded in August 2015 acts as basis for the following simulations. The corresponding ambient conditions and heat generation profile for that day are given in figure 8.21.

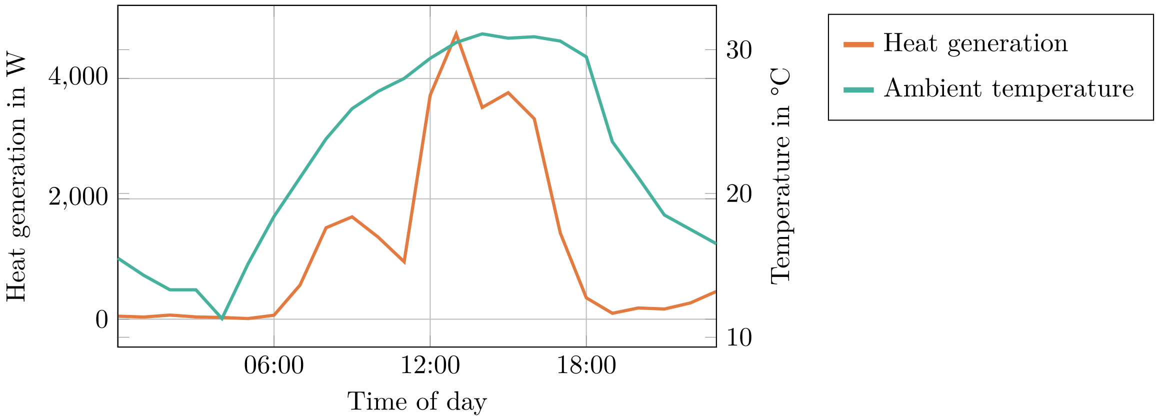

Figure 8.21: Internal and external heat load during one day of operation

As heat generation and ambient temperature both reach maximum around noon, heat energy should be stored inside the PCM during daytime, and dissipated during night, when load levels are neglectable and temperature falls way below the transition temperature.

The simulation results shown in figure 8.22 are obtained by using the transient simulation model, fed with the following model parameters and assumptions.

- The volume of PCM mounted is defined by the available space and identical in all scenarios. It sums up to approx. 17 % of the module's cell volume.
- Heat is released from the individual battery cells uniformly across their surface.
- Only the PCM candidates from table 8.13 are used.
- Timestep size is discrete, constant and set to 1 s.

Table 8.13: PCM candidates for integration in the "Energy Neighbor" stationary battery

	(I)	**(II)**	**(III)**	**(IV)**	**(V)**	**(VI)**
	high energy PCM			high power PCM		
$\boldsymbol{T_{PCM}}$	25 °C	28 °C	32 °C	25 °C	28 °C	32 °C
$\boldsymbol{L}$	132 $\frac{kJ}{kg}$	140 $\frac{kJ}{kg}$	128 $\frac{kJ}{kg}$	78 $\frac{kJ}{kg}$	83 $\frac{kJ}{kg}$	81 $\frac{kJ}{kg}$
$\boldsymbol{\lambda_\perp}$	3.8 $\frac{W}{mK}$	3.9 $\frac{W}{mK}$	3.7 $\frac{W}{mK}$	6.1 $\frac{W}{mK}$	6.0 $\frac{W}{mK}$	6.3 $\frac{W}{mK}$

From the data represented in figure 8.22 several conclusions can be drawn. For temperature regions below the phase change, all materials act solely as additional thermal mass and cause the battery temperature to react on changes more inertially. At this point, the varying composition has virtually

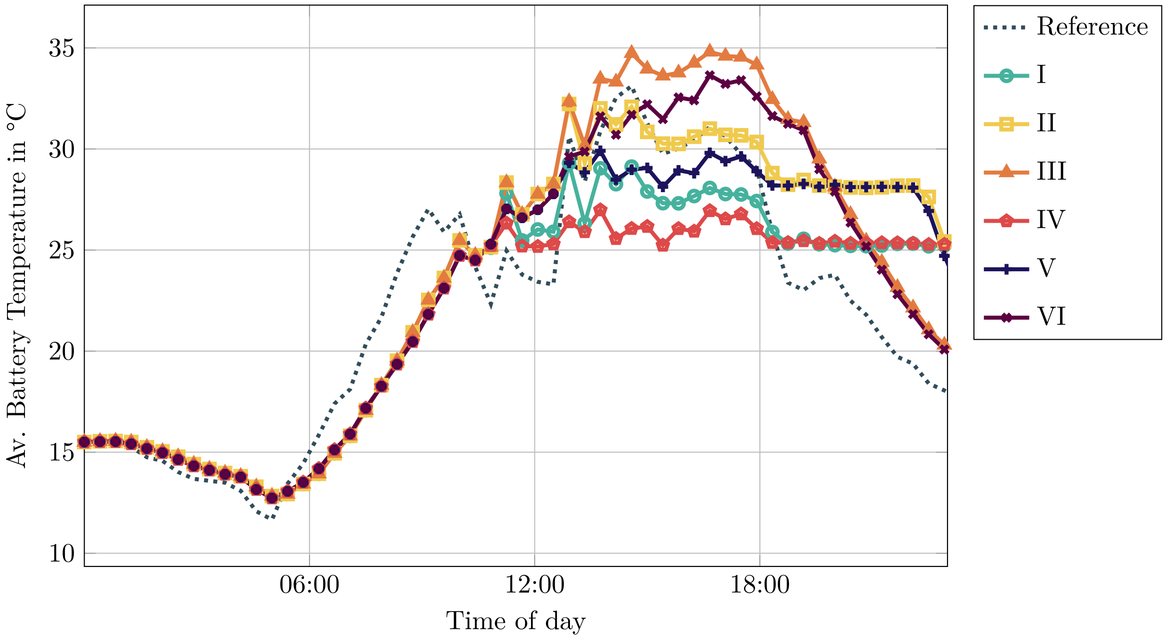

Figure 8.22: Comparison of simulated PCM variants and experimentally measured reference in terms of average battery temperature

no effect, so that all PCM temperature curves are almost congruent till the lowest phase change temperature (25 °C) is hit for the first time. In the following time steps the material samples with the lowest phase change temperature also result in the lowest battery temperature levels, whereas the 32 ° samples (III and VI) can barely influence the battery temperature level at all. Their low utilization can also be seen by the fact that there is virtually no recuperation plateau following the peak load. For all other samples, this plateau of constant temperature can be clearly identified. When comparing the high-energy samples with their more conductive high-power counterparts, the latter, without exception, result in lower battery temperatures.

The most promising passive variant (IV) reduces the maximum battery temperature level by more than 6 °C or 18 % compared to actively driven air cooling. As this type of BTMS does not consume any parasitic cooling power, it increases the overall efficiency of the storage significantly by utilizing cold, stored during the night hours. Putting the daily energy throughput in relation to the economized cooling power according to equation 8.2, the potential benefit in terms of increased efficiency can be quantified to be 21 %.

$$\Delta\eta = \frac{E_{el} - \int_{t_t1}^{t_2} E_{cool} dt}{E_{el}} \qquad (8.2)$$

Experimental validation

Experimental validation of the passive cooling concept is achieved by replacing standard air cooled cell blocks with PCM variants. In this alternative, almost the entire air volume of the standard block is filled with the graphite composite PCM introduced in section 5.3. The PCM component is manufactured from one single block, which has been supplemented by 24 drill holes for the individual cells. In order to achieve a sufficient thermal contact, the holes' diameters are chosen slightly smaller than the cell. The elastic nature of the material still allows perfect fitting and also holds the cells in place at the same time. Based on the simulation results, PCM variant IV is chosen as material. Figure 8.23 shows the layout and components of both variants of cell blocks and compares the resulting specific properties.

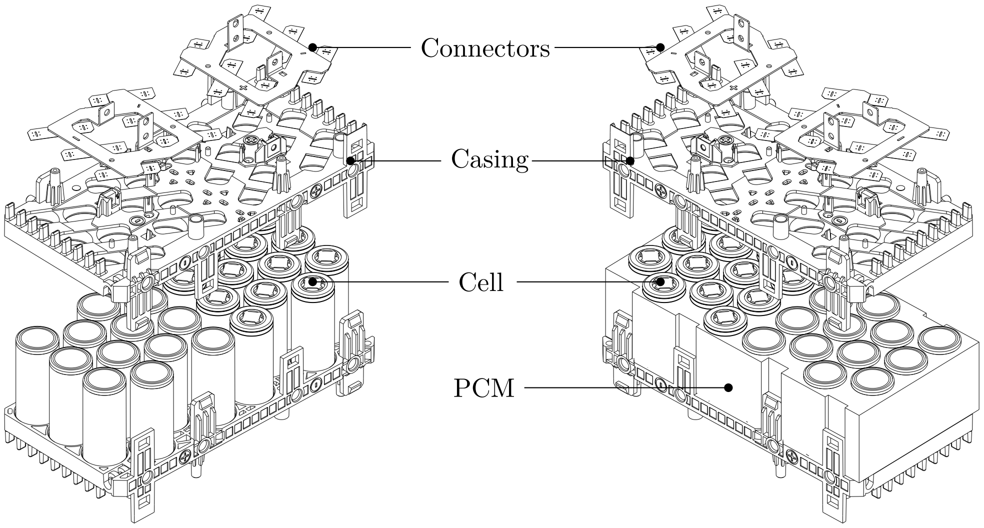

Figure 8.23: Two alternative battery box designs

Table 8.14: Specifications of reference and PCM cell block design

Air (reference)		PCM
2.46 kg	**Total weight**	3.24 kg
93.66 $\frac{Wh}{kg}$	**Specific energy**	71.11 $\frac{Wh}{kg}$

Experimental results are opposed to simulation data in figure 8.24. The course of both curves suggests that simulation resembles the fundamental processes well, however does not exactly meet the absolute temperature levels. A more detailed comparison of the results reveals that the maximum error of the simulation lies at 10.4 %, with an average error of 4.2 %. The derivation in absolute temperature level might be caused by slight variances between real and simulated thermal contact resistance values, as they highly depend on manufacturing tolerances. The fact, that temperature recuperation during experiment occurs more rapidly is pointing at an elevated heat flux to ambient, e.g. due to convective effects.

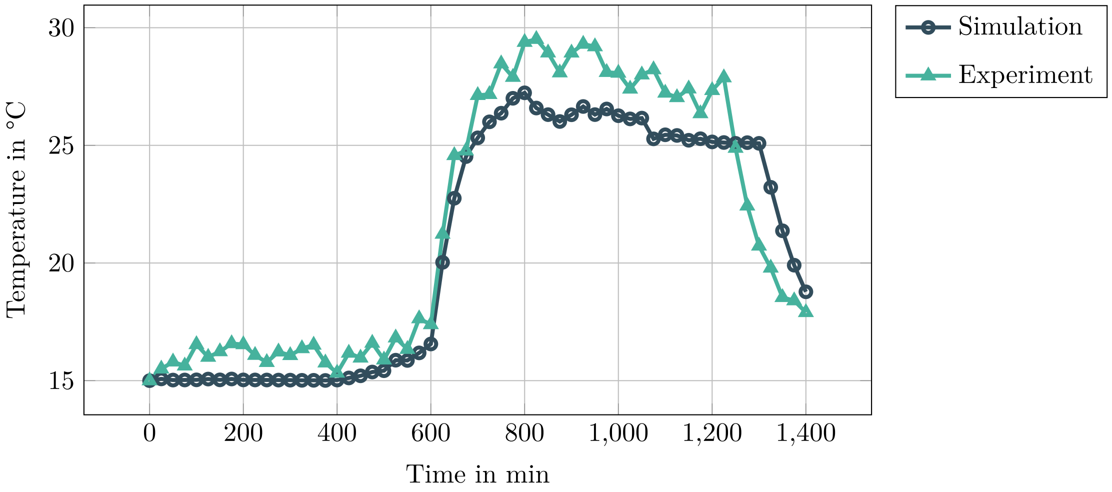

Figure 8.24: Experiment vs. simulation - PCM equipped cell blocks

Conclusion

Results obtained by combining real life application and environmental data with the developed PCM simulation models suggest that for larger scale stationary batteries, daily temperature spreads can be used to significantly reduce the amount of energy required for BTMS. In the presented case, even for a hot summer day, a completely passive cooling can be achieved, with temperature levels and spread even being more favorable than in the existing reference setup, which is actively cooled.

8.3 Case study: Prevention of thermal runaway propagation

Within the third case study, PCM's ability to decelerate or even prevent thermal runaway propagation on system level is elicited. The investigated module comprises fourteen cylindrical lithium ion 41 Ah cells of NCA chemistry arranged in two identical rows. Featuring a 2p7s configuration and a total nominal capacity of 2.1 kWh, it is commonly used in scalable stationary energy storage applications. The cell type used includes an internal safety mechanism, combining a current interruption device and a vent. All individual cells (1-14) are mounted vertically and held in place by a thin-walled split polypropylen housing (A) and an insulating polyurethan foam core (B) as depicted in Figure 8.25. Cell connectors are made of solid copper plates. The cell numbering and relevant layout parameter names will be persistently used in the following. As onset temperature and amount of energy released during thermal runaway correlate with the SOC [45] [26], prior to the following experiments, all modules have been fully charged to a SOC of 100 % in order to represent the worst case scenario.

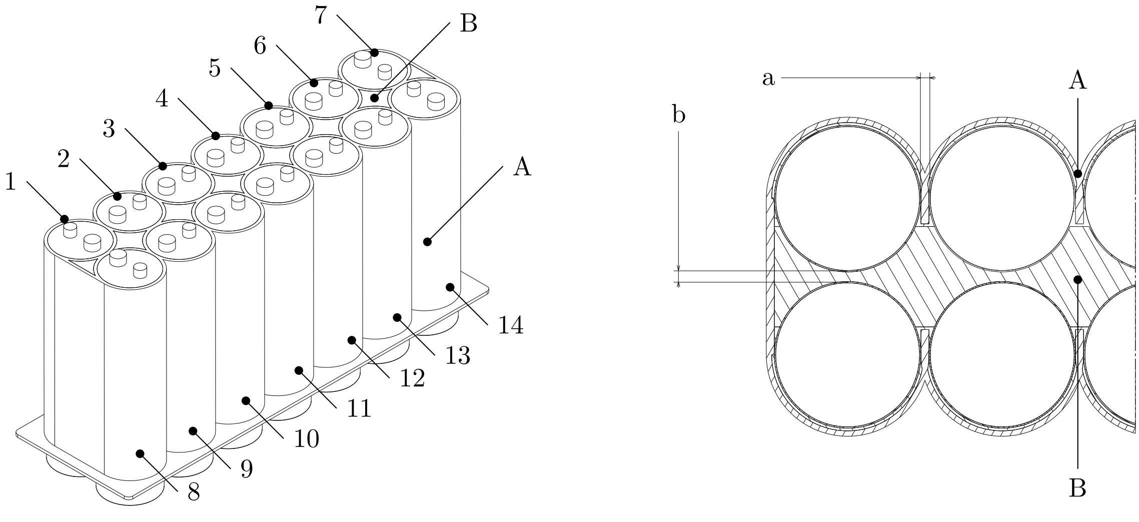

Figure 8.25: Design and main components of the investigated stationary storage module

Table 8.15: Specification of cell module

Overall dimensions (l × w × d):	400 mm × 600 mm × 2000 mm
Energy content:	2066 Wh
Nominal voltage:	25.2 V

Load profile

Starting point of the proposed numerical investigation of PCM integration has been a set of extensive real-life experiments conducted in a controlled abuse environment. Experiments have been conducted by the TÜV Süd Battery Testing GmbH. In order to identify causal coherence, twenty-two identical LIB modules have been triggered by forcing the centrally located cell 11 into thermal runaway. During eleven tests, thermal runaway has been initiated by a low ohmic external Short Circuit (SC) (below

0.3Ω). The remaining eleven modules have been triggered by controlled Overcharge (OC) of the identical cell with up to 15.0 V and currents of up to 10 C. Temperatures of all cells are logged by type K thermocouples located at the outer shell of each cell. Additional thermocouples are used to track ambient temperature and temperature at the terminals. Visual control via several cameras allows to identify and timestamp events as venting or burning. In one out of four runs, thermal runaway propagates to the adjacent cell and eventually to the whole module. Experimental results for those relevant cases are listed in table 8.16.

Table 8.16: Data recorded during TR abuse experiments

Experiment	**Trigger**	**Onset temperature**	**Max. temperature**	**Time b/w venting and TR**
1	Short circuit	139 °C	580 °C	8.6 min
2	Overcharge	137 °C	512 °C	10.3 min
3	Short circuit	139 °C	586 °C	9 min
4	Overcharge	141 °C	506 °C	8.75 min
5	Overcharge	144 °C	523 °C	6.9 min

From the recorded data, the following qualitative statements can be derived:

- The onset temperature for the triggered cells and all following cells lies within a narrow temperature range of 137 °C and 144 °C.
- Venting of the adjacent cell, in all cases, leads to thermal runaway propagation.
- Propagation follows a similar pattern, with the opposite cell being the first to be excited
- Propagation to one additional cell always leads to the loss of the whole module
- Time between venting of a cell and thermal runaway is almost identical for all ignited cells.

A typical course of recorded thermal runaway propagation is shown in figure 8.26. Especially the narrow onset temperature window, and the self-accelerating nature of the cell-to-cell propagation can be clearly identified. For cell 12, the temperature probe peeled off from the cell surface, resulting in corrupted data which is excluded from the following observations.

TR simulation model

With extensive experimental data at hand, the next step and prerequisite for the PCM investigation is a finite element model that reflects the actual module properties and behavior. For the subsequent investigations a compact, but still precise model of the battery module has been setup in ANSYS.

It is aligned with existing thermal runaway modeling approaches as [20] and [35], but has been designed with focus on supporting the additional PCM models. In order to reduce the computational costs of the model, several assumptions and simplifications have been included in the proposed simulation setup. Experimental results have shown a predictive pattern of propagation and an inevitable loss of

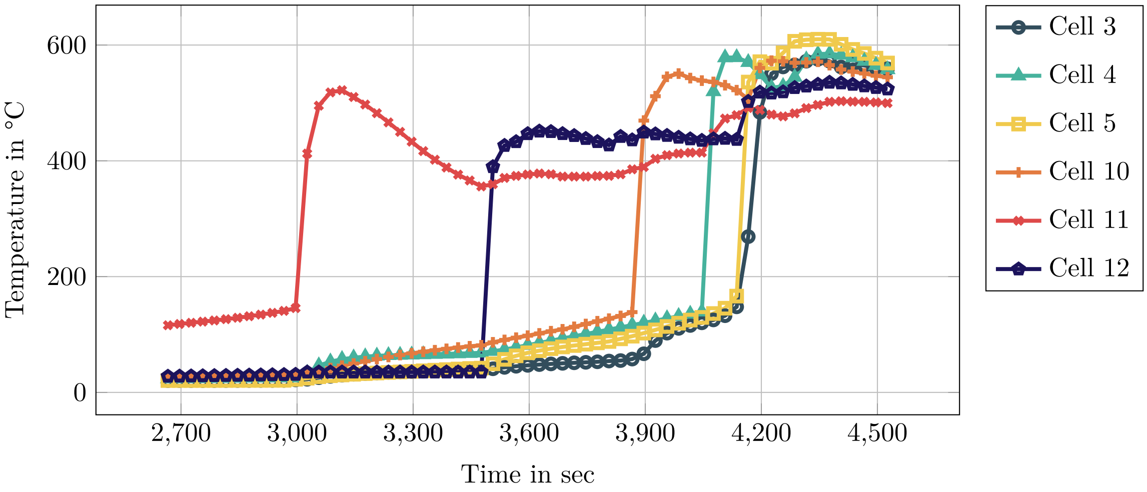

Figure 8.26: Thermal runaway propagation after short circuit of cell 6 at $t = 0s$

the module after the first passover, which was always directed towards one of the cells being in direct contact with the initially triggered one. Accordingly, only the starting cell and the directly adjacent cells are modeled. Material and process parameters are assumed to be constant throughout the model, only depending on temperature and fitted according to the experimentally obtained values, as detailed in the subsequent subsections. The same is valid for the applied thermal boundary conditions that are kept constant over time and iteratively fitted to represent the actual experimental results. Effects as thermally induced mechanical tensions and deformations have been neglected.

Thermal material properties, as heat capacity and thermal conductivity of the individual module components originate from the corresponding data sheets where available or are obtained experimentally according to the techniques presented in section 3. An overview on all material data used for the following simulations is given in table 8.17.

Table 8.17: Thermal material properties

Property (at 25 °C)	**Fixed structure**		**Spacers**	
	NCA cell	**Poly-propylen**	**Air**	**Polyurethan foam**
Density in $\frac{kg}{m^3}$	2098.0	946.0	1.184	30.23
Spec. heat capacity in $\frac{J}{kgK}$	790	1920	1005	1720
Th. cond. cross-plane in $\frac{W}{mK}$	0.985	0.22	0.026	0.038
Th. cond. in-plane in $\frac{W}{mK}$	17.2	0.22	0.026	0.038
Emissivity	-	0.97	-	-

In addition to the observations gathered in section 8.3, further oven and ARC tests on single cells have been conducted, following a basic heat, wait and search approach. Results confirm the already observed temperature range. Hence, for the numerical model a defined fixed onset temperature of 140 °C is chosen, in line with other studies on NCA cell behavior as e.g. in [45].

The volumetric heat generation rate of all triggered cells is modeled based on the transient temperature data measured on single cells by ARC. By combining the observed self heating rate of three experiments with the cell properties, an average volumetric thermal energy source term can be estimated according to equation 8.3.

$$\dot{Q}_{gen} = \frac{\partial T}{\partial t} m_{cell} \cdot c_{p,cell} \tag{8.3}$$

Resembling the actual environmental interactions of the experiments with maintainable effort, the following boundary conditions are assumed and applied to the simulation model:

- Convective heat transfer towards ambient air is modeled as simplified natural convection (equation 8.4) with an average heat transfer coefficient h of $5\frac{W}{m^2K}$ and is active at all surfaces in contact with ambient air.

$$\dot{Q}_{conv} = (T_{cell} - T_{air}) \cdot A \cdot h \tag{8.4}$$

- An additional term for thermal radiation is added according to equation 8.5, assuming the surrounding ambient area to be significantly larger than the cell area and held at constant temperature of T_{amb}. The emissivity of the outer surface ϵ_{cell} is assumed to be 0.77.

$$\dot{Q}_{rad} = \epsilon_{cell} \cdot \sigma \cdot A_{surface} \cdot \left(T_{surf}^4 - T_{amb}^4\right) \tag{8.5}$$

- As the bottom of the module is in direct contact with the testing area, a conductive heat flux of $20\frac{W}{m^2}$ between both contact surfaces is imposed.
- The thin air gap between the individual cells and the foam core is represented by a constant thermal contact resistance of $0.88 \cdot 10^{-4}\frac{m^2K}{W}$, aligned with similar material pairings found in literature [59].

The combination of all heat sources and sinks results in the overall energy balance for individual finite elements, given in equation 8.6, which is evaluated at every timestep.

$$\frac{\partial T}{\partial t} = \frac{\dot{Q}_{gen} - \dot{Q}_{conv} - \dot{Q}_{cond} - \dot{Q}_{rad}}{m \cdot c_p} \tag{8.6}$$

In order to make results of different layout variants comparable and minimize impact of numerical effects, the computational mesh is created from identical tetrahedral elements of fixed volume. This results in approximately 3000 elements for the compound of six cells. While the number of elements of the cell domain remains constant, for the surrounding structure a slight variance due to different dimensions occurs. Time discretization has also been set to fixed values, small enough to reflect the propagation mechanisms. The whole transient observation window of 1800 s has hence been separated in 3600 equally spaced timesteps. The highly non-linear propagation mechanisms are modeled with help of ANSYS User Defined Functions (UDF) which are evaluated at every single time step. Following each iteration, the average temperature values for all elements are calculated, compared with the onset temperature and written into a file. Onset temperatures are set individually for the individual cells, in order to resemble the actual behavior. In case the element's average temperature lies above the onset temperature for two subsequent timesteps, the transient heat release is triggered and the volumetric generation rate (see section 2.5) is applied to the corresponding element. From that time step on, the element follows the experimentally obtained transient heat generation curve, read from an external file. Consequently, the temperature rises in the adjacent elements, where thermal runaway is then triggered within one of the next timesteps.

Simulation results

Figure 8.27 pictures the qualitative transient process of thermal runaway propagation and a quantitative comparison with the initial experimental data. The results indicate that for the first and second cell, error is below 10 %, while it significantly increases with evolving time. This can be traced back to the effects related to the explosive and non-predictable processes as well as combustive side reactions. Chaotic and stochastic effects, as uncontrolled ejection and vaporization of material and deformation of structure can not be reproduced by the presented model. Accordingly, simulation results are only meaningful for the first propagation steps. However, as the dominating design goal is the thorough avoidance of any thermal runaway, the presenting model can still be used for further optimization activities, focusing on the first propagation step.

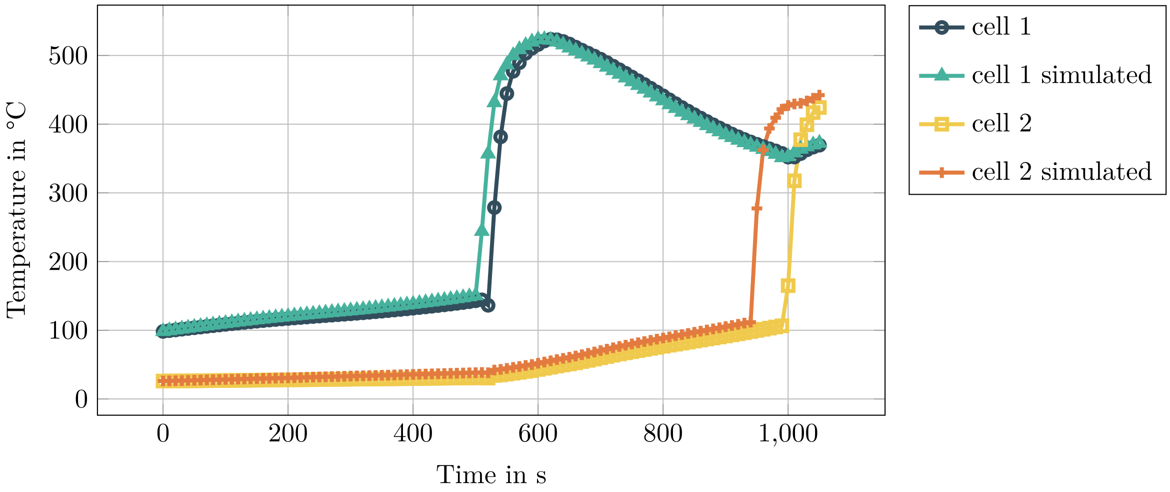

Figure 8.27: Thermal runaway propagation after short circuit of cell 6

PCM integration

With the numerical model for TR propagation in place, the beneficial impact of PCM on module level can be investigated by simulation. In line with the two previous case studies, six PCM candidates are selected. As pre-investigation in section 7.6 suggests the use of high temperature melting materials, for this study composites with a T_{melt} of 28 °C, 48 °C and 68 °C are selected. Each temperature level is represented in a high-energy and a high-power variant and an overview on all candidates is given in table 8.18.

Table 8.18: PCM candidates for TR prevention application

	(I)	**(II)**	**(III)**	**(IV)**	**(V)**	**(VI)**
	high energy			high power		
$\boldsymbol{T_{PCM}}$	28 °C	48 °C	68 °C	28 °C	48 °C	68 °C
$\boldsymbol{L}$	140 $\frac{kJ}{kg}$	132 $\frac{kJ}{kg}$	128 $\frac{kJ}{kg}$	83 $\frac{kJ}{kg}$	79 $\frac{kJ}{kg}$	71 $\frac{kJ}{kg}$
$\boldsymbol{\lambda_{\perp}}$	7 $\frac{W}{mK}$	6.8 $\frac{W}{mK}$	6.7 $\frac{W}{mK}$	21.8 $\frac{W}{mK}$	20.1 $\frac{W}{mK}$	20.4 $\frac{W}{mK}$

Figure 8.28 overlays the maximum temperature curves of the cells surrounding the triggered cell for all design variants (I to VI). Temperature of the triggered cell is given as dotted reference.

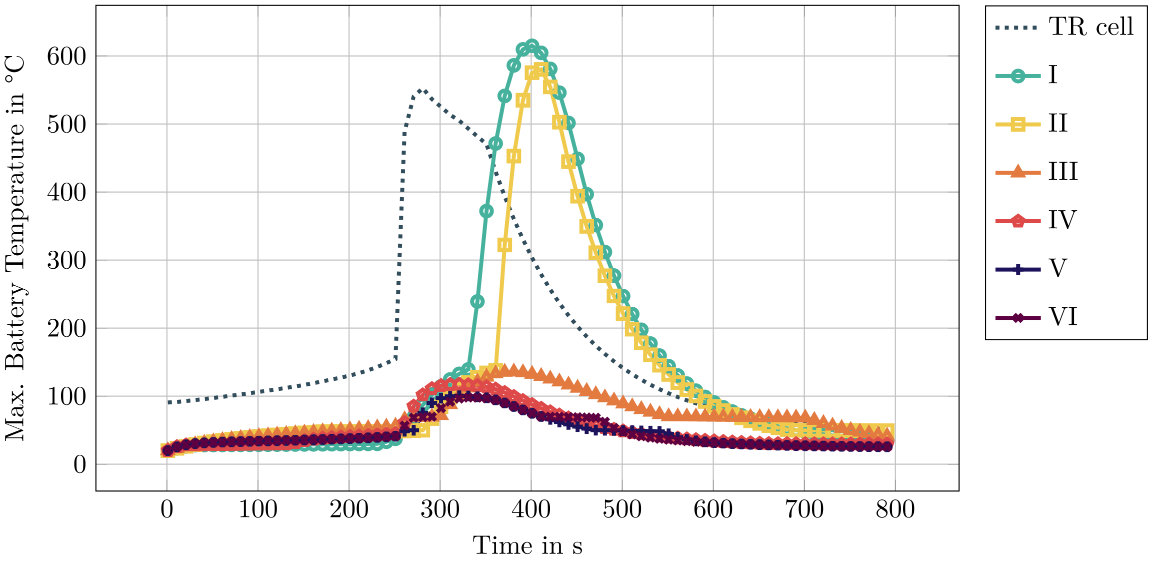

Figure 8.28: Impact of the different PCMs on max. battery temperature after TR of one cell

Result data shows that for four out of the six PCM candidates, TR propagation throughout the module can be prevented, as the maximum cell temperature of all adjacent cells remains below the onset temperature. Only for the two high-energy samples featuring lower phase change temperatures, the dissipated amount of heat is not sufficient, so that adjacent cells are triggered. The best and hence safest result is achieved by the high-performance material with the highest melting temperature (sample VI). The temperature distribution depicted in figure 8.29 shows that the material succeeds in storing some heat and distributing the remaining excess heat over the whole module more efficiently. In order to compare the positive effect of all samples, a safety margin ΔT_{safety} is defined according to equation 8.7, equaling the offset between the maximum transient temperature and the defined onset temperature. Negative values point at variants that are potentially prone to TR propagation, whereas positive values give a hint that propagation is less likely. Based on the safety margin, the occurrence probability of TR propagation can be estimated. Results of all simulated materials are compared in table 8.19, highlighting the superiority of the high-power material.

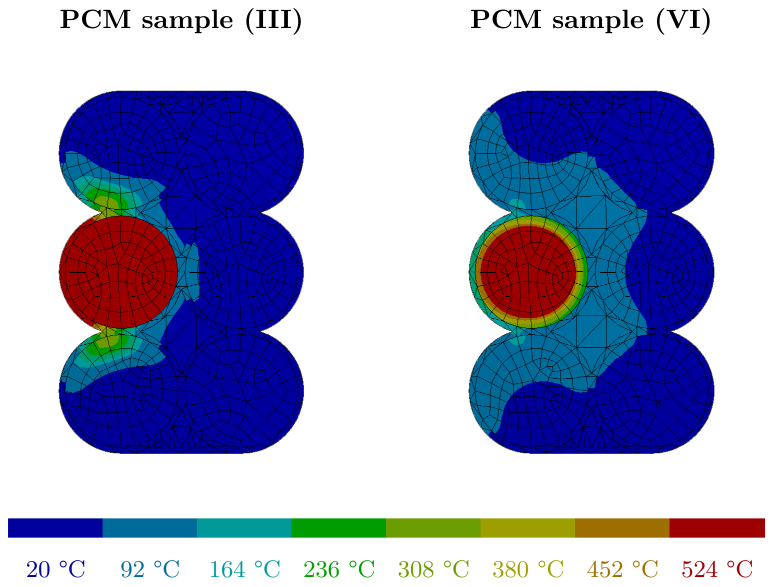

Figure 8.29: Temperature distribution at $T = T_{max}$ dependent on PCM used

$$\Delta T_{safety} = T_{TR} - max\left(T\left(t\right)\right) \quad (8.7)$$

Table 8.19: Result data of PCM impact used in TR prevention application

	(I)	**(II)**	**(III)**	**(IV)**	**(V)**	**(VI)**
	high energy			high power		
$\boldsymbol{T_{avg}}$	146.8 °C	128.5 °C	70.6 °C	50.4 °C	46.0 °C	46.1 °C
$\boldsymbol{T_{max}}$	615.2 °C	582.2 °C	135.8 °C	117.5 °C	100.6 °C	98.0 °C
$\boldsymbol{t\left(T_{max}\right)}$	398 s	406 s	377 s	318 s	321 s	334 s
$\boldsymbol{\Delta T_{safety}}$	n.a.	n.a.	4.2 °C	22.54 °C	39.4 °C	42.0 °C
$\boldsymbol{\Delta m_{PCM}}$	722 g	702 g	680 g	447 g	437 g	423 g

Conclusion

Obtained simulation results suggest that PCMs can be efficiently used as thermal buffer in order to decelerate the spread of temperature peaks between cells and hence contribute to higher resilience against thermal runaway propagation. High thermal conductivity and a high phase change temperature seem to be more decisive than the latent heat storage capacity.

9 Review and Outlook

Extensive simulations and real life tests have been conducted on the interaction between single cells (section 7), respectively whole battery systems (section 8), and various types of composite PCMs. In the following concluding section, all gathered results shall be contemplated from a statistical point of view in order to further quantify the impact of the primary design parameters and refine the design guideline of section 8.

9.1 Review of results using PCA and response surfaces

At the end of the precedent experiments and case studies, first qualitative estimations regarding the most influencial PCM design parameters have already been derived. For the three material parameters of phase change temperature, specific latent heat storage capacity and thermal conductivity, the impact on the design solution is now quantified using the statistical procedure of PCA. By the help of orthogonal transformations, dependencies between variables can be uncovered and even extensive parameter sets can be reduced to independent variables [75]. Furthermore, the impact of the individual components on single parameters, as e.g. a desired target function, can be quantified using a so called score matrix.

In a first step, dependencies between the material properties for all proposed PCMs are transferred into scatter plots, shown in figure 9.1. The three plots (a)-(c) are sufficient to depict all possible coherence between the variables.

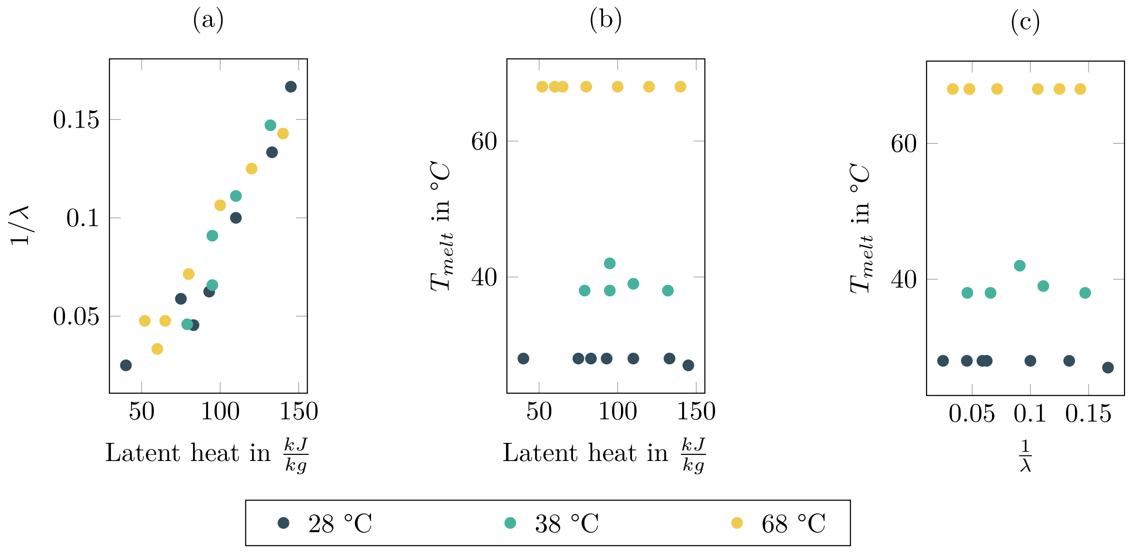

Figure 9.1: Scatter plots of all material samples measured

The results in subplot (a) confirm the very obvious fact that thermal conductivity and latent heat storage capacity of the composite material are linearly dependent variables and can be combined into one principal factor. Correspondingly, the factor thermal inertia $X_{inertia}$ is introduced according to equation 9.1. The higher the value, the more inertial the material responds to temperature changes. This step helps to reduce the complexity of the system and enables the following PCA.

$$X_{inertia} = \frac{L}{\lambda} \tag{9.1}$$

The two other scatter plots (b) and (c) clearly highlight that the thermal inertia can be adjusted virtually independently from the melting temperature, as it solely depends on the volume fraction of PCM added to the graphite carrier matrix.

Based on the two independent variables, a PCA can now be conducted for all the applications presented in the case studies. Therefore, the influence of the independent design parameters $X_{inertia}$ and T_{melt} on a figure of merit Y is quantified by weight factors as given in equation 9.2.

$$Y = \gamma_1 \cdot X_{inertia} + \gamma_2 \cdot T_{melt} \tag{9.2}$$

By plotting all obtained data after having performed extensive interpolation, simplified response surfaces can be generated with the help of software PCA toolboxes [58]. For that reason, independent variables are normalized to the given range of values. Accordingly, the shape of the response surface allows quick identification of the main sensitivities and can also be used for generating predicting models of new parameter combinations [156]. Table 9.1 gives an overview on considered parameter ranges of the individual applications.

Table 9.1: Data recorded during TR abuse experiments

	$T_{melt,min}$	$T_{melt,max}$	$X_{inertia,min}$	$X_{inertia,max}$
Peak mitigation	25 °C	32 °C	5	20
Passive cooling	25 °C	32 °C	5	20
TR prevention	28 °C	68 °C	5	20

In the following, the according response surfaces for all three case studies are explained in more detail.

Peak mitigation

In order to assess the eligibility for peak shaving (case study 1), the normalized required maximum cooling power according to equation 9.3 is utilized as figure of merit. The response surface given in figure 9.2 indicates that both melting temperature and inertia equally contribute to the resulting energy savings, with the blue areas being the most favorable ones. This fact is also reflected in the weight factors of the score matrix which only differ by 8 %. This indicates that for the dimensioning process, in the investigated parameter range, both variables virtually have the same impact. As a matter of course, however, this is only valid for temperature ranges above the idle operation temperature and within the maximum temperature.

$$Y = \Delta P_{cool} = \frac{P_{cool}}{min\,(P_{cool})} \qquad (9.3)$$

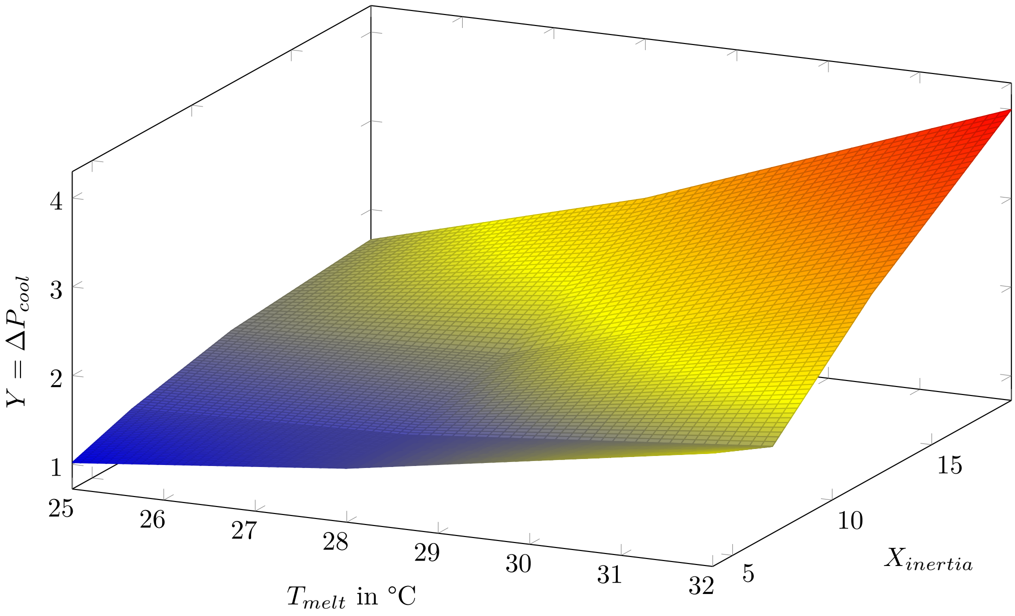

Weight factor T_{melt}:	0.52
Weight factor $X_{inertia}$:	0.48

Figure 9.2: Parameter sensitivity/response surface - use case: Peak mitigation

From an application point of view, the results signify that for an optimum design, both parameters have to be adjusted. On the other hand, it also implies that, even if one parameter is unshiftable, a change in the other one still allows significant improvements.

Passive cooling - low intensity

As an indicator of PCM's positive impact on the low load passive cooling application (case study 2), the increase in system efficiency $\Delta\eta_{sys}$ is chosen. Hence, higher values are favorable. The resulting response surface displayed in figure 9.3 features a different appearance, compared to the one presented before.

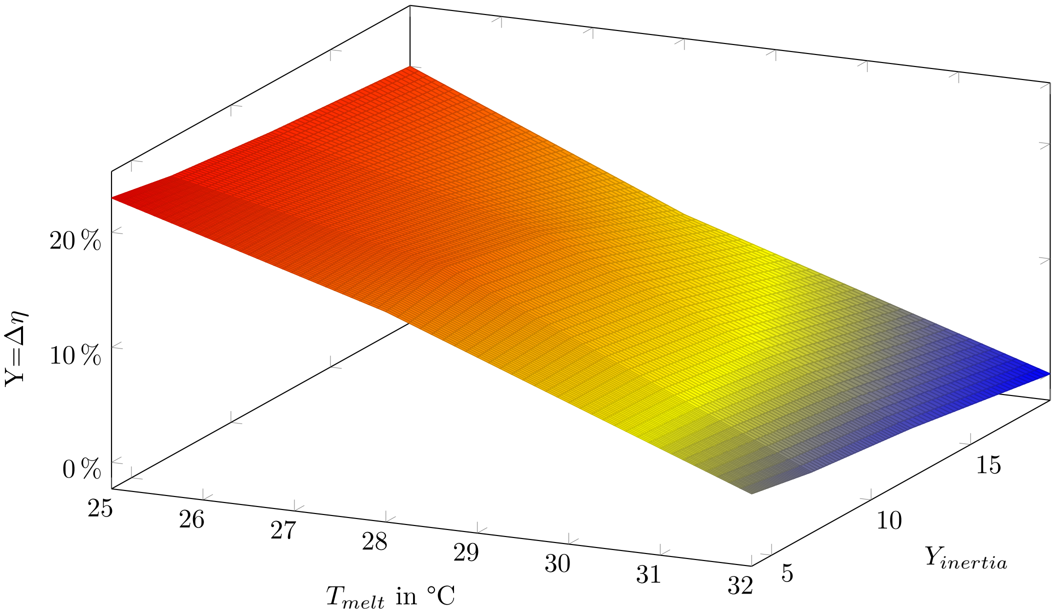

Weight factor T_{melt}:	0.78
Weight factor $X_{inertia}$:	0.22

Figure 9.3: Parameter sensitivity/response surface - use case: Passive cooling

The weight factor distribution in this case is highly shifted towards the melting temperature T_{melt}, which should be therefore the primary design criteria when dimensioning passive cooling systems. For the investigated low load use scenario, changes in PCM dynamics do not significantly affect the energy efficiency of the system. It is rather the temperature level of phase change T_{melt}, equivalent to the temperature spread between battery and PCM, that has a dominant effect. For fixed temperatures, higher system dynamics (lower system inertia) improves the efficiency only slightly.

Among the tested variants, the PCM with a melting temperature of 25 °C and lowest inertia shows the most auspicious results, promising an increase in efficiency of more than 20 %.

TR propagation prevention

In order to quantify the risk of thermal runaway propagation (case study 3), the negative reciprocal value of the safety margin, according to equation 9.4, is considered. The smaller the term gets, the more unlikely is a cell-to-cell propagation after one cell went into TR. Correspondingly, the blue areas in the response surface depicted in figure 9.4 are the parameter combinations least prone for TR propagation. Experimental data results in a weight factor distribution that is inclined towards $X_{inertia}$. The contour of the response surface suggests that also the melting temperature has certain impact, especially in the range between 30 °C and 50 °C but is superposed by the dominating effect of the material thermophysical dynamics.

$$Y = -\Delta T_{safety} \tag{9.4}$$

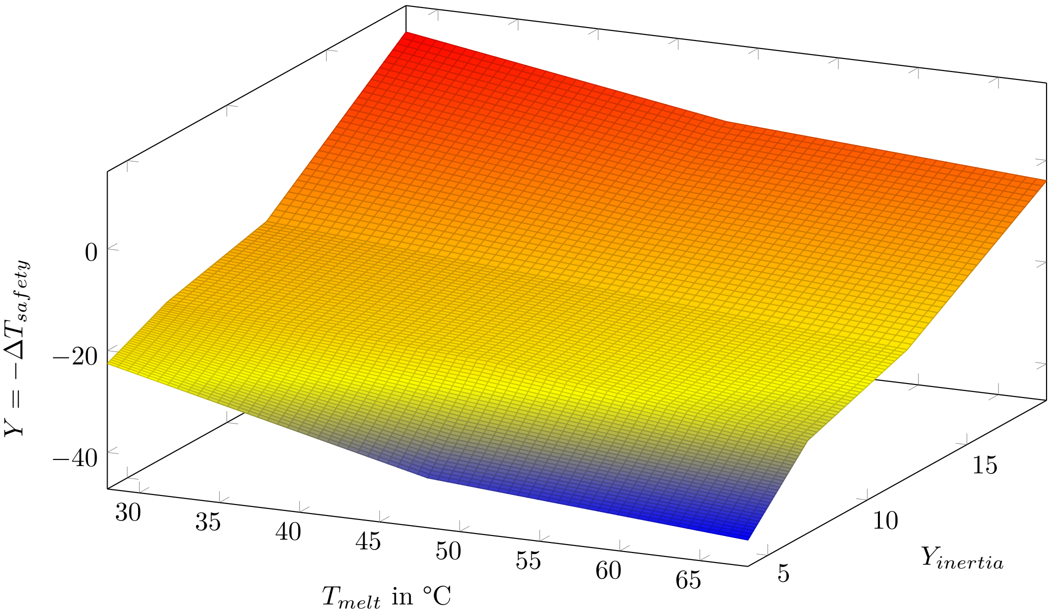

Weight factor T_{melt}:	0.13
Weight factor $X_{inertia}$:	0.87

Figure 9.4: Parameter sensitivity/repsonse surface - use case: TR propagation prevention

Results hint at the fact that for TR propagation satisfying results can only be achieved with highly conductive PCMs in between the cells that succeed in distributing the excess heat fast enough. For a given $X_{inertia}$, higher melting temperatures are advantageous.

9.2 Critical review and limitations

Although the presented experiments, simulations and case studies highlight the significant potential of PCM integration into a broad range of the most typical LIB applications, they still only represent a simplified fraction of real life use cases and are not able to cover all aspects extensively. The derived sensitivity of design parameters can, however, give valuable support for first dimensioning and fundamental design decisions. Especially the concluding sensitivity analysis proposes a resilient guideline for the question which parameter to focus on first.

However, owing the limited number of samples, qualitative observations are more authoritative than absolute figures. Due to reasons of model simplicity and limitations in experiment space, some aspects typical for real applications are only partly covered by the case studies or completely mitigated. Those effects include among others:

- Extreme or highly varying levels of ambient conditions
- Non-predictable use scenarios, e.g. long-term non-operational times
- Shifts in load-profiles, heat generation and thermal safety due to cell aging
- Variation between cells, e.g. in terms of internal resistance or onset temperature
- Interference with other system components as cell connectors, etc.
- Externally imposed temperature spreads
- Impurities or thermal contact issues
- Parasitic heatfluxes from or to the PCM

Further uncertainties arise from the simulation models, that have proven to reliably resemble actual behavior (section 6.4), but depend on settings of mesh and timestep size by nature. Experimental assessment, especially of the dynamic behavior, is complicated by the fact that the position of the phase change front within the material can hardly be measured directly, but has to be mostly derived from temperature profiles.

While the work presented only focuses on battery cooling, in further research, the same considerations shall also be undertook for heating. For this purpose and investigations on additional battery types, the developed models may serve as a starting point.

9.3 Concluding remarks and further perspective

Starting from multidimensional experimental studies on the thermal sensitivity of various LIBs, relevant temperature ranges and load profiles for potential PCM integration into battery systems have been identified. The most common actively cooled state of the art BTMS systems have been briefly introduced and compared, before focus has been put on passive thermal energy storage using composite PCMs. Based on the experimentally derived battery sensitivities, selected PCMs are investigated in more detail and evaluated in terms of their eligibility for battery applications.

Multiple numerical simulation models for describing the PCM behavior are introduced, with one advanced model being implemented for further simulation runs. Extensive single cell experiments have been carried out in order to gain deeper understanding of proper PCM selection. Those results have then been transferred to real life case studies on battery module and battery pack level to evaluate the actual potential in terms of efficiency and safety. From the entity of simulated and measured data, principle design guidelines for three main applications are derived.

The results allow to draw the following qualitative statements:

- PCMs can be efficiently utilized in battery applications for passive thermal management, increase of temperature uniformity, peak mitigation and TR propagation prevention.
- The material selection highly depends on the respective target application.
- Melting temperature and thermal inertia are the primary design levers.
- The benefits arising from PCM integration can be reliably estimated by numerical simulation.

In the context of this work a numerical simulation model that precisely resembles dynamic PCM behavior has been developed, which can be used for further investigations and shall be extended e.g. by the components mentioned in the previous section.

The variety of real life battery applications allows for further extensive research based on the findings of the presented work. Follow-up projects could be aimed at providing answers to questions as:

- How does the exact position of PCMs within the battery pack affect its effectiveness?
- To what extent is a remotely installed PCM at some point within the coolant circuit favorable over direct coupling to the battery cell?
- Is it feasible and advisable to integrate the PCM into other components of the battery system, or even within the battery cells themselves?
- Can PCM-based battery housing structures take over additional tasks, e.g. act as crash structure?

Besides those concrete questions, the developed simulation models and the PCM design guidelines can also contribute to any other project which includes BTMS tasks.

References

[1] A. Abhat. “Low temperature latent heat thermal energy storage: Heat storage materials”. In: *Solar Energy* 30.4 (1983), pp. 313–332 (cit. on p. 50).

[2] V. Alexiades. *Mathematical Modeling Of Melting And Freezing Processes.* CRC Press, Nov. 1992 (cit. on p. 63).

[3] A. Apelblat and E. Manzurola. “Volumetric and thermal properties of some aqueous electrolyte solutions”. In: *Journal of Molecular Liquids* 118.1-3 (Apr. 2005), pp. 77–88 (cit. on p. 23).

[4] A. Babapoor, M. Azizi, and G. Karimi. “Thermal management of a Li-ion battery using carbon fiber-PCM composites”. In: *Applied Thermal Engineering* 82 (May 2015), pp. 281–290.

[5] H. D. Baehr and K. Stephan. *Wärme- und Stoffübertragung.* Berlin, Heidelberg: Springer Berlin Heidelberg, 2016 (cit. on pp. 19, 20, 35).

[6] T. M. Bandhauer, S. Garimella, and T. F. Fuller. “A Critical Review of Thermal Issues in Lithium-Ion Batteries”. In: *Journal of The Electrochemical Society* 158.3 (2011), R1 (cit. on pp. 7, 11, 27).

[7] C. Barreneche, A. Solé, L. Miró, I. Martorell, A. I. Fernández, and L. F. Cabeza. “Study on differential scanning calorimetry analysis with two operation modes and organic and inorganic phase change material (PCM)”. In: *Thermochimica Acta* 553 (Feb. 2013), pp. 23–26 (cit. on p. 52).

[8] S. Bender et al. “Concept of an Electric Taxi - for Tropical Megacities”. In: *CoFAT.* 2014 (cit. on p. 90).

[9] H. Berg. “Battery technologies for electric vehicles”. In: *Batteries for Electric Vehicles.* Cambridge: Cambridge University Press, 2015, pp. 47–80 (cit. on p. 17).

[10] D. Bernardi. “A General Energy Balance for Battery Systems”. In: *Journal of The Electrochemical Society* 132.1 (1985), p. 5 (cit. on p. 27).

[11] C. R. Birkl, E. McTurk, M. R. Roberts, P. G. Bruce, and D. A. Howey. “A Parametric Open Circuit Voltage Model for Lithium Ion Batteries”. In: *Journal of The Electrochemical Society* 162.12 (2015), A2271 (cit. on p. 8).

[12] P. von Böckh and T. Wetzel. *Wärmeübertragung.* Berlin, Heidelberg: Springer Berlin Heidelberg, 2014 (cit. on p. 39).

[13] J. W. Braithwaite. “Corrosion of Lithium-Ion Battery Current Collectors”. In: *Journal of The Electrochemical Society* 146.2 (1999), p. 448 (cit. on pp. 9, 13).

[14] M. Broussely, P. Biensan, F. Bonhomme, P. Blanchard, S. Herreyre, K. Nechev, and R. J. Staniewicz. “Main aging mechanisms in Li ion batteries”. In: *Journal of Power Sources* 146.1-2 (2005), p. 90 (cit. on p. 13).

[15] T. Bruen and J. Marco. “Modelling and experimental evaluation of parallel connected lithium ion cells for an electric vehicle battery system”. In: *Journal of Power Sources* 310 (2016), p. 91 (cit. on p. 2).

[16] A. T. D. Butland and R. J. Maddison. “The specific heat of graphite: An evaluation of measurements”. In: *Journal of Nuclear Materials* 49.1 (Nov. 1973), pp. 45–56 (cit. on p. 20).

[17] L. F. Cabeza, A. Castell, C. Barreneche, A. de Gracia, and A. I. Fernández. “Materials used as PCM in thermal energy storage in buildings: A review”. In: *Renewable and Sustainable Energy Reviews* 15.3 (Apr. 2011), pp. 1675–1695 (cit. on p. 49).

[18] L. F. Cabeza, I. Martorell, L. Miró, A. I. Fernández, and C. Barreneche. “Introduction to thermal energy storage (TES) systems”. In: *Advances in Thermal Energy Storage Systems.* Elsevier, 2015, pp. 1–28 (cit. on p. 45).

[19] A. Celzard, S. Schneider, and J. F. Marêché. “Densification of expanded graphite”. In: *Carbon* 40.12 (2002), pp. 2185–2191 (cit. on p. 56).

[20] M. Chen, Q. Sun, Y. Li, K. Wu, B. Liu, P. Peng, and Q. Wang. “A Thermal Runaway Simulation on a Lithium Titanate Battery and the Battery Module”. In: *Energies* 8.1 (Jan. 2015), pp. 490–500 (cit. on p. 106).

[21] S. C. Chen, C. C. Wan, and Y. Y. Wang. “Thermal analysis of lithium-ion batteries”. In: *Journal of Power Sources* 140.1 (Jan. 2005), pp. 111–124 (cit. on p. 20).

[22] F. Cverna, ed. *ASM Ready Reference: Thermal properties of metals.* ASM International, 2003 (cit. on p. 23).

[23] G. Diarce, Á. Campos-Celador, K. Martin, A. Urresti, A. Garcı’a-Romero, and J. M. Sala. “A comparative study of the CFD modeling of a ventilated active façade including phase change materials”. In: *Applied Energy* 126 (Aug. 2014), pp. 307–317 (cit. on p. 64).

[24] M. M. Doeff. “Batteries: Overview of Battery Cathodes”. In: *Springer Encyclopedia of Sustainability Sciecne and Technology.* Berlin/Heidelberg: Springer-Verlag, 2011 (cit. on p. 20).

[25] M. M. Doeff. “Battery Cathodes”. In: *Batteries for Sustainability.* New York, NY: Springer New York, Nov. 2012, pp. 5–49 (cit. on p. 20).

[26] D. H. Doughty and E. P. Roth. “A General Discussion of Li Ion Battery Safety”. In: *Interface magazine* 21.2 (Jan. 2012), pp. 37–44 (cit. on p. 105).

[27] D. H. Doughty, E. P. Roth, C. C. Crafts, G. Nagasubramanian, G. Henriksen, and K. Amine. “Effects of additives on thermal stability of Li ion cells”. In: *Journal of Power Sources* 146.1-2 (Aug. 2005), pp. 116–120 (cit. on p. 16).

[28] X. Duan and G. F. Naterer. “Heat transfer in phase change materials for thermal management of electric vehicle battery modules”. In: *International Journal of Heat and Mass Transfer* 53.23-24 (Nov. 2010), pp. 5176–5182.

[29] *DWD Archiv Stundenwerte, Deutschland 2015.* URL: `http://www.dwd.de/DE/leistungen/klimadatendeutschland/klarchivstunden.html?nn=16102` (cit. on pp. 96, 97).

[30] T. a. E. *Electric Vehicles in Europe - 2016.* Tech. rep. Oct. 2016 (cit. on p. 38).

[31] K. Eberman, P. Gomadam, G. Jain, and E. Scott. “Material and Design Options for Avoiding Lithium Plating during Charging”. In: *216th ECS Meeting.* ECS, 2010, pp. 47–58 (cit. on p. 15).

[32] S. Emeis. “The discovery of latent heat 250 years ago”. In: *Meteorologische Zeitschrift* 13.4 (Sept. 2004), pp. 329–333 (cit. on p. 45).

[33] D. C. Erb, I. M. Ehrenberg, S. E. Sarma, and E. Carlson. “Effects of cell geometry on thermal management in air-cooled battery packs”. In: *2015 IEEE Transportation Electrification Conference and Expo (ITEC).* IEEE, 2015, pp. 1–6 (cit. on p. 34).

[34] E. C. Evarts. “Lithium batteries: To the limits of lithium”. In: *Nature* 526.7575 (2015), S93 (cit. on p. 2).

[35] X. Feng, J. Sun, M. Ouyang, F. Wang, X. He, L. Lu, and H. Peng. “Characterization of penetration induced thermal runaway propagation process within a large format lithium ion battery module”. In: *Journal of Power Sources* 275 (Feb. 2015), pp. 261–273 (cit. on p. 106).

[36] M. Fleckenstein, O. Bohlen, M. A. Roscher, and B. Bäker. “Current density and state of charge inhomogeneities in Li-ion battery cells with LiFePO4 as cathode material due to temperature gradients”. In: *Journal of Power Sources* 196.10 (May 2011), pp. 4769–4778 (cit. on p. 7).

[37] S. Furbo. “Using water for heat storage in thermal energy storage (TES) systems”. In: *Advances in Thermal Energy Storage Systems*. Elsevier, 2015, pp. 31–47 (cit. on p. 45).

[38] P. Gabbott. “A Practical Introduction to Differential Scanning Calorimetry”. In: *Principles and Applications of Thermal Analysis*. Oxford, UK: Blackwell Publishing Ltd, Jan. 2008, pp. 1–50 (cit. on p. 52).

[39] P. Gantenbein and C. Rindt. *Modeling techniques of TCM/PCM-materials on micro-, meso- and macro scales*. Tech. rep. IEA Solar Heating and Cooling Programme, Task 42, Apr. 2011 (cit. on p. 65).

[40] H. P. Garg, S. C. Mullick, and A. K. Bhargava. “Sensible Heat Storage”. In: *Solar Thermal Energy Storage*. Dordrecht: Springer Netherlands, 1985, pp. 82–153 (cit. on p. 44).

[41] S. K. Ghosh. *Functional Coatings and Microencapsulation: A General Perspective*. 2006 (cit. on p. 55).

[42] L. Gireaud, S. Grugeon, S. Laruelle, B. Yrieix, and J. M. Tarascon. “Lithium metal stripping/-plating mechanisms studies: A metallurgical approach”. In: *Electrochemistry Communications* 8.10 (Oct. 2006), pp. 1639–1649 (cit. on p. 15).

[43] J. Giro-Paloma, M. Martı’nez, L. F. Cabeza, and A. I. Fernández. “Types, methods, techniques, and applications for microencapsulated phase change materials (MPCM): A review”. In: *Renewable and Sustainable Energy Reviews* 53 (Jan. 2016), p. 1059 (cit. on p. 55).

[44] A. W. Golubkov, D. Fuchs, J. Wagner, H. Wiltsche, C. Stangl, G. Fauler, G. Voitic, A. Thaler, and V. Hacker. “Thermal-runaway experiments on consumer Li-ion batteries with metal-oxide and olivin-type cathodes”. In: *RSC Adv.* 4.7 (2014), pp. 3633–3642 (cit. on p. 16).

[45] A. W. Golubkov, S. Scheikl, R. Planteu, G. Voitic, H. Wiltsche, C. Stangl, G. Fauler, A. Thaler, and V. Hacker. “Thermal runaway of commercial 18650 Li-ion batteries with LFP and NCA cathodes – impact of state of charge and overcharge”. In: *RSC Adv.* 5.70 (2015), pp. 57171–57186 (cit. on pp. 105, 107).

[46] P. Gotcu and H. J. Seifert. “Thermophysical properties of LiCoO 2–LiMn 2O 4blended electrode materials for Li-ion batteries”. In: *Phys. Chem. Chem. Phys.* 18.15 (2016), pp. 10550–10562 (cit. on pp. 20, 23).

[47] A. Greco, X. Jiang, and D. Cao. “An investigation of lithium-ion battery thermal management using paraffin/porous-graphite-matrix composite”. In: *Journal of Power Sources* 278 (2015), p. 50 (cit. on p. 69).

[48] W. Gu, Z. Sun, X. Wei, and H. Dai. “A Capacity Fading Model of Lithium-Ion Battery Cycle Life Based on the Kinetics of Side Reactions for Electric Vehicle Applications”. In: *Electrochimica Acta* 133 (2014), p. 107 (cit. on p. 13).

[49] E. Günther, T. Schmid, H. Mehling, S. Hiebler, and L. Huang. “Subcooling in hexadecane emulsions”. In: *International Journal of Refrigeration* 33.8 (Dec. 2010), pp. 1605–1611 (cit. on p. 51).

[50] E. Günther, L. Huang, H. Mehling, and C. Dötsch. “Subcooling in PCM emulsions – Part 2: Interpretation in terms of nucleation theory”. In: *Thermochimica Acta* 522.1-2 (Aug. 2011), pp. 199–204 (cit. on p. 51).

[51] Y. Guo. “SAFETY | Thermal Runaway”. In: *Encyclopedia of Electrochemical Power Sources*. Elsevier, 2009, pp. 241–253 (cit. on p. 16).

[52] S. E. Gustafsson. “On the Development of the Hot Strip, Hot Disc, and Pulse Hot Strip Methods for Measuring Thermal Transport Properties”. In: (2015) (cit. on p. 25).

[53] S. Al-Hallaj, H. Maleki, J. S. Hong, and J. R. Selman. “Thermal modeling and design considerations of lithium-ion batteries”. In: *Journal of Power Sources* 83.1-2 (Oct. 1999), pp. 1–8 (cit. on pp. 1, 31).

[54] S. Al-Hallaj and J. R. Selman. “Thermal modeling of secondary lithium batteries for electric vehicle/hybrid electric vehicle applications”. In: *Journal of Power Sources* 110.2 (Aug. 2002), pp. 341–348 (cit. on p. 71).

[55] Y. He. “Rapid thermal conductivity measurement with a hot disk sensor”. In: *Thermochimica Acta* 436.1-2 (2005), p. 122 (cit. on p. 26).

[56] D. I. T. Heckenberger, D. I. A. Wiebelt, and D. r. n. D. Neumeister. “Integration of a lithium-ion battery into hybrid and elelectric vehicles”. In: *ATZ worldwide* 112.4 (2010) (cit. on pp. 33, 38).

[57] T. Heckenberger, C. Pfender, T. Isermeyer, and F. Brotz. “Cooling of high-performance batteries for hybrid vehicles”. In: *ATZ worldwide* 109.12 (2007) (cit. on p. 34).

[58] T. H. Hejazi, A. Salmasnia, and M. Bastan. “Optimization of Correlated Multiple Response Surfaces with Stochastic Covariate”. In: *International Journal of Computer Theory and Engineering* (2013), pp. 341–345 (cit. on p. 114).

[59] H. Herwig. *Wärmeübertragung A-Z*. Springer Verlag, 2000 (cit. on p. 108).

[60] G. W. H. Höhne, W. Hemminger, and H. J. Flammersheim. “Introduction”. In: *Differential Scanning Calorimetry*. Berlin, Heidelberg: Springer Berlin Heidelberg, 1996, pp. 1–6 (cit. on p. 52).

[61] A. F. Holleman, E. und Nils Wiberg, and G. Fischer. *Lehrbuch der Anorganischen Chemie*. Berlin • New York: Walter de Gruyter, 2007 (cit. on p. 50).

[62] H. Hu and S. A. Argyropoulos. “Mathematical modelling of solidification and melting: a review”. In: *Modelling and Simulation in Materials Science and Engineering* 4.4 (Jan. 1999), pp. 371–396 (cit. on p. 64).

[63] L. Huang, E. Günther, C. Doetsch, and H. Mehling. “Subcooling in PCM emulsions—Part 1: Experimental”. In: *Thermochimica Acta* 509.1-2 (Sept. 2010), pp. 93–99 (cit. on p. 51).

[64] C. Huber and R. Kuhn. “Thermal management of batteries for electric vehicles”. In: *Advances in Battery Technologies for Electric Vehicles*. Elsevier, 2015, pp. 327–358 (cit. on p. 38).

[65] C. Huber and A. Jossen. “Development of a holistic thermal management concept for an ultra-fast charging EV in tropical climate”. In: *rd International Conference on Thermal Management for Electric Vehicles*. June 2013 (cit. on p. 84).

[66] A. Jamekhorshid, S. M. Sadrameli, and M. Farid. “A review of microencapsulation methods of phase change materials (PCMs) as a thermal energy storage (TES) medium”. In: *Renewable and Sustainable Energy Reviews* 31 (Mar. 2014), pp. 531–542 (cit. on p. 55).

[67] C. James and K. Yuen-Yick. “A brief review of several numerical methods for one-dimensional Stefan problems”. In: *Thermal Science* 13.2 (2009), pp. 61–72 (cit. on p. 61).

[68] N. Javani, I. Dincer, G. F. Naterer, and G. L. Rohrauer. “Modeling of passive thermal management for electric vehicle battery packs with PCM between cells”. In: *Applied Thermal Engineering* 73.1 (Dec. 2014), pp. 307–316.

[69] E. Javierre, C. Vuik, F. J. Vermolen, and S. van der Zwaag. “A comparison of numerical models for one-dimensional Stefan problems”. In: *Journal of Computational and Applied Mathematics* 192.2 (Aug. 2006), pp. 445–459 (cit. on p. 61).

[70] J. Jiang and C. Zhang. *Fundamentals and Applications of Lithium-ion Batteries in Electric Drive Vehicles*. Jiang/Fundamentals and Applications of Lithium-ion Batteries in Electric Drive Vehicles. Singapore: John Wiley & Sons Singapore Pte. Ltd, May 2015 (cit. on p. 2).

[71] A. Jossen and W. Weydanz. *Moderne Akkumulatoren richtig einsetzen*. 36 Tabellen. 2006 (cit. on pp. 8, 17).

[72] *Journal of Power Sources - Online Database. Accessed: 01/02/2017*. URL: `www.sciencedirect.com/science/journals/03787753` (cit. on p. 1).

[73] M. Jurkowska and I. Szczygieł. “Review on properties of microencapsulated phase change materials slurries (mPCMS)”. In: *Applied Thermal Engineering* 98 (Apr. 2016), pp. 365–373 (cit. on p. 55).

[74] G. Karimi and A. R. Dehghan. “Thermal Management Analysis of a Lithium-Ion Battery Pack using Flow Network Approach”. In: *International Journal of Mechanical Engineering and Mechatronics* (2012) (cit. on pp. 20, 23).

[75] Y. Keho. “The Basics of Linear Principal Components Analysis”. In: *Principal Component Analysis*. InTech, Mar. 2012 (cit. on p. 113).

[76] S. A. Khateeb, S. Amiruddin, M. Farid, J. R. Selman, and S. Al-Hallaj. “Thermal management of Li-ion battery with phase change material for electric scooters: experimental validation”. In: *Journal of Power Sources* 142.1-2 (Mar. 2005), pp. 345–353.

[77] S. A. Khateeb, M. M. Farid, J. R. Selman, and S. Al-Hallaj. “Design and simulation of a lithium-ion battery with a phase change material thermal management system for an electric scooter”. In: *Journal of Power Sources* 128.2 (Apr. 2004), pp. 292–307 (cit. on p. 71).

[78] H. Kiehne. “Battery Technology Handbook”. In: (2003) (cit. on p. 8).

[79] G. H. Kim, J. Gonder, J. Lustbader, and A. Pesaran. “Thermal management of batteries in advanced vehicles using phase-change materials”. In: *The World Electric Vehicle . . .* 2.2 (2008), pp. 46–59.

[80] R. Kizilel, A. Lateef, R. Sabbah, M. M. Farid, J. R. Selman, and S. Al-Hallaj. “Passive control of temperature excursion and uniformity in high-energy Li-ion battery packs at high current and ambient temperature”. In: *Journal of Power Sources* 183.1 (Aug. 2008), pp. 370–375.

[81] R. Kizilel, R. Sabbah, J. R. Selman, and S. Al-Hallaj. “An alternative cooling system to enhance the safety of Li-ion battery packs”. In: *Journal of Power Sources* 194.2 (Dec. 2009), pp. 1105–1112 (cit. on p. 71).

[82] J. Kosny, N. Shukla, and A. Fallahi. *Cost Analysis of Simple Phase Change Material-Enhanced Building Envelopes in Southern U.S. Climates.* Tech. rep. EERE Publication and Product Library, Jan. 2013 (cit. on p. 52).

[83] Y. Kozak and G. Ziskind. “Numerical modeling of a finned PCM heat sink”. In: *NUMERICAL ANALYSIS AND APPLIED MATHEMATICS ICNAAM 2012: International Conference of Numerical Analysis and Applied Mathematics.* AIP, 2012, pp. 2375–2378 (cit. on p. 66).

[84] E. D. Kravvaritis, K. A. Antonopoulos, and C. Tzivanidis. “Experimental determination of the effective thermal capacity function and other thermal properties for various phase change materials using the thermal delay method”. In: *Applied Energy* 88.12 (Dec. 2011), pp. 4459–4469 (cit. on p. 49).

[85] I. L. Krüger, D. Limperich, and G. Schmitz. “Energy Consumption Of Battery Cooling In Hybrid Electric Vehicles”. In: (2012) (cit. on p. 41).

[86] G. A. Lane. “Low temperature heat storage with phase change materials”. In: *International Journal of Ambient Energy* 1.3 (Mar. 2011), pp. 155–168 (cit. on p. 49).

[87] R. J. Lauf and C. J. Hamby. *Metallic phase-change materials for solar dynamic energy storage systems.* Tech. rep. Oak Ridge National Laboratory (ORNL), Oak Ridge, TN, Dec. 1990 (cit. on p. 47).

[88] D. I. M. Lichtenberger, D. I. F. Kessler, D. I. H. Graf, and D. I. E. Bauchrowitz. “The hybrid drive system in the BMW active hybrid 7”. In: *ATZ worldwide* 112.9 (2010) (cit. on p. 41).

[89] C. Lin, S. Xu, G. Chang, and J. Liu. “Experiment and simulation of a LiFePO4 battery pack with a passive thermal management system using composite phase change material and graphite sheets”. In: *Journal of Power Sources* 275 (Feb. 2015), pp. 742–749.

[90] C. Lin, S. Xu, Z. Li, B. Li, G. Chang, and J. Liu. “Thermal analysis of large-capacity LiFePO4 power batteries for electric vehicles”. In: *Journal of Power Sources* 294 (Oct. 2015), pp. 633–642 (cit. on p. 11).

[91] M. Linder. “Using thermochemical reactions in thermal energy storage systems”. In: *Advances in Thermal Energy Storage Systems.* Elsevier, 2015, pp. 357–374 (cit. on p. 44).

[92] G. Liu, M. Ouyang, L. Lu, J. Li, and X. Han. “Analysis of the heat generation of lithium-ion battery during charging and discharging considering different influencing factors”. In: *Journal of Thermal Analysis and Calorimetry* 116.2 (Jan. 2014), pp. 1001–1010 (cit. on p. 29).

[93] A. Loges, S. Herberger, P. Seegert, and T. Wetzel. “A study on specific heat capacities of Li-ion cell components and their influence on thermal management”. In: *Journal of Power Sources* 336 (Dec. 2016), pp. 341–350 (cit. on p. 20).

[94] A. Lukhanin, A. Belyaev, D. Fedorchenko, M. Khazhmuradov, O. Lukhanin, Y. Rudychev, and U. S. Rohatgi. “Thermal Characteristics of Air Flow Cooling in the Lithium Ion Batteries Experimental Chamber”. In: *ASME 2012 Heat Transfer Summer Conference collocated with the ASME 2012 Fluids Engineering Division Summer Meeting and the ASME 2012 10th International Conference on Nanochannels, Microchannels, and M.* ASME, July 2012, pp. 129–133 (cit. on p. 34).

[95] E. Maiser et al. *Battery Production Equipment 2030.* Ed. by E. Maiser, S. Michaelis, and D. Müller. VDMA Battery Production, 2014 (cit. on p. 2).

[96] H. Maleki. “Thermal Properties of Lithium-Ion Battery and Components”. In: *Journal of The Electrochemical Society* 146.3 (1999), p. 947 (cit. on pp. 19, 22, 23).

[97] H. Maleki, H. Wang, W. Porter, and J. Hallmark. “Li-Ion polymer cells thermal property changes as a function of cycle-life”. In: *Journal of Power Sources* 263 (Oct. 2014), pp. 223–230 (cit. on p. 23).

[98] M. Malik, I. Dincer, and M. A. Rosen. “Review on use of phase change materials in battery thermal management for electric and hybrid electric vehicles”. In: *International Journal of Energy Research* 40.8 (Feb. 2016), pp. 1011–1031 (cit. on p. 69).

[99] B. K. Mandal, A. K. Padhi, Z. Shi, S. Chakraborty, and R. Filler. “Thermal runaway inhibitors for lithium battery electrolytes”. In: *Journal of Power Sources* 161.2 (Oct. 2006), pp. 1341–1345 (cit. on p. 16).

[100] M. J. Marongiu and R. L. Clarksean. “Thermal management of battery compartments of outdoor telecommunication cabinets using phase change materials (PCM)”. In: *Power and Energy Systems in Converging Markets*. IEEE, pp. 29–34.

[101] A. Mathur, R. Kasetty, J. Oxley, J. Mendez, and K. Nithyanandam. “Using Encapsulated Phase Change Salts for Concentrated Solar Power Plant”. In: *Energy Procedia* 49 (2014), pp. 908–915 (cit. on p. 47).

[102] D. McCord, J. Crepeau, A. Siahpush, and J. A. Ferres Brogin. “Analytical solutions to the Stefan problem with internal heat generation”. In: *Applied Thermal Engineering* 103 (June 2016), pp. 443–451 (cit. on pp. 62, 63).

[103] H. Mehling and L. F. Cabeza. *Heat and cold storage with PCM*. An up to date introduction into basics and applications. Springer Science & Business Media, Aug. 2008 (cit. on pp. 47, 48, 53).

[104] A. Mills and S. Al-Hallaj. “Simulation of passive thermal management system for lithium-ion battery packs”. In: *Journal of Power Sources* 141.2 (Mar. 2005), pp. 307–315.

[105] S. L. Mitchell and M. Vynnycky. “On the numerical solution of two-phase Stefan problems with heat-flux boundary conditions”. In: *Journal of Computational and Applied Mathematics* 264 (July 2014), pp. 49–64 (cit. on p. 63).

[106] J. Nanda, S. K. Martha, W. D. Porter, H. Wang, N. J. Dudney, M. D. Radin, and D. J. Siegel. “Thermophysical properties of LiFePO4 cathodes with carbonized pitch coatings and organic binders: Experiments and first-principles modeling”. In: *Journal of Power Sources* 251 (2014), p. 8 (cit. on pp. 20, 23).

[107] J. S. Neubauer and E. Wood. “Will Your Battery Survive a World With Fast Chargers?” In: *SAE 2016 World Congress and Exhibition*. 400 Commonwealth Drive, Warrendale, PA, United States: SAE International, Apr. 2015, pp. 2015–01–1196 (cit. on p. 82).

[108] J. Neubauer and A. Pesaran. “A techno-economic analysis of BEVs with fast charging infrastructure”. In: *2013 World Electric Vehicle Symposium and Exhibition (EVS27)* (2013), pp. 1–12 (cit. on pp. 2, 82).

[109] H. Noureddini, B. C. Teoh, and L. Davis Clements. “Densities of vegetable oils and fatty acids”. In: *Journal of the American Oil Chemists Society* 69.12 (Dec. 1992), pp. 1184–1188 (cit. on p. 50).

[110] M. Okubo, Y. Tanaka, H. Zhou, T. Kudo, and I. Honma. “Determination of Activation Energy for Li Ion Diffusion in Electrodes”. In: *The Journal of Physical Chemistry B* 113.9 (2009), p. 2840 (cit. on p. 8).

[111] N. Omar, Y. Firouz, H. Gualous, J. Salminen, T. Kallio, J. M. Timmermans, T. Coosemans, P. Van den Bossche, and J. Van Mierlo. “Aging and degradation of lithium-ion batteries”. In: *Rechargeable Lithium Batteries.* Elsevier, 2015, pp. 263–279 (cit. on p. 17).

[112] M. Park, X. Zhang, M. Chung, G. B. Less, and A. M. Sastry. “A review of conduction phenomena in Li-ion batteries”. In: *Journal of Power Sources* 195.24 (2010), p. 7904 (cit. on p. 8).

[113] G. Pellegrini and R. Colombo. “Building Components with Integrated Latent Heat Storage”. In: *First E.C. Conference on Solar Heating.* Dordrecht: Springer Netherlands, 1984, pp. 267–272 (cit. on p. 47).

[114] A. A. Pesaran. “Battery thermal models for hybrid vehicle simulations”. In: *Journal of Power Sources* 110.2 (Aug. 2002), pp. 377–382 (cit. on p. 10).

[115] C. Pillot. “The Rechargeable Battery Market and Main Trends 2011-2020”. In: *Batteries 2016.* Nice, Sept. 2016 (cit. on p. 2).

[116] M. Y. Ramandi, I. Dincer, and G. F. Naterer. “Heat transfer and thermal management of electric vehicle batteries with phase change materials”. In: *Heat and Mass Transfer* 47.7 (Feb. 2011), pp. 777–788.

[117] A. V. Ramayya and K. N. Ramesh. “Exergy analysis of latent heat storage systems with sensible heating and subcooling of PCM”. In: *International Journal of Energy Research* 22.5 (Apr. 1998), pp. 411–426 (cit. on p. 51).

[118] E. P. Roth, C. C. Crafts, and D. H. Doughty. “Thermal abuse studies on lithium ion rechargeable batteries”. In: *Sixteenth Annual Battery Conference on Applications and Advances.* IEEE, 2001, pp. 375–380 (cit. on p. 16).

[119] S. N. Al-Saadi and Z. J. Zhai. “Systematic evaluation of mathematical methods and numerical schemes for modeling PCM-enhanced building enclosure”. In: *Energy and Buildings* 92 (Apr. 2015), pp. 374–388 (cit. on p. 64).

[120] *SAE Electric Vehicle and Plug in Hybrid Vehicle Conductive Charge Coupler, SAE J1772.* 2016 (cit. on p. 2).

[121] N. Sato. “Thermal behavior analysis of lithium-ion batteries for electric and hybrid vehicles”. In: *Journal of Power Sources* 99.1-2 (Aug. 2001), pp. 70–77 (cit. on p. 7).

[122] C. Sattler and A. Wörner. “Thermochemical Energy Storage”. In: (2013) (cit. on p. 44).

[123] L. H. Saw, A. A. O. Tay, and L. W. Zhang. “Thermal management of lithium-ion battery pack with liquid cooling”. In: *2015 31st Thermal Measurement, Modeling & Management Symposium (SEMI-THERM).* IEEE, 2015, pp. 298–302 (cit. on p. 33).

[124] J. Schröder. “Thermal Energy Storage and Control”. In: *Journal of Engineering for Industry* 97.3 (Aug. 1975), pp. 893–896 (cit. on p. 48).

[125] S. F. Schuster, T. Bach, E. Fleder, J. Müller, M. Brand, G. Sextl, and A. Jossen. “Nonlinear aging characteristics of lithium-ion cells under different operational conditions”. In: *Journal of Energy Storage* 1 (June 2015), pp. 44–53 (cit. on p. 15).

[126] H.-G. Schweiger, O. Obeidi, O. Komesker, A. Raschke, M. Schiemann, C. Zehner, M. Gehnen, M. Keller, and P. Birke. “Comparison of Several Methods for Determining the Internal Resistance of Lithium Ion Cells”. In: *Sensors* 10.6 (2010), p. 5604 (cit. on p. 13).

[127] A. Senyshyn, M. J. Mühlbauer, O. Dolotko, and H. Ehrenberg. “Low-temperature performance of Li-ion batteries: The behavior of lithiated graphite”. In: *Journal of Power Sources* 282 (May 2015), pp. 235–240 (cit. on p. 7).

[128] J. Singh. “Future energy technology - Thermal hazards of Li-ion batteries”. In: *Institution of Chemical Engineers Symposium Series.* HEL Ltd, Borehamwood, United Kingdom. Dec. 2012, pp. 489–495 (cit. on p. 31).

[129] M. C. Smart and B. V. Ratnakumar. “Effects of Electrolyte Composition on Lithium Plating in Lithium-Ion Cells”. In: *Journal of The Electrochemical Society* 158.4 (2011), A379–A389 (cit. on p. 15).

[130] A. Solé, L. Miró, C. Barreneche, I. Martorell, and L. F. Cabeza. “Review of the T-history method to determine thermophysical properties of phase change materials (PCM)”. In: *Renewable and Sustainable Energy Reviews* 26 (Oct. 2013), pp. 425–436 (cit. on p. 52).

[131] R. Spotnitz and J. Franklin. “Abuse behavior of high-power, lithium-ion cells”. In: *Journal of Power Sources* 113.1 (Jan. 2003), pp. 81–100 (cit. on p. 7).

[132] B. Stiaszny, J. C. Ziegler, E. E. Krauß, M. Zhang, J. P. Schmidt, and E. Ivers-Tiffée. “Electrochemical characterization and post-mortem analysis of aged LiMn2O4-NMC/graphite lithium ion batteries part II: Calendar aging”. In: () (cit. on pp. 11–13).

[133] H. Sun, B. Tossan, and D. Brouns. “Thermal Behavior Study on HEV Air-Cooled Battery Pack”. In: *SAE 2016 World Congress and Exhibition.* 400 Commonwealth Drive, Warrendale, PA, United States: SAE International, Apr. 2011, pp. 2011–01–1368 (cit. on p. 35).

[134] H. Taheri and A. Sharma. “An Overview of Phase Change Materials for Building Applications”. In: *Rechargeable Batteries.* New Delhi: Springer India, Apr. 2015, pp. 189–213 (cit. on p. 47).

[135] *The Rechargeable Battery Market and Main Trends 2014-2025.* Aivcenne Energy. Fort Lauderdale, Mar. 2015 (cit. on pp. 2, 4).

[136] E. V. Thomas, H. L. Case, D. H. Doughty, R. G. Jungst, G. Nagasubramanian, and E. P. Roth. “Accelerated power degradation of Li-ion cells”. In: *Journal of Power Sources* 124.1 (2003), p. 254 (cit. on p. 13).

[137] K. E. Thomas and J. Newman. “Thermal Modeling of Porous Insertion Electrodes”. In: *Journal of The Electrochemical Society* 150.2 (2003), A176 (cit. on p. 27).

[138] P. Tittelein et al. “Simulation of the thermal and energy behaviour of a composite material containing encapsulated-PCM: Influence of the thermodynamical modelling”. In: *Applied Energy* 140 (Feb. 2015), pp. 269–274 (cit. on p. 65).

[139] Y. Tomizawa, K. Sasaki, A. Kuroda, R. Takeda, and Y. Kaito. “Experimental and numerical study on phase change material (PCM) for thermal management of mobile devices”. In: *Applied Thermal Engineering* 98 (Apr. 2016), pp. 320–329 (cit. on p. 69).

[140] C. Uher. “Thermal Conductivity of Metals”. In: *Thermal Conductivity.* Springer US, 2004, pp. 21–91 (cit. on p. 23).

[141] N. Ukrainczyk, S. Kurajica, and J. Šipušić. “Thermophysical Comparison of Five Commercial Paraffin Waxes as Latent Heat Storage Materials”. In: *Chemical and Biochemical Engineering Quarterly* 24.2 (July 2010), pp. 129–137 (cit. on p. 50).

[142] A. Väyrynen and J. Salminen. “Lithium ion battery production”. In: *The Journal of Chemical Thermodynamics* 46 (Mar. 2012), pp. 80–85 (cit. on p. 17).

[143] V. R. Voller, J. B. Swenson, and C. Paola. “An analytical solution for a Stefan problem with variable latent heat”. In: *International Journal of Heat and Mass Transfer* 47.24 (Nov. 2004), pp. 5387–5390 (cit. on p. 62).

[144] T. Waldmann, M. Wilka, M. Kasper, M. Fleischhammer, and M. Wohlfahrt-Mehrens. “Temperature dependent ageing mechanisms in Lithium-ion batteries – A Post-Mortem study”. In: *Journal of Power Sources* 262 (2014), p. 129 (cit. on p. 11).

[145] W. Q. Walker. “Rechargeable lithium batteries for aerospace applications”. In: *Rechargeable Lithium Batteries*. Elsevier, 2015, pp. 369–383 (cit. on p. 14).

[146] Q. Wang, P. Ping, X. Zhao, G. Chu, J. Sun, and C. Chen. “Thermal runaway caused fire and explosion of lithium ion battery”. In: *Journal of Power Sources* 208 (June 2012), pp. 210–224 (cit. on pp. 1, 16).

[147] X. Wang and M. Dennis. “Characterisation of thermal properties and charging performance of semi-clathrate hydrates for cold storage applications”. In: *Applied Energy* 167 (Apr. 2016), pp. 59–69 (cit. on p. 49).

[148] Y.-W. Wang and C.-M. Shu. “Hazard Characterizations of Li-Ion Batteries: Thermal Runaway Evaluation by Calorimetry Methodology”. In: *Rechargeable Batteries*. Cham: Springer International Publishing, June 2015, pp. 419–454 (cit. on p. 31).

[149] Z. Wang, Z. Zhang, L. Jia, and L. Yang. “Paraffin and paraffin/aluminum foam composite phase change material heat storage experimental study based on thermal management of Li-ion battery”. In: *Applied Thermal Engineering* 78 (Mar. 2015), pp. 428–436.

[150] G. Wettermark. “Thermochemical Energy Storage”. In: *Energy Storage Systems*. Dordrecht: Springer Netherlands, 1989, pp. 673–681 (cit. on p. 44).

[151] M. A. White. “Heat storage systems”. In: *AccessScience, McGraw-Hill Education* (2014) (cit. on p. 48).

[152] M. Widden. “Laminar and turbulent flow; flow in pipes”. In: *Fluid Mechanics*. London: Macmillan Education UK, 1996, pp. 351–398 (cit. on p. 35).

[153] A. Wiebelt, T. Isermeyer, T. Siebrecht, and T. Heckenberger. “Thermomanagement of Li-ion batteries”. In: *ATZ worldwide* 111.7-8 (2009), pp. 12–15 (cit. on p. 38).

[154] S. Wilke, B. Schweitzer, S. Khateeb, and S. Al-Hallaj. “Preventing thermal runaway propagation in lithium ion battery packs using a phase change composite material: An experimental study”. In: *Journal of Power Sources* 340 (Feb. 2017), pp. 51–59.

[155] N. Williard, W. He, C. Hendricks, and M. Pecht. “Lessons learned from the 787 Dreamliner issue on lithium-ion battery reliability”. In: *Energies* 6.9 (2013), pp. 4682–4695 (cit. on p. 1).

[156] S. Wold, K. Esbensen, and P. Geladi. “Principal component analysis”. In: *Chemometrics and Intelligent Laboratory Systems* 2.1-3 (1987), pp. 37–52 (cit. on p. 114).

[157] B. Wu, R. G. Reddy, and R. D. Rogers. “Novel Ionic Liquid Thermal Storage For Solar Thermal Electric Power Systems”. In: *Solar Forum 2001, Washington DC* (cit. on p. 48).

[158] H. Wulfmeier, A. Omelcenko, D. Albrecht, D. Klimm, W. El Mofid, M. Strafela, S. Ulrich, A. Bund, and H. Fritze. “Thermal Stability of Materials for Thin-Film Electrochemical Cells Investigated by Thin-Film Calorimetry”. In: *MRS Advances* 1.15 (Jan. 2016), pp. 1043–1049 (cit. on pp. 20, 23).

[159] B. Xie, W.-l. Cheng, and Z.-m. Xu. “Studies on the effect of shape-stabilized PCM filled aluminum honeycomb composite material on thermal control”. In: *International Journal of Heat and Mass Transfer* 91 (Dec. 2015), pp. 135–143 (cit. on p. 55).

[160] R. Yazami and Y. F. Reynier. “Mechanism of self-discharge in graphite–lithium anode”. In: *Electrochimica Acta* (2002) (cit. on p. 14).

[161] K. Young, C. Wang, L. Y. Wang, and K. Strunz. “Electric Vehicle Battery Technologies”. In: *Electric Vehicle Integration into Modern Power Networks*. New York, NY: Springer New York, Oct. 2012, pp. 15–56 (cit. on p. 17).

[162] A. Zeh, M. Rau, and R. Witzmann. “Comparison of decentralised and centralised grid-compatible battery storage systems in distribution grids with high PV penetration”. In: *Progress in Photovoltaics: Research and Applications* 24.4 (Dec. 2014), pp. 496–506 (cit. on p. 95).

[163] A. Zeh and R. Witzmann. “Operational Strategies for Battery Storage Systems in Low-voltage Distribution Grids to Limit the Feed-in Power of Roof-mounted Solar Power Systems”. In: *Energy Procedia* 46 (2014), pp. 114–123 (cit. on p. 94).

[164] S. S. Zhang, K. Xu, and T. R. Jow. “The low temperature performance of Li-ion batteries”. In: *Journal of Power Sources* 115.1 (2003), p. 137 (cit. on p. 14).

[165] S. S. Zhang. “The effect of the charging protocol on the cycle life of a Li-ion battery”. In: *Journal of Power Sources* 161.2 (Oct. 2006), pp. 1385–1391 (cit. on p. 15).

List of Figures

1.1 Development of publication numbers based on thermal keywords [72] 1
1.2 Global LIB market trends by year on cell level [135] 2
1.3 Impact of ambient temperature on BTMS energy demand and driving range 3
1.4 Cost composition of automotive Li-ion battery packs [135] 4
1.5 Volume and weight distribution of battery pack components as used in EVA electric vehicle (see section 8.1) 4
1.6 Systematic approach for case study evaluation 5

2.1 Internal 1 kHz AC impedance vs. temperature 9
2.2 Extent of temperature spread within one cell dependent on C rate 9
2.3 Extent of temperature spread within a battery pack after 1 C charge 10
2.4 Usable capacity of a 60 Ah NMC pouch cell as function of C rate and ambient temperature 11
2.5 Cyclic irreversible capacity fade at 1C/1C as a function of ambient temperature 12
2.6 Irreversible capacity loss of a 60 Ah NMC pouch cell during soaking at 50 % SOC . . . 12
2.7 Increase of internal resistance (VDA current step) of a 60 Ah NMC pouch cell over charge throughput 13
2.8 Increase of internal resistance (VDA current step) of a 60 Ah NMC pouch cell during soaking at 50 % SOC 13
2.9 Self-discharge of a 60 Ah NMC pouch cell at different storage temperatures 14
2.10 Low temperature performance of a 60 Ah NMC pouch cell at 0.5 C charge/discharge . . 15
2.11 Impact of lithium plating during low temperature fast charge 15
2.12 Triggered Thermal Runaway (heat-wait-search method) 16

3.1 Process of dissasembly and weighing of cell components 20
3.2 Result data of a calorimetric heat capacity determination 21
3.3 Process of steady state $\lambda_\perp$ determination applied to a 60 Ah NMC pouch cell 25
3.4 Measurement data of steady state methodology 25
3.5 Experimental setup for a one-sided TPS measurement on a cylindrical LFP cell 26
3.6 Result data of TPS thermal conductivity determination 26
3.7 Temperature of a 60 Ah NMC cell cycled at different C rates under adiabatic conditions 28
3.8 Heat rate of a 60 Ah NMC cell cycled at different C rates under adiabatic conditions . . 28
3.9 Heat-wait-search study for different cell types 31

4.1 Main components of a Toyota Prius battery pack cooling system 34
4.2 Layout of air cooled system - top view 35
4.3 Dual circuit liquid cooling concept 38
4.4 Cross section of liquid based cooling, heat flow path and schematic thermal model . . . 39
4.5 Refrigerant based cooling concept 41
4.6 Cross section of refrigerant based cooling, heat flow path and schematic thermal model . 42

5.1 Overview on PCM types, temperature ranges and storage capacities [103] 48
5.2 Melting temperatures of selected PCMs in the range of 0 °C to 100 °C [17], [86] 49
5.3 Gravimetric latent heat of fusion of selected PCMs [147], [84] 49
5.4 Volumetric latent heat of selected PCMs [141], [1], [61], [109] 50
5.5 Thermal conductivity of selected PCMs in solid/liquid state 50
5.6 Melting/solidification of a paraffin based PCM with $T_{melt} = 28°C$ tracked by DSC . . . 51
5.7 Cost of selected PCMs [82] 52
5.8 Comparison of DSC and T-history measurements 53
5.9 Positive impact of internal macro heat spreaders 54
5.10 Schematic structure and SEM images of microencapsulated PCM 55
5.11 Steps of expanded graphite production 56
5.12 Thermal conductivity as a function of graphite matrix density 56
5.13 Thermal contact resistance as a function of graphite matrix density 57
5.14 Transient penetration depth of selected PCM samples 59

6.1 Fundamental layout of a one-dimensional Stefan Problem 61
6.2 Modeling phase change by temperature dependent c_p 64
6.3 Modeling phase change by direct enthalpy method 65
6.4 Average temperature of front surface - experiment vs. simulation models 67
6.5 Comparison of selected numerical PCM models 68

7.1 Overview on research landscape of PCM use in LIB applications 69
7.2 Experimental setup for single cell experiments 70
7.3 Transient temperature profiles 72
7.4 Transient temperature profiles 74
7.5 Transient temperature profiles 76
7.6 Transient temperature profiles 78

8.1 Methodology for PCM selection 81
8.2 Electric taxi concept EVA 82
8.3 EVA cooling concept 84
8.4 Battery pack of the electric vehicle EVA 85
8.5 Battery module of the electric vehicle EVA 86
8.6 Meshed model for battery pack simulation 87
8.7 PCM utilization factor as a function of material properties 88
8.8 Selected PCM configurations for fast charging case study 89
8.9 Individual cell temperatures - Reference stack vs. PCM stack 91
8.10 Photos of anode surfaces, comparing reference cell and abruptly aged cell 93
8.11 Sudden aging for PCM cooled cell stacks 93
8.12 Stationary Energy Storage System - Energy Neighbor 94
8.13 Power generation and load curve of a small village close to Munich 95
8.14 Load curves for stationary storage application 95
8.15 Heat generation per container resulting from the load profile shown in figure 8.14 96
8.16 Ambient temperature range over one year [29] 96
8.17 Daily temperature spread over one year [29] 97
8.18 System design of Energy Neighbor cooling concept 98

8.19 Design and core components of the stationary storage unit battery rack 99
8.20 Design and core components of the stationary storage unit battery module 100
8.21 Internal and external heat load during one day of operation 101
8.22 Comparison of simulated PCM variants and experimentally measured reference in terms of average battery temperature 102
8.23 Two alternative battery box designs 103
8.24 Experiment vs. simulation - PCM equipped cell blocks 104
8.25 Design and main components of the investigated stationary storage module 105
8.26 Thermal runaway propagation after short circuit of cell 6 at $t = 0s$ 107
8.27 Thermal runaway propagation after short circuit of cell 6 109
8.28 Impact of the different PCMs on max. battery temperature after TR of one cell 110
8.29 Temperature distribution at $T = T_{max}$ dependent on PCM used 111

9.1 Scatter plots of all material samples measured 113
9.2 Parameter sensitivity/response surface - use case: Peak mitigation 115
9.3 Parameter sensitivity/response surface - use case: Passive cooling 116
9.4 Parameter sensitivity/repsonse surface - use case: TR propagation prevention 117

List of Tables

2.1 Overview on thermal dependencies . . . 17
2.2 Operating conditions of common cell types as found in literature [142], [161], [71], [9] . . 17

3.1 Specific heat capacity of selected materials common in LIBs . . . 20
3.2 Specific heat capacity calculated from individual cell components . . . 21
3.3 Specific heat capacity calculated from individual cell components . . . 22
3.4 Analogy between thermal and electrical network . . . 23
3.5 Thermal conductivity of selected materials common in LIBs . . . 23
3.6 Properties of individual cell layers . . . 24
3.7 Thermal conductivity estimations . . . 24
3.8 Result data - steady state measurements on 60 Ah NMC cell . . . 25
3.9 Thermal conductivity values obtained via TPS method . . . 27
3.10 Typical cycle data for exemplary automotive and stationary load profiles . . . 30
3.11 Exemplaric onset temperature values for selected cells . . . 31
3.12 Overview on properties of selected cell types . . . 32

4.1 Sample data for 60 Ah NMC pouch cell used for exemplary comparative calculations . . 33
4.2 Assumptions made for air based cooling system . . . 37
4.3 Assumptions made for liquid based cooling system . . . 40
4.4 Assumptions made for refrigerant based cooling system . . . 42
4.5 Benchmark of common Battery Thermal Management Concepts . . . 43

5.1 Selected types of expanded graphite matrices . . . 57
5.2 Selected types of graphite based PCM composites . . . 58

6.1 Temperature and path dependent source terms Q_{PCM} . . . 66
6.2 Material properties for PCM sample . . . 67

7.1 Properties of selected PCM samples for passive temperature control . . . 72
7.2 Impact of different PCM samples used for temperature control . . . 72
7.3 Properties of selected PCM samples for peak load mitigation . . . 74
7.4 Impact of different PCM samples used for peak mitigation . . . 74
7.5 Properties of selected PCM samples for increasing temperature uniformity . . . 76
7.6 Impact of different PCM samples used for increasing temperature uniformity . . . 76
7.7 Properties of selected PCM samples for prevention of thermal runaway propagation . . . 78
7.8 Impact of different PCM samples used for TR propagation prevention . . . 78
7.9 Basic requirement scheme for different applications . . . 79

8.1 Specifications of electric taxi concept EVA . . . 82
8.2 Singapore driving cycle - single cell load profile . . . 83
8.3 Specifications of EVA cooling loops . . . 84

8.4 Technical data of the EVA battery pack . . . 85
8.5 PCM candidates for integration in EVA battery pack . . . 88
8.6 Impact of PCM scenario on cooling system and driving range . . . 90
8.7 Impact of PCM integration on battery stack temperature distribution . . . 91
8.8 Specifications of Energy Neighbor . . . 94
8.9 Monthly temperature profile and temperature distribution for Moosham, Germany [29] . 97
8.10 Specifications of Energy Neighbor cooling concept . . . 98
8.11 Technical specifications of the stationary storage unit battery rack . . . 99
8.12 Specifications of the stationary storage unit battery module . . . 100
8.13 PCM candidates for integration in the "Energy Neighbor" stationary battery . . . 101
8.14 Specifications of reference and PCM cell block design . . . 103
8.15 Specification of cell module . . . 105
8.16 Data recorded during TR abuse experiments . . . 106
8.17 Thermal material properties . . . 107
8.18 PCM candidates for TR prevention application . . . 110
8.19 Result data of PCM impact used in TR prevention application . . . 111

9.1 Data recorded during TR abuse experiments . . . 114